The Numerical Analysis of a Turbulent Compressible Jet

James R. DeBonis
Glenn Research Center, Cleveland, Ohio

National Aeronautics and
Space Administration

Glenn Research Center

May 2001

Acknowledgments

This dissertation would not have been possible without the efforts and support of my teachers, colleagues, and friends. I would like to thank my advisor Dr. Jim Scott for both his guidance and encouragement during my studies and also for making this process an enjoyable one. I would also like to thank Dr. Richard Bodonyi, Dr. Michael Foster, and Dr. Mohammad Samimy for reviewing this document. They have made my studies at Ohio State very rewarding. This work was done under the doctoral study program at the NASA Glenn Research Center. I am very grateful for the support of my supervisors, Mr. Bernard Blaha and Dr. Rickey Shyne, and project managers, Ms. Mary Jo Long-Davis and Mr. Waldo Acosta. During my research, I have sought the help and advice of many colleagues. In particular I would like to thank Mr. Ibraheem Al-Qadi at Ohio State, Mr. Dennis Yoder at NASA Glenn, Dr. Ray Hixon at the Ohio Aerospace Institute, and Dr. Tom Barber at UTRC. I am grateful to Dr. Jay Panda for his high quality experimental data and for the many informative discussions on jet flows. A special note of thanks also goes to my NASA office-mate and fellow Ph.D. candidate Nick Georgiadis. Nick and I have spent many, many hours "discussing" the finer points of Large-Eddy Simulation. My research is the better for it.

TABLE OF CONTENTS

LIST OF TABLES

LIST OF FIGURES

LIST OF SYMBOLS

a	speed of sound
c	wave speed
c_v	specific heat at constant volume
e	internal energy
e_t	total energy
k	thermal conductivity
k	turbulent kinetic energy
ℓ	turbulent length scale
n_i	surface normal vector
p	pressure
q_i	heat flux vector
t	time
u_i	velocity vector
x_i	coordinate vector
y^+	inner variable distance
u,v,w	velocity components
x,y,z	cartesian coordinates
x,r,θ	cylindrical coordinates

A^+	Van Driest damping function constant
C	Smagorinsky model coefficient
C_I	Smagorinsky model coefficient
C_1	Sutherland's viscosity law coefficient
C_2	Sutherland's viscosity law coefficient
C_3	sub-grid scale turbulent dissipation rate model coefficient
C_f	skin friction coefficient
C_p	pressure coefficient
D_i	sub-grid scale turbulent diffusion vector
D_j	jet diameter
$\mathbf{D}$	spatial finite difference operator
$\hat{D}$	eigenvalues of spatial finite difference operator
E, F, G	flux vectors
H	axisymmetric source term vector
J	Jacobian
Pr	Prandtl number
Pr_t	turbulent Prandtl number
Q	conservation variable vector
Q_i	sub-grid scale heat flux vector
R	specific gas constant
$\mathcal{R}$	correlation coefficient
Re_j	Reynolds number base on jet diameter
Re_t	Reynolds number based on turbulent length scale
Re_x	Reynolds number based on axial distance

S_{ij}	strain rate tensor
T	temperature
U	velocity
U_c	convective velocity
U_n	velocity normal to the surface
U_θ	velocity at angle θ to the jet axis
α_m	Runge-Kutta coefficient
α_D	solution filter coefficient
β_m	Runge-Kutta coefficient
γ	ratio of specific heats
δ_{ij}	Kronecker delta
ϵ	turbulent dissipation rate
η	similarity variable
κ	Kolmogorov length scale
μ	dynamic viscosity
ν	kinematic viscosity
ρ	density
σ_{ij}	stress tensor
τ	time delay
τ_{ij}	sub-grid scale stress tensor
ϕ_i	two point correlation location vector
ψ_i	two point correlation separation vector
ω	wave number
ξ, η, ζ	computational coordinates

Δ	filter width
Δt	time step
Δx	spatial step

subscripts

avg	mass averaged
ex	exact
j	jet
max	maximum
min	minimum
rms	root mean square
sgs	sub-grid scale
v	viscous
0	stagnation/total condition
∞	freestream

superscripts

$^{-}$	spatially filtered quantity
$^{\sim}$	Favre averaged quantity
$^{\wedge}$	resolved quantity
$^{=}$	time averaged quantity
$'$	unresolved quantity
$''$	perturbation from time averaged value
$\hat{}$	turbulent intensity

CHAPTER 1

INTRODUCTION

The analysis of turbulent compressible jets is a critical technology for improving the performance of advanced aerospace propulsion systems. In both the military and commercial sectors a need exists for a better understanding and prediction of jet engine exhaust plumes and fuel injector flows. This dissertation addresses this need through the development and application of a computational method to analyze these flows, providing a better understanding of the underlying physics.

1.1 Motivation

The survivability of military aircraft depends on their ability to evade the enemy's defenses. Anti-aircraft systems employ infrared detectors and heat seeking missiles, which rely on the high temperature exhaust from the aircraft's engines. The military has a great interest in low-observable technology to reduce the size and intensity of this exhaust plume in order to increase the aircraft's survival rate.

In the commercial aircraft industry, reducing the noise generated by the aircraft has become an important focus, as increasingly stringent restrictions on noise levels are imposed near airports. The primary contribution to community noise is jet noise from the engine at takeoff. The mechanisms by which the jet generates sound are

not well understood. Expanding the knowledge of jet aeroacoustics has become the focus of several recent national programs including NASA's High Speed Research and Advanced Subsonic Technology programs.

Both the military and commercial sectors are interested in high speed ramjet and scramjet propulsion systems. These systems are being considered for fast response weapon systems, high speed aircraft and efficient airbreathing launch vehicles. The complete and rapid mixing of the fuel jet with the high speed airstream is key to their operation. A better predictor of the performance of fuel injectors and their interaction with the freestream flowfield is necessary.

1.2 Physics of Jets

The physics of jet flows is dominated by turbulent motion. Turbulent flows by definition are unsteady and randomly varying. Turbulence is three-dimensional and rotational with many vortical structures. The scales of the structures vary from the Kolmogorov microscales [1] to scales nearly on the order of the jet diameter. The large scales contain most of the turbulent energy and transport the majority of the momentum and energy. The energy is cascaded from the largest scales to the smallest. The smallest scales then dissipate the energy and are isotropic. The Kolmogorov scales, κ, are extremely small. Their ratio to the scales of the largest eddies is

$$\frac{\kappa}{\ell} = Re_t^{-3/4} \tag{1.1}$$

where ℓ is the size of the largest scales and Re_t is the turbulent Reynolds number. However, Wilcox shows for a typical turbulent flow the Kolmogorov scales are approximately seventy two times the mean free path of the molecules [2]. Thus, the continuum assumption can be used when modeling the flow at this level.

The turbulent motion in the jet flowfield is confined to the mixing layer, which is the interface between the flow from the nozzle and the ambient air (figure 1.1). The mixing layer begins at the jet lip and spreads radially with increasing distance downstream. The nozzle flow that has not been affected by the mixing layer maintains an inviscid character and is termed the potential core.

1.3 Computational Methods

An accurate and inexpensive method to predict the complex physics of jet flows would be a great benefit to low-observable, aeroacoustic, and fuel injector technology. Experimental studies of jets are an expensive and difficult undertaking and provide a limited amount of data. Analytical methods in this area are very limited in their applicability due to the steady-state and low Reynolds number assumptions that usually accompany them.

Computational fluid dynamics (CFD) offers an excellent alternative for jet analyses. In CFD, solutions to the governing equations of fluid motion are obtained using numerical methods. In principle, it does not require major simplifications to the equations that limit the applicability and accuracy of the simpler analytical methods. CFD provides a complete description of the flowfield at specified discretized points. In this way it is superior to experimental methods that provide a limited amount of data. In general, a CFD analysis is also less expensive than an experimental program.

Two sources of error limit the accuracy of CFD. The first error is the error introduced into the solution by the discretization of the equations. This discretization, or truncation, error is a function of both the numerical scheme used to solve the equations and the computational grid that specifies the discrete locations at which

the equations are solved. The second source of error is modeling error. This error is the result of assumptions made to model the particular geometry or physics of the problem. Modeling errors are introduced in grid generation, boundary condition specification and within problem formulation and solution process. In fact some of the largest and most widespread sources of modeling error occur in formulating and solving a turbulent flowfield. Three common methods are used to simulate turbulent flows. They are outlined below.

1.3.1   Reynolds Averaged Navier-Stokes Simulations

The most common approach to simulate a turbulent flow is to solve the Reynolds Averaged Navier-Stokes (RANS) equations. The RANS equations are obtained by time averaging the Navier-Stokes equations. The contribution of the unsteady terms in the equations is averaged out and the effect on the flow is replaced by the Reynolds stress tensor. In practice, this tensor is modeled using the Boussinesq approximation: it is replaced by the product of an eddy viscosity and the strain rate tensor. To further simplify, isotropic turbulence is typically assumed. The process of calculating the eddy viscosity is commonly referred to as turbulence modeling.

Turbulence modeling has been an active area of research for many years and a great number approaches exists. But due to the approximations inherent in the method, these approaches have failed to produce an adequate simulation of a turbulent jet.

The most widely used turbulence model for RANS simulations of jet flows is the k–ϵ model [3]. In this approach, two additional partial differential equations, transport equations for the turbulent kinetic energy, k, and the turbulent dissipation rate, ϵ, are solved and the eddy viscosity is computed from these quantities.

Corrections to the k–ε model to improve jet flow predictions have been developed. Sarkar [4] and Zeman [5] both introduced corrections to account for compressibility effects which retard the shear layer mixing in high speed jets. Pope [6] developed a vortex stretching correction that improved the prediction of round jets.

In a cooperative effort among the aerospace community. Barber et. al. [7] computed several jet flows using RANS techniques. They found that the solutions were highly dependent on the formulation of the turbulence model and the corrections used. They concluded that no one model provided adequate predictions over a range of jet conditions.

RANS simulations are the least CPU intensive method for computing a turbulent flow. Typically, the discretized equations are marched in time to convergence at a steady state. Time accuracy in intermediate steps is not necessary and is often sacrificed for computational speed. In general, the results obtained represent only the time average of the flowfield. Some unsteady information may be available from the turbulence model itself (i.e. turbulent kinetic energy is computed in the k–ε model).

1.3.2 Direct Numerical Simulations

In theory the simplest and most straightforward way to compute a turbulent flowfield is by performing a Direct Numerical Simulation (DNS). DNS methods solve the Navier-Stokes equations in a time accurate manner without approximation. In order to obtain an accurate representation of the turbulence, the turbulent motion down to the Kolmogorov scales must be accurately resolved in both time and space. In other words, the grid spacing must be no larger than the Kolmogorov scale. κ. The

Kolmogorov scales vary with the turbulent Reynolds number as shown in equation (1.1). In order to resolve just one large scale eddy we would need $\frac{l}{\kappa}$ grid points in each direction. a total of $Re_t^{9/4}$ points. And since the time step is linearly related to the grid size through the Courant Friedrichs Lewey (CFL) number [8]. the cost of the simulation is on the order of Re_t^3. The amount of computer memory available limits the size of the computational grid that can be used and the computer's processing speed gives a practical limit to the number of time steps possible in a simulation. Therefore. based on available computational resources. DNS is limited to very low Reynolds number flows.

One way to help alleviate this Reynolds number limitation on DNS is the use of high order numerical methods [9–15]. These methods have the ability to accurately capture small scale structures with fewer grid points than possible with traditional second-order accurate codes. This increased accuracy does come at the price of increased computational expense and the trade-off between the two has not been sufficiently investigated.

Freund [16–18] has computed Mach 0.8. 0.9, and 1.92 jets using a DNS technique. These jets had Reynolds numbers of 800, 3600, and 2000 respectively. This work has produced excellent agreement with experimental data and provided great insight into the flow behavior. But the Reynolds numbers of the jets are orders of magnitude smaller than any nozzle of practical interest.

1.3.3 Large-Eddy Simulations

A compromise between the approximations necessary in RANS and the computational limitations of DNS is Large-Eddy Simulation (LES) [19–23]. In LES the large

scales of turbulent motion are simulated directly in the Navier-Stokes equations, but the small scales are modeled in a manner similar to RANS turbulence modeling. Because the larger scales carry most of the momentum and energy, computing them directly should increase the simulation's accuracy. And, since the small scales are dissipative and isotropic, modeling them using a simple eddy viscosity approach appears viable. The scales are separated by spatially filtering the Navier-Stokes equations. This filtering process replaces the equations with a set of resolved (large scale) equations of motion that contain additional unresolved (small scale) terms that must be modeled. The size of the scales that are resolved and that are modeled is determined by the width of the filter, Δ, which is on the order of the grid cell size.

The key to an accurate LES computation is the model used to approximate the unresolved or sub-grid scale terms. There are many forms of these sub-grid scale models. The simplest and most popular model, the Smagorinsky model [24] is similar to Prandtl's mixing length theory [25]. Germano et. al. [26] developed a very successful model which dynamically adjusts this constant based on the local flow conditions. Others [27–30] have modified and improved on these basic ideas.

As with DNS calculations, high order schemes are important for proper and efficient resolution of the large scale structures. In addition, most sub-grid models scale the eddy viscosity by the square of the filter width, which is directly related to the grid size. In second-order accurate numerical schemes the truncation error is also a function of the square of the cell size. LES performed with a second-order accurate code would have a truncation error and a sub-grid model of the same magnitude. And because they both scale with Δ^2 it would be impossible to separate the two by

performing grid refinement. Therefore it is critical to use a higher order accurate numerical method when performing LES computations.

Previous studies [31-33] have applied LES codes to high Reynolds number jet flows. In each of the cited cases, agreement with experimental data has been poor. A common problem with these studies is the overprediction of the length of the jet's potential core. Each solution underpredicts the large scale structures and resultant turbulent mixing. In all three studies the computational domain began at the nozzle exit and a "top-hat" inflow velocity profile was specified. The nozzle geometry and influence of the jet lip was not modeled. Mankbadi et. al. [31] also artificially perturbed the inflow conditions to in an attempt to excite the jet and increase mixing.

1.4 Discussion of the Present Work

The objective of the present work is to accurately predict a high Reynolds number turbulent nozzle flowfield using computational methods and gain an improved understanding of the jet's behavior. A completely new analysis code has been developed for this purpose. To meet the goal of accuracy, the sources of error present in any CFD analysis must be minimized. These errors, discretization error and modeling error are thoroughly investigated.

Discretization error is addressed through the examination of an existing high-order numerical scheme and the development of a new scheme. Care is taken to consider both temporal and spatial accuracy conjointly. Both schemes are then examined analytically through their truncation error and experimentally through numerical experiments to ascertain their performance in solving representative problems. Grid refinement is also examined to show how increased resolution affects the solution.

The largest contribution to the modeling error, modeling of the turbulent structures, is examined fully. The Large-Eddy simulation technique was selected as the most promising method to use. The LES equations are derived in detail and the resulting sub-grid terms are examined. Models for the dominate sub-grid terms are implemented in the flow solver. Boundary conditions and other modeling issues along with correct code implementation are tested using simple validation cases and a representative jet problem.

Using the knowledge gained from testing the codes on simpler problems, a turbulent compressible round jet is simulated. The jet has a Reynolds number of 1.2 million and an exit Mach number of 1.4. A complete description of the jet flowfield including turbulence information is presented. The time averaged flowfield is compared to experimental data to ascertain the accuracy of the simulation. Instantaneous flowfield data and turbulent statistics lend insight into the complex behavior of the jet. Correlation of velocity signals in the jet's mixing layer help quantify the large scale structures present.
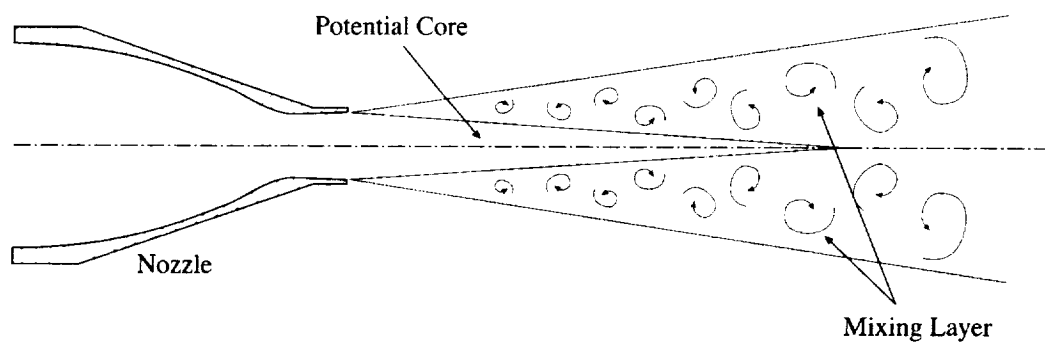
Figure 1.1: Jet schematic

CHAPTER 2

GOVERNING EQUATIONS

The equations governing the flow of the unsteady compressible jet are presented below. The fluid is assumed to be a continuum, which implies that the smallest scales of interest are much larger than the scales of molecular motion.

2.1 The Navier-Stokes Equations

The most general set of equations considered are the three-dimensional Navier-Stokes equations. As presented below, they express the conservation of mass, momentum, and energy for an unsteady compressible fluid in tensor form using cartesian coordinates (x,y,z).

The continuity equation expresses the conservation of mass.

$$\frac{\partial \rho}{\partial t} + \frac{\partial \rho u_i}{\partial x_i} = 0 \tag{2.1}$$

The momentum equation expresses Newton's Second Law. It relates the time rate of change of momentum to the forces applied.

$$\frac{\partial \rho u_i}{\partial t} + \frac{\partial \rho u_i u_j}{\partial x_j} + \frac{\partial p}{\partial x_i} = \frac{\partial \sigma_{ij}}{\partial x_j} \tag{2.2}$$

The stress tensor is defined as

$$\sigma_{ij} = -\tfrac{2}{3}\mu\delta_{ij}S_{kk} + 2\mu S_{ij} \tag{2.3}$$

and the strain rate tensor is

$$S_{ij} = \frac{1}{2}\left(\frac{\partial u_j}{\partial x_i} + \frac{\partial u_i}{\partial x_j}\right) \tag{2.4}$$

Sutherland's Law is used to model the viscosity

$$\mu = \frac{C_1 T^{\frac{3}{2}}}{C_2 + T} \tag{2.5}$$

The constants for μ expressed in English units ($\frac{\text{slugs}}{\text{ft·s}}$) are $C_1 = 2.27 \times 10^{-8}$ and $C_2 = 198.6$.

Conservation of energy expresses the first law of thermodynamics. It relates the time rate of change of energy to the amount of heat added and the work done.

$$\frac{\partial \rho e_t}{\partial t} + \frac{\partial \rho u_i e_t}{\partial x_i} + \frac{\partial u_i p}{\partial x_i} = \frac{\partial u_j \sigma_{ij}}{\partial x_i} - \frac{\partial q_i}{\partial x_i} \tag{2.6}$$

The total energy of the fluid, e_t is defined from the internal energy, $e = c_v T$

$$e_t = e + \tfrac{1}{2}u_i u_i \tag{2.7}$$

The heat flux is represented by

$$q_i = -k\frac{\partial T}{\partial x_i} \tag{2.8}$$

The system of equations is closed using the equation of state for a perfect gas.

$$p = \rho R T \tag{2.9}$$

2.2 Axisymmetric Formulation

A solution to the three-dimensional Navier-Stokes equations requires a large amount of computer memory, storage and CPU time. Taking advantage of the symmetry of a problem is a common technique used in CFD to reduce the computer resources required for an analysis. Since the geometry of the round nozzle is symmetric about its centerline, it may be possible to model the problem using the axisymmetric form of the Navier-Stokes equations. In order for this assumption to be valid the flow field must also be symmetric about the centerline.

The axisymmetric form of the Navier-Stokes equations assumes that there are no gradients or velocity components in the circumferential direction of a cylindrical coordinate system. The symbols x, r, and θ represent the axial, radial, and circumferential directions. The corresponding velocities are represented by u, v, and w. The resulting equations are presented below.

Continuity

$$\frac{\partial \rho}{\partial t} + \frac{\partial \rho u}{\partial x} + \frac{1}{r}\frac{\partial \rho r v}{\partial r} = 0 \tag{2.10}$$

Axial momentum

$$\frac{\partial \rho u}{\partial t} + \frac{\partial \rho u^2}{\partial x} + \frac{1}{r}\frac{\partial \rho r u v}{\partial r} + \frac{\partial p}{\partial x} = \frac{\partial \sigma_{xx}}{\partial x} + \frac{\partial \sigma_{xr}}{\partial r} + \sigma_{xr} - \frac{2}{3}r\frac{\partial}{\partial x}\left(\mu\frac{v}{r}\right) \tag{2.11}$$

Radial momentum

$$\frac{\partial \rho v}{\partial t} + \frac{\partial \rho u v}{\partial x} + \frac{1}{r}\frac{\partial \rho r v^2}{\partial r} + \frac{\partial p}{\partial r} = \frac{\partial \sigma_{xr}}{\partial x} + \frac{\partial \sigma_{rr}}{\partial r} + \sigma_{rr} - \sigma_{\theta\theta} - \frac{2}{3}\mu\frac{v}{r} - \frac{2}{3}r\frac{\partial}{\partial r}\left(\mu\frac{v}{r}\right) \tag{2.12}$$

The components of the stress tensor are

$$\sigma_{xx} = \mu \left(\frac{4}{3} \frac{\partial u}{\partial x} - \frac{2}{3} \frac{\partial v}{\partial r} \right) \tag{2.13a}$$

$$\sigma_{rr} = \mu \left(\frac{4}{3} \frac{\partial v}{\partial r} - \frac{2}{3} \frac{\partial u}{\partial x} \right) \tag{2.13b}$$

$$\sigma_{xr} = \mu \left(\frac{\partial u}{\partial r} + \frac{\partial v}{\partial x} \right) \tag{2.13c}$$

$$\sigma_{\theta\theta} = \mu \left[-\frac{2}{3} \left(\frac{\partial u}{\partial x} + \frac{\partial v}{\partial r} \right) + \frac{4}{3} \frac{v}{r} \right] \tag{2.13d}$$

Energy

$$\frac{\partial \rho e_t}{\partial t} + \frac{\partial \rho e_t u}{\partial x} + \frac{1}{r} \frac{\partial \rho e_t r v}{\partial r} + \frac{\partial p u}{\partial x} + \frac{1}{r} \frac{\partial p r v}{\partial r} = \frac{\partial}{\partial x} \left(u \sigma_{xx} + v \sigma_{xr} - q_x \right)$$

$$+ \frac{\partial}{\partial r} \left(u \sigma_{xr} + v \sigma_{rr} - q_r \right) + u \sigma_{xr} + v \sigma_{rr}$$

$$- q_r - \frac{2}{3} \mu \frac{v^2}{r} - r \frac{\partial}{\partial r} \left(\frac{2}{3} \mu \frac{v^2}{r} \right) - r \frac{\partial}{\partial x} \left(\frac{2}{3} \mu \frac{uv}{r} \right) \tag{2.14}$$

The corresponding heat fluxes are represented by

$$q_x = -k \frac{\partial T}{\partial x} \tag{2.15a}$$

$$q_r = -k \frac{\partial T}{\partial r} \tag{2.15b}$$

2.3 Flux Vector Forms

For CFD, it is helpful to recast the equations in flux vector form. This puts all the equations the same form for easy discretization and solution.

2.3.1 Three-dimensional

The flux vector form of the three-dimensional Navier-Stokes equations is

$$\frac{\partial Q}{\partial t} + \frac{\partial E}{\partial x} + \frac{\partial F}{\partial y} + \frac{\partial G}{\partial z} = \frac{\partial E_v}{\partial x} + \frac{\partial F_v}{\partial y} + \frac{\partial G_v}{\partial z} \tag{2.16}$$

where

$$Q = \begin{bmatrix} \rho \\ \rho u \\ \rho v \\ \rho w \\ \rho \epsilon_t \end{bmatrix}$$

$$E = \begin{bmatrix} \rho u \\ \rho u^2 + p \\ \rho u v \\ \rho u w \\ (\rho \epsilon_t + p) u \end{bmatrix} \qquad E_v = \begin{bmatrix} 0 \\ \sigma_{xx} \\ \sigma_{xy} \\ \sigma_{xz} \\ u\sigma_{xx} + v\sigma_{xy} + w\sigma_{xz} - q_x \end{bmatrix}$$

$$F = \begin{bmatrix} \rho v \\ \rho v u \\ \rho v^2 + p \\ \rho v w \\ (\rho \epsilon_t + p) v \end{bmatrix} \qquad F_v = \begin{bmatrix} 0 \\ \sigma_{yx} \\ \sigma_{yy} \\ \sigma_{yz} \\ u\sigma_{yx} + v\sigma_{yy} + w\sigma_{yz} - q_y \end{bmatrix}$$

$$G = \begin{bmatrix} \rho w \\ \rho w u \\ \rho w v \\ \rho w^2 + p \\ (\rho \epsilon_t + p) w \end{bmatrix} \qquad G_v = \begin{bmatrix} 0 \\ \sigma_{zx} \\ \sigma_{zy} \\ \sigma_{zz} \\ u\sigma_{zx} + v\sigma_{zy} + w\sigma_{zz} - q_z \end{bmatrix}$$

2.3.2 Axisymmetric

The axisymmetric equations are similar to the three-dimensional form with the addition of a source term. When the source term H is omitted, the equations simplify to the two-dimensional/planar form.

$$\frac{\partial Q}{\partial t} + \frac{\partial E}{\partial x} + \frac{\partial F}{\partial y} + H = \frac{\partial E_v}{\partial x} + \frac{\partial F_v}{\partial y} + H_v \qquad (2.17)$$

where

$$Q = \begin{bmatrix} \rho \\ \rho u \\ \rho v \\ \rho \epsilon_t \end{bmatrix}$$

$$E = \begin{bmatrix} \rho u \\ \rho u^2 + p \\ \rho u v \\ (\rho e_t + p)\, u \end{bmatrix} \qquad\qquad E_v = \begin{bmatrix} 0 \\ \sigma_{xx} \\ \sigma_{xr} \\ u\sigma_{xx} + v\sigma_{rx} - q_x \end{bmatrix}$$

$$F = \begin{bmatrix} \rho v \\ \rho v u \\ \rho v^2 + p \\ (\rho e_t + p)\, v \end{bmatrix} \qquad\qquad F_v = \begin{bmatrix} 0 \\ \sigma_{rx} \\ \sigma_{rr} \\ u\sigma_{xr} + v\sigma_{rr} - q_r \end{bmatrix}$$

$$H = \frac{1}{r}\begin{bmatrix} \rho v \\ \rho u v \\ \rho v^2 \\ (\rho e_t + p)\, v \end{bmatrix} \qquad H_v = \begin{bmatrix} 0 \\ \sigma_{xr} - \frac{2}{3} r \frac{\partial}{\partial r}\left(\mu \frac{v}{r} \right) \\ \sigma_{rr} - \sigma_{\theta\theta} - \frac{2}{3}\mu \frac{v}{r} - \frac{2}{3} r \frac{\partial}{\partial r}\left(\mu \frac{v}{r} \right) \\ u\sigma_{xr} + v\sigma_{rr} - q_r - \frac{2}{3}\mu \frac{v^2}{r} - r\frac{\partial}{\partial r}\left(\frac{2}{3}\mu \frac{v^2}{r} \right) - r\frac{\partial}{\partial x}\left(\frac{2}{3}\mu \frac{uv}{r} \right) \end{bmatrix}$$

CHAPTER 3

NUMERICAL METHODS

The governing equations are solved using two explicit finite difference methods, a MacCormack type predictor-corrector method and a Runge-Kutta method. Both types of schemes are in wide use today for fluid dynamic and acoustic analyses of nozzle flows. Each scheme has an associated set of strengths and weaknesses which will be discussed later in this document.

The numerical schemes will be presented in terms of a one-dimensional model equation

$$\frac{\partial q}{\partial t} + \frac{\partial f}{\partial x} = 0 \tag{3.1}$$

where $f = f(q)$. Extending the schemes to the Navier-Stokes equations (2.16 & 2.17) is a straight-forward matter.

3.1 Predictor-Corrector Schemes

MacCormack developed a two-step explicit finite difference method [34] which is a variant of the Lax-Wendroff scheme [35]. This method is very easy to understand and implement and hence has become very popular in the CFD community. The scheme is very robust and requires only two storage locations for each dependent variable

(2-N storage). As a consequence several variants of the MacCormack technique have been developed. The original technique and a higher order variant will be discussed.

3.1.1 MacCormack 2-2 Scheme

MacCormack's original scheme is second order accurate in both time and space. That is to say the truncation error of the scheme is proportional to both the time step and spatial step to the second power.

The first stage, or predictor step, computes the solution at an intermediate time based on the solution at the previous time step. It uses a one-sided forward difference for the spatial derivative.

$$q_i^* = q_i^n - \frac{\Delta t}{\Delta x} \left(f_{i+1}^n - f_i^n \right) \tag{3.2a}$$

The second stage, or corrector step, computes the solution at the end of the time step based on the solution at the intermediate time. It uses a one-sided backward difference for the spatial derivative.

$$q_i^{n+1} = \frac{1}{2} \left[q_i^n + q_i^* - \frac{\Delta t}{\Delta x} \left(f_i^* - f_{i-1}^* \right) \right] \tag{3.2b}$$

The leading truncation error terms for MacCormack's scheme are

$$-\frac{(\Delta t)^2}{6} \frac{\partial^3 q}{\partial t^3} - \frac{(\Delta x)^2}{6} \frac{\partial^3 f}{\partial x^3} - \frac{\Delta t (\Delta x)^2}{24} A \frac{\partial^4 f}{\partial x^4} \tag{3.3}$$

where f has been linearized by $f = Aq$. The error associated with the temporal and spatial terms are dispersive in nature, while the error associated with the cross term is dissipative. This dissipative term is scaled by the time step.

3.1.2 Gottlieb-Turkel 2-4 Scheme

Gottlieb and Turkel [9] modified MacCormack's scheme to be fourth-order accurate in space while retaining the second-order time accuracy. They simply modified

the difference stencil of the spatial derivative to achieve higher accuracy.

$$q_i^* = q_i^n - \frac{1}{6} \frac{\Delta t}{\Delta x} \left(-f_{i+2}^n + 8 f_{i+1}^n - 7 f_i^n \right) \tag{3.4a}$$

$$q_i^{n+1} = \frac{1}{2} \left[q_i^n + q_i^* - \frac{1}{6} \frac{\Delta t}{\Delta x} \left(7 f_i^* - 8 f_{i-1}^* + f_{i-2}^* \right) \right] \tag{3.4b}$$

The leading terms in the truncation error for the Gottlieb-Turkel scheme are

$$-\frac{(\Delta t)^2}{6} \frac{\partial^3 q}{\partial t^3} + \frac{(\Delta x)^4}{30} \frac{\partial^5 q}{\partial x^5} - \frac{\Delta t (\Delta x)^2}{18} A \frac{\partial^4 f}{\partial x^4} \tag{3.5}$$

In addition to retaining the second-order time accuracy, it is important to note that the cross term is dissipative and is scaled by $\Delta t (\Delta x)^2$. Bayliss et. al. [36] extended this scheme to the solution of the Navier-Stokes equations.

3.2 Runge-Kutta Schemes

As seen with the Gottlieb-Turkel scheme, all higher order variants of MacCormack's method maintain second-order time accuracy. It will be shown later that one cannot separate the temporal and spatial accuracy. They are clearly equated through equation (3.1).

A true fourth-order accurate scheme in both time and space has been developed. A fourth-order central difference for the spatial derivative is combined with a fourth-order Runge-Kutta time stepping scheme.

Runge-Kutta schemes are a popular family of numerical schemes with higher order temporal accuracy. These multi-stage schemes can be formulated for any order of accuracy. The number of stages in the scheme is equal to or greater than the desired order of accuracy. Two fourth-order Runge-Kutta schemes are investigated.

3.2.1 Standard Scheme

The standard four-stage fourth-order scheme as given by Jameson [37] is

$$
\begin{aligned}
q_0 &= q^n \\[4pt]
q_1 &= q^n - \frac{1}{4}\Delta t \mathbf{D}\,(q_0) \\[4pt]
q_2 &= q^n - \frac{1}{3}\Delta t \mathbf{D}\,(q_1) \\[4pt]
q_3 &= q^n - \frac{1}{2}\Delta t \mathbf{D}\,(q_2) \\[4pt]
q^{n+1} &= q^n - \Delta t \mathbf{D}\,(q_3)
\end{aligned}
\tag{3.6}
$$

The operator $\mathbf{D}$ is the spatial finite difference operator. For equation 3.1, $\mathbf{D}\,(q)$ would be a fourth-order finite difference stencil for $-\frac{\partial f}{\partial x}$. A central difference stencil for $\frac{\partial f}{\partial x}$ is used here.

$$
\frac{\partial f}{\partial x} = \frac{-f_{i+2} + 8f_{i+1} - 8f_{i-1} + f_{i-2}}{12(\Delta x)}
\tag{3.7}
$$

This scheme requires two storage locations for each dependent variable (2-N storage). The leading terms in the truncation error for this scheme are

$$
-\frac{(\Delta t)^4}{120}\frac{\partial^5 q}{\partial t^5} + \frac{(\Delta x)^4}{30}\frac{\partial^5 q}{\partial x^5} - \frac{\Delta t(\Delta x)^4}{30}A\frac{\partial^6 f}{\partial x^6}
\tag{3.8}
$$

3.2.2 Low Dispersion Scheme

Several researchers [38–41] have developed alternative Runge-Kutta schemes that have a lower dispersion error than the standard scheme leading to greater stability and accuracy. To accomplish this, additional stages are required. The additional stages provide a means to impose the additional constraints necessary to minimize the error. All of the schemes are based on a general M-stage 2-N storage formulation

given by

$$dq_m = \alpha_m dq_{m-1} + \Delta t \mathbf{D}(q_{m-1})$$ (3.9a)

$$q_m = q_{m-1} + \beta_m dq_m$$ (3.9b)

for $m = 1 \dots M$. and where $q_0 = q^n$ and $q_M = q^{n+1}$. The coefficient α_1 is typically set to zero for the algorithm to be self-starting. Again, the operator $\mathbf{D}$ is the spatial finite difference operator.

Carpenter and Kennedy's five-stage fourth-order scheme [38] was chosen for its fourth-order accuracy, low number of stages, and ease of programming. The coefficients for the scheme are given in table 3.1

stage (m)	α_m	β_m
1	0.00000000000	0.1496590219993
2	-0.41789047450	0.3792103129999
3	-1.192151694643	0.8229550293869
4	-1.697784692471	0.6994504559488
5	-1.514183444257	0.1530572479681

Table 3.1: Coefficients for fourth-order low-dispersion Runge-Kutta scheme

The leading terms in the truncation error for this scheme are

$$-\frac{(\Delta t)^4}{300}\frac{\partial^5 q}{\partial t^5} + \frac{(\Delta x)^4}{30}\frac{\partial^5 q}{\partial x^5} - \frac{\Delta t(\Delta x)^4}{30}A\frac{\partial^6 f}{\partial x^6}$$ (3.10)

The dispersive error term due to the time step (the first term) is two and one-half times smaller than the standard fourth-order scheme's error (3.8).

3.3 Fourier Analysis of Numerical Schemes

In the field of high order numerical methods for DNS and LES, the proper resolution of the waves present in the flowfield is critical. A popular method to assess the ability of a numerical scheme to resolve waves is the Fourier analysis of the semi-discretized equation (spatial discretization only) [42].

The semi-discretization of equation 3.1 is

$$\frac{\partial q_n}{\partial t} = \mathbf{D}\left(q_n\right) \tag{3.11}$$

where q_n is the discrete solution. We choose a sinusoidal trial solution with wave number ω, which has the form

$$q_n(\omega, t) = v(\omega, t)e^{i\omega x_n} \tag{3.12}$$

We substitute 3.12 into 3.11 and solve for $v(\omega, t)$. The resulting solution of the equation is

$$q_n(\omega, t) = v(\omega, 0)e^{\mathbf{Re}\left[\hat{D}(\omega)t\right]}e^{i\omega(x_n - c^* t)} \tag{3.13a}$$

with

$$c^* = -\frac{1}{\omega}\mathbf{Im}\left[\hat{D}(\omega)t\right] \tag{3.13b}$$

where $\hat{D}(\omega)$ are the eigenvalues of $\mathbf{D}$. The exact solution to equation 3.1 is

$$q(\omega, t) = v(\omega, 0)e^{i\omega(x - ct)} \tag{3.14}$$

By comparing the numerical and exact solutions we can see how the numerical scheme affects the propagation of the wave. The exact solution (equation (3.14)) shows that

amplitude of the wave should not change. However, in the numerical solution the amplitude is a function of time (equation (3.13a)). Therefore,

$$\text{if } \mathbf{Re}\left[\hat{D}(\omega)\right] = 0, \text{ then the scheme is conservative}$$

$$\text{if } \mathbf{Re}\left[\hat{D}(\omega)\right] < 0, \text{ then the scheme is dissipative}$$

$$\text{if } \mathbf{Re}\left[\hat{D}(\omega)\right] > 0, \text{ then the scheme is unstable}$$

Similarly, comparing the numerical wave speed c^* to the exact wave speed c we find

$$\text{if } \frac{c^*}{c} = 1, \text{ then the scheme has no phase error}$$

$$\text{if } \frac{c^*}{c} \neq 1, \text{ then the scheme introduces a phase error}$$

To achieve a conservative scheme ($\mathbf{Re}\left[\hat{D}(\omega)\right] = 0$) the matrix $\mathbf{D}$ must be anti-symmetric. Central difference schemes, such as those used here, satisfy this criteria. Upwind schemes, which are dissipative, do not have an anti-symmetric matrix and were not considered suitable for this study. The wave speed relative to the exact speed for each scheme considered here is

$$\frac{c^*}{c} = \frac{sin(\omega\Delta x)}{\omega\Delta x} \qquad \text{, for second-order spatial accuracy}$$

(3.15a)

$$\frac{c^*}{c} = \frac{-\frac{1}{3}sin(\omega\Delta x)cos(\omega\Delta x) + \frac{4}{3}sin(\omega\Delta x)}{\omega\Delta x} \qquad \text{, for fourth-order spatial accuracy}$$

(3.15b)

Figure 3.1 compares the error in the wave speeds for second- and fourth-order accurate central difference operators, $\mathbf{D}$. The error is a function of the wave number, ω, and grid resolution, Δx. From this Fourier analysis perspective the numerical scheme can be seen to act as a spectral filter of the exact solution. This error is sometimes plotted as numerical wave number versus exact wave number ($\omega^*\Delta x$ versus

$\omega\Delta x$. figure 3.2). It is clear that higher order schemes can resolve higher wave number waves with less grid resolution. But, neither scheme can adequately resolve very high wave numbers. even with very fine grid resolution.

If one determines an acceptable error in wave speed for their calculation. the maximum value of $\omega\Delta x$ that provides this error can be related to the number of grid points per wavelength necessary to accurately resolve a wave [43].

$$N = \frac{2\pi}{(\omega\Delta x)_{max}} \qquad (3.16)$$

The wave will be properly resolved if it is captured by at least N points. This "points per wavelength" has become a popular measure of a scheme's "goodness". But, this measure does not consider the error due to time discretization and the computational cost of the scheme.

3.4 Filtering

Both numerical methods introduce a dispersive error into the solution. This error manifests itself in two ways. First, as shown above, waves that are that are not resolved with enough grid points have their speeds altered. Secondly, new high wave number waves are introduced into the solution. If unchecked, these errors can grow and cause the analysis to become unstable. To damp out these waves, an artificial dissipation term is typically added to the equations [44–47]. All these "classical" techniques involve the use of a user specified constant that scales the effect of the dissipation. The value of this constant is somewhat arbitrary and varies widely between cases.

In this study a solution filtering technique is used. This technique can be regarded in two ways. In the classical sense, solution filtering simply adds a dissipative term to

the equations to damp the unwanted waves. From a Fourier analysis perspective, this technique filters the high wave number components out of the solution. A properly selected filter removes both the numerically introduced waves and the poorly resolved waves, leaving only the portions of the flowfield that are accurately modeled. Several researchers have developed solution filters for CFD including [10,42,48,49]. The explicit filters of Kennedy and Carpenter [48] were chosen for their ease of implementation and clear relation to the unfiltered solution. The filtered solution is simply the unfiltered solution plus a dissipative term.

$$\hat{q}_i = q_i - \alpha_D(\Delta x)^{2n}\frac{\partial^{2n}q_i}{\partial x^{2n}} \qquad (3.17)$$

where $\alpha_D = \frac{(-1)^n}{2^{2n}}$ and $n = 1, 2, \ldots$. Kennedy and Carpenter developed a family of filters with corresponding boundary stencils for $n = 1 \ldots 7$. These filters are implemented in the analysis code. By choosing the order of the filter, $2n$, to be larger than the order of accuracy of the numerical scheme, one can insure that the filter does not overly influence the numerical solution. The response of the filters is shown in figure 3.3. As the order of the filter is increases the cut-off wave number of the filter is increased and a greater portion of the domain remains unmodified.

Examples of the effect of solution filtering are shown in figures 3.4 and 3.5. A sine wave on the domain $0 \le x \le \pi$ was filtered 100,000 times (a typical number of iterations for a jet calculation). To illustrate how increased grid resolution reduces the effect of the filter, sine waves made up of 5, 15, 25, 35, and 45 points ($\omega\Delta x = 1.257$, 0.4189, 0.2513, 0.1795, and 0.1396) were filtered using fourth-, sixth-, and eighth-order filters. Figure 3.4 shows that increasing the resolution of the wave reduces the

effect of the filter. Poorly resolved waves can be completely eliminated (the fourth-order filter completely removes the 5 point resolved wave) Figure 3.5 shows how the resolved wave number increases with the order of the filter. A wave resolved by five points was filtered with fourth-, sixth-. eighth-. tenth-. twelfth-. and fourteenth-order filters. The wave ($\omega \Delta x = 1.257$) is completely removed by the fourth order filter. but damped less than 10 percent by the tenth-order filter. and maintained exactly by the fourteenth-order filter.
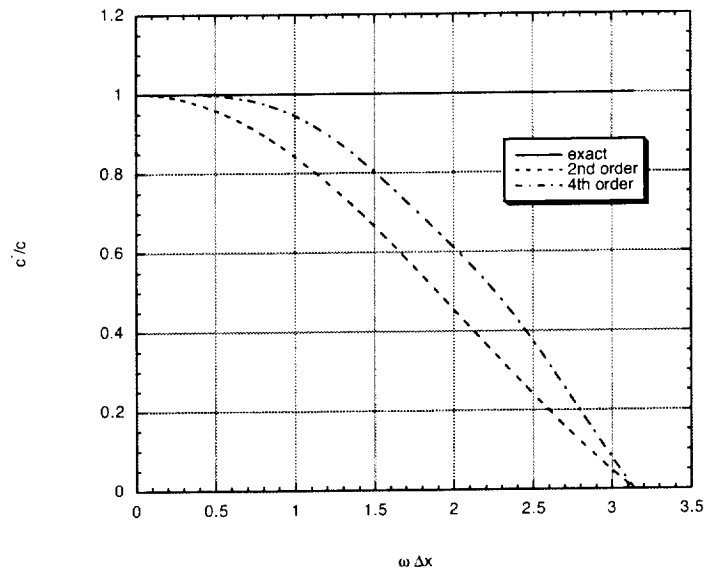
Figure 3.1: Error in wave speed
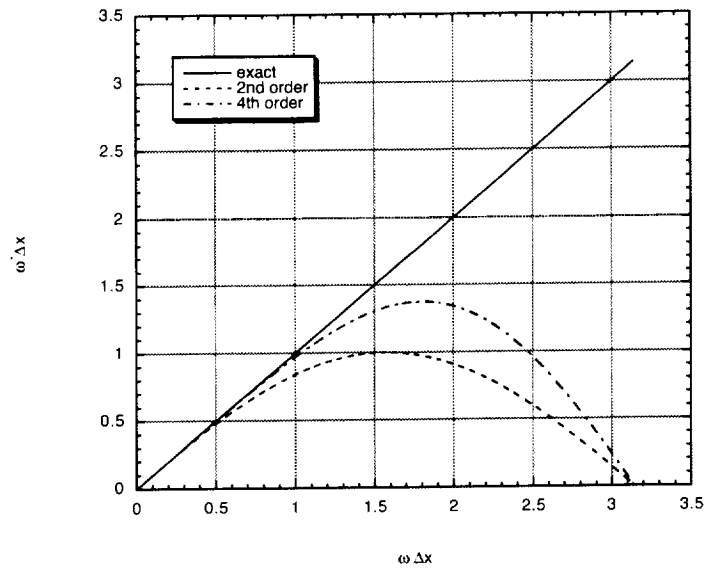
Figure 3.2: Error in wave number
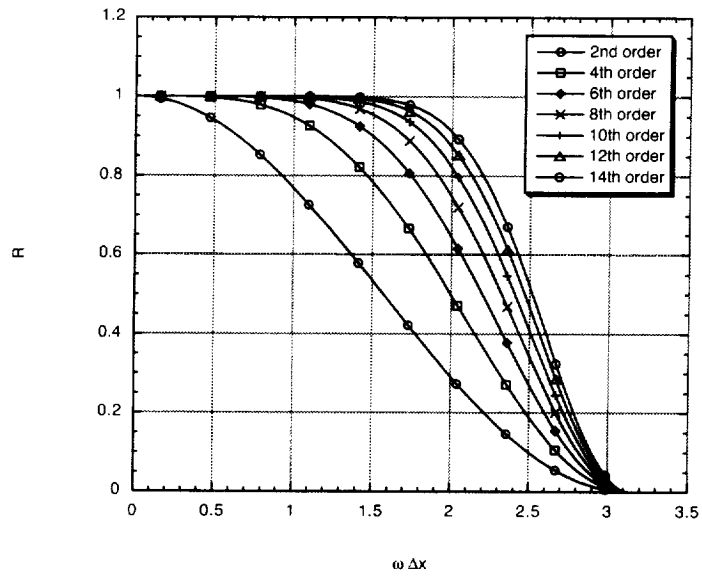
Figure 3.3: Filter response
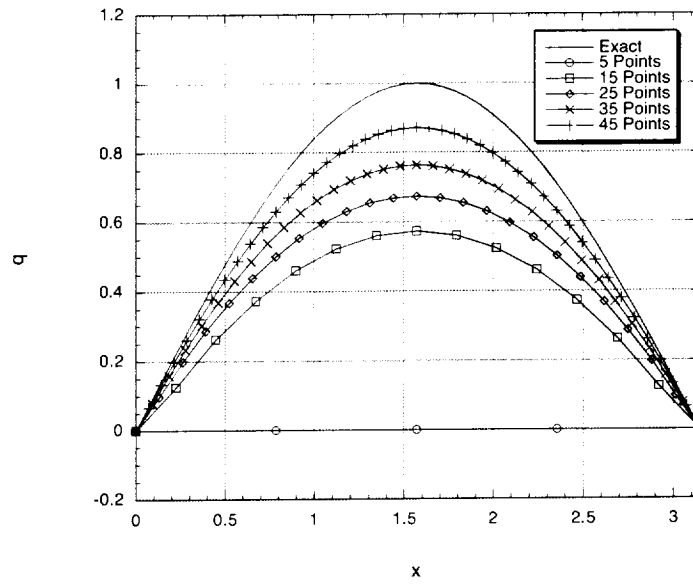
(a) fourth-order filter
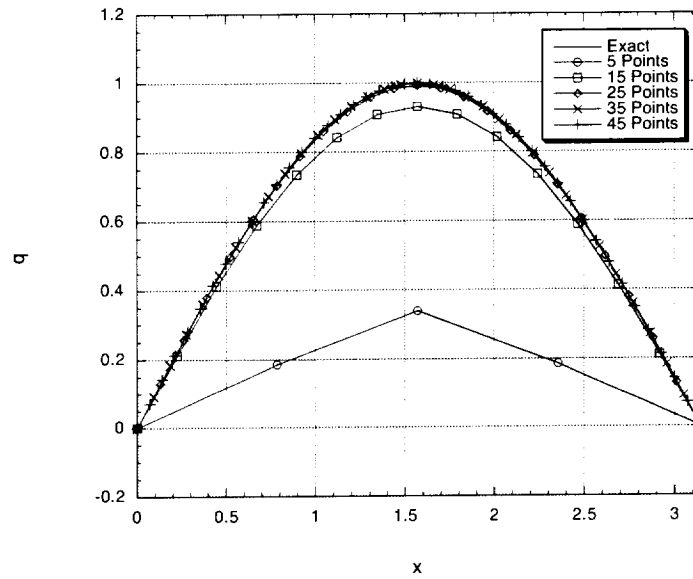
(b) sixth-order filter

Figure 3.4: Effect of grid resolution on filter response

Figure 3.4: continued
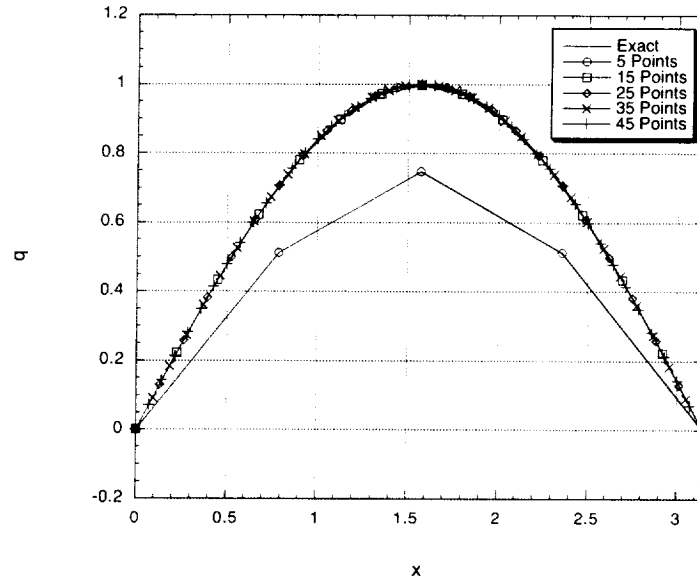
(c) eight-order filter
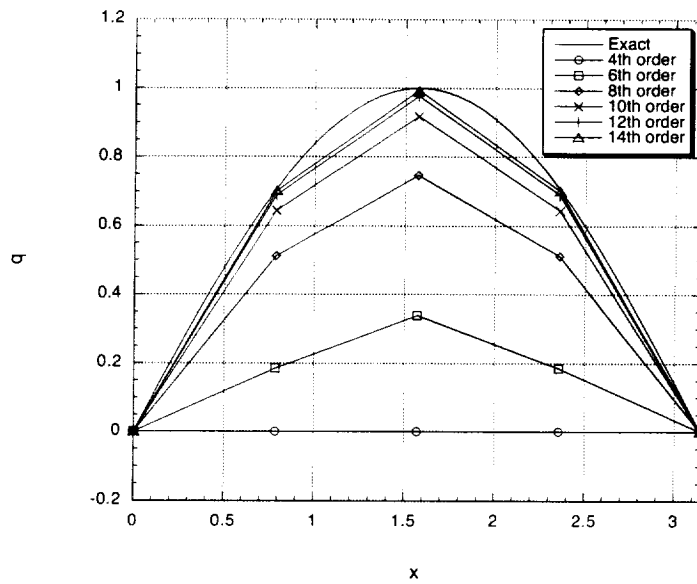
Figure 3.5: Effect of filter order on a five point wave

CHAPTER 4

1-D ERROR ANALYSIS

The behavior of the numerical schemes presented in Chapter 3 is examined for three one-dimensional model problems. Truncation error, efficiency, and the consequence of disparate temporal and spatial accuracy are discussed. The schemes are used to solve the one-dimensional inviscid convection of a gaussian pulse.

The accuracy of these schemes is commonly expressed separately in terms of spatial and temporal accuracy. A great deal of effort has focused on increasing the spatial accuracy of a numerical scheme without regard to the temporal accuracy. This chapter examines the behavior of two commonly used schemes in terms of truncation error and computational cost on a model equation. Particular attention is paid to the truncation error of the schemes and how the spatial and temporal errors affect the overall order of accuracy of the scheme.

Three one-dimensional problems were used to test the accuracy and efficiency of the schemes. All three are based on the model equation (3.1).

4.1 Problem Descriptions

4.1.1 Problem 1

The first problem is the linear convection of a gaussian pulse, where $q = f = u$.

$$\frac{\partial u}{\partial t} + \frac{\partial u}{\partial x} = 0 \tag{4.1}$$

The initial condition is given by

$$u(x,0) = u_0(x) = \frac{1}{2}e^{-ln(2)\left(\frac{x}{3}\right)^2} \tag{4.2}$$

The domain is $-20 \leq x \leq 450$ and the solution is run for $0 \leq t \leq 400$. An exact solution to this problem exists and is given by

$$u_{ex}(x,t) = u_0(x - t) \tag{4.3}$$

4.1.2 Problem 2

The second problem is nonlinear where $q = u$ and $f = \frac{1}{2}u^2$.

$$\frac{\partial u}{\partial t} + \frac{\partial}{\partial x}\left(\frac{u^2}{2}\right) = 0 \tag{4.4}$$

The initial conditions and simulation time are set so that a smooth final solution is obtained. The initial condition is

$$u(x,0) = u_0(x) = \frac{1}{8}e^{-ln(2)\left(\frac{x}{10}\right)^2} \tag{4.5}$$

The domain is $-50 \leq x \leq 50$ and the solution is run for $0 \leq t \leq 100$. A numerical approximation to the exact solution is obtained using the method of characteristics.

4.1.3 Problem 3

The third problem is also nonlinear (equation (4.4)), but the initial conditions and time of the simulation are set so that the pulse is allowed to coalesce into a shock.

$$u(x,0) = u_0(x) = \tfrac{1}{2}e^{-ln(2)\left(\frac{x}{5}\right)^2} \tag{4.6}$$

The domain is $-50 \leq x \leq 50$ and the solution is run for $0 \leq t \leq 200$. Like problem 2, a numerical approximation to the exact solution is obtained using the method of characteristics. The location of the shock is then fitted in the exact solution using Whitham's area rule [50].

4.2 Results

All the one-dimensional calculations were run on an Apple Macintosh Powerbook G3 computer with a 266MHz PowerPC G3 processor.

The standard scheme was used for all the Runge-Kutta results in this section.

The error of the numerical scheme was measured by the l_2 norm, which is computed as follows

$$l_2 = \left[\frac{x_{max} - x_{min}}{n-1} \sum_{i=1}^{n} (u_i - u_{ex_i})^2 \right]^{\frac{1}{2}} \tag{4.7}$$

For each problem, both numerical schemes were run to determine the maximum stable time step. Then, each scheme was run at a number of different values of $\frac{\Delta t}{\Delta x}$ as the spatial step was halved.

4.2.1 Problem 1

A sample solution to the linear problem for both numerical schemes is presented in figure 4.1. The Runge-Kutta scheme shows better agreement with the exact solution

than the Gottlieb-Turkel scheme. Error from the Gottlieb-Turkel scheme is plotted versus spatial step and time step (figure 4.2). The terminal slope of the line, p indicates the order of accuracy of the scheme and is listed in the plot legend. The slopes in figure 4.2(a) show that the error is of second-order accuracy for the varying spatial step. Only where the time step is much smaller than the spatial step does the scheme behave as a fourth-order scheme. Also, the error is dependent on the time step chosen. This is due to the third term in the truncation error (equation (3.5)). Clearly, this dissipative error is significant. Figure 4.2(b), shows the error behavior with the time step. Again, the scheme is only second-order accurate except when the time step is very small compared to the spatial step. In order to obtain fourth-order behavior from the Gottlieb-Turkel scheme, the error due to the time step must be reduced at the same rate as the error due to the spatial step. In order to accomplish this, the time step must be reduced by a factor of $\frac{1}{4}$ as the spatial step is reduced by $\frac{1}{2}$. Figure 4.3 verifies that when adjusting the time step in this manner fourth-order accuracy is obtained.

Results for Runge-Kutta scheme, on the linear problem (figure 4.4), indicate that the scheme is truly a fourth-order accurate scheme. In addition, except for the highest value of $\frac{\Delta t}{\Delta x}$ where the time error term dominates, the error is independent of time step.

The efficiency of a numerical scheme can be seen by comparing the l_2 error against the time required to obtain that error level [51]. Both schemes are compared at their maximum stable time step. Figure 4.5 shows that the Runge-Kutta scheme is superior to the Gottlieb-Turkel scheme. Runge-Kutta achieves an equivalent error level in about an order of magnitude less time than the Gottlieb-Turkel scheme. This result

is due to the lower truncation error and larger allowable time step of the Runge-Kutta scheme. Reducing the time step of the Gottlieb-Turkel scheme to maintain fourth-order accuracy increases the accuracy but also increases the computational cost.

4.2.2 Problem 2

Sample solutions to the smooth nonlinear problem for both numerical schemes are presented in figure 4.6. Because a short simulation time was necessary to maintain a smooth solution, the differences between the exact solution and numerical solutions are not discernible on the plot. Error data for the smooth nonlinear problem are shown in figures 4.7–4.10. The effects of round-off error, the reduction in accuracy/slope at small Δt and Δx, make it difficult to report a terminal slope, instead the maximum slope was used. The trends for the nonlinear analysis are similar to the linear case. However, the benefit for using the Runge-Kutta scheme is somewhat less. But, at large time steps, for maximum efficiency, the Runge-Kutta scheme is superior.

4.2.3 Problem 3

Solutions to the nonlinear problem with a shock (figure 4.11) show that both schemes produce high frequency oscillations near the discontinuity. This problem does not provide useful error information and illustrates the limitations of finite difference schemes. The presence of the discontinuity reduces the accuracy of all schemes to first-order (figures 4.12 & 4.13). Results from the Gottlieb-Turkel scheme indicate that the third term in equation (3.5) provides a damping effect on the numerical oscillations that occur near the shock. This damping allowed the scheme to obtain a converged answer. Figure 4.12 shows that larger time steps yielded lower errors for

this problem. The dissipative term in the truncation error is scaled with the time step and larger time steps resulted in greater dissipation of the non-physical oscillations.

To obtain useful solutions to this problem, the Runge-Kutta scheme required some form of artificial dissipation. The solution filtering technique of Kennedy and Carpenter [48] was used. Filtering adds to the solution an additional dissipative term that removes high frequency numerical oscillations while leaving the low frequency physical oscillations untouched.

The order of the filter, $2n$ in equation (3.17), determines the magnitude of the dissipation added and the range of frequencies which are damped. If the order of the filter is larger than the order of the truncation error of the numerical scheme, then the filter should have a negligible effect on the solution error. Increasing the order of the filter increases the range of frequencies which are untouched by the filter. Figure 4.13 shows that the filters remove the non-physical oscillations from the solution and greatly reduce the error of the scheme. The insensitivity of the error to the order of the filter indicates that the truncation error of the scheme is greater than the dissipative term of the filter and that the numerical oscillations have frequencies higher than frequency range of the highest order filter.

Figure 4.1: Solution to linear convection problem

(a) Spatial error

(b) Temporal error

Figure 4.2: Error of Gottlieb-Turkel scheme for the linear problem

Figure 4.3: Improved spatial error of Gottlieb-Turkel scheme for the linear problem

(a) Spatial error

(b) Temporal error

Figure 4.4: Error of Runge-Kutta scheme for the linear problem
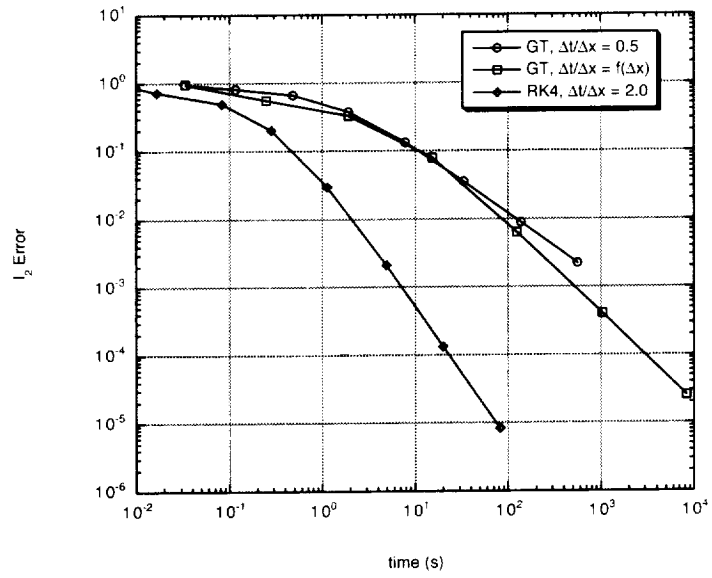
Figure 4.5: Efficiency of the numerical schemes for the linear convection problem
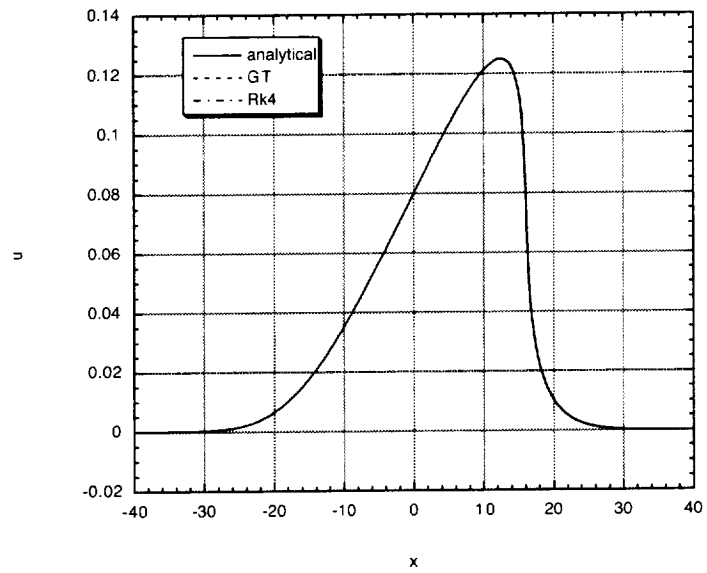
Figure 4.6: Solution to smooth nonlinear convection problem
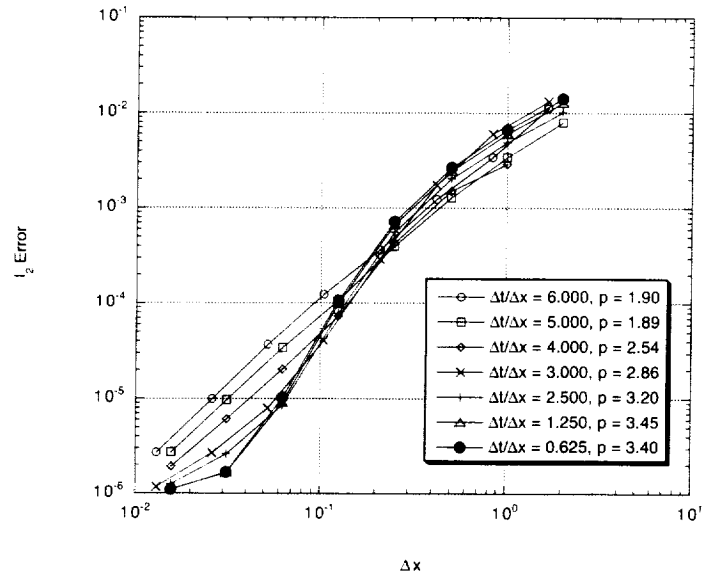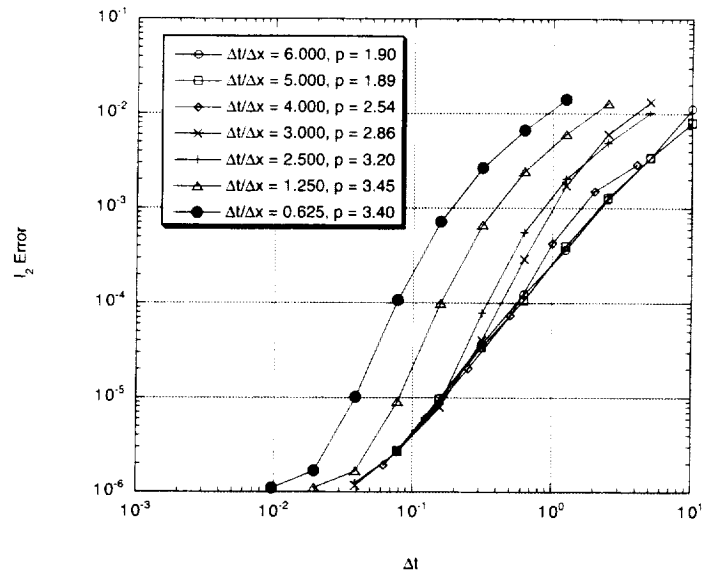
(a) Spatial error

(b) Temporal error

Figure 4.7: Error of Gottlieb-Turkel scheme for the smooth nonlinear problem
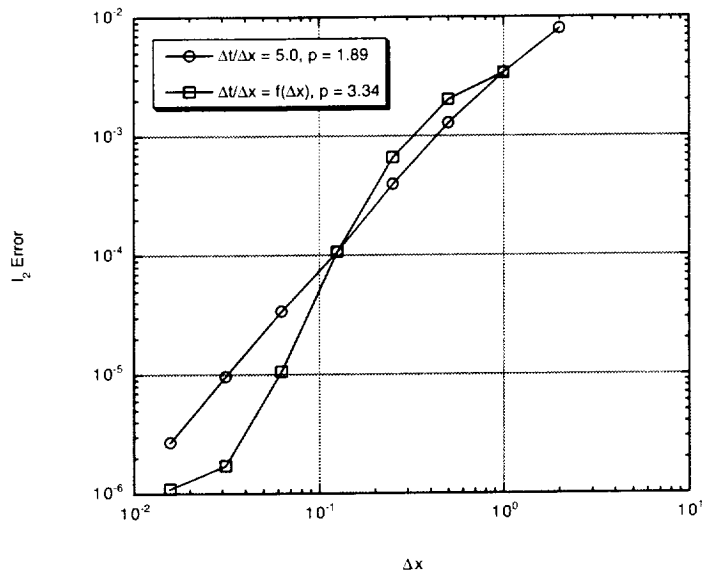
Figure 4.8: Improved spatial error of Gottlieb-Turkel scheme for the smooth nonlinear problem
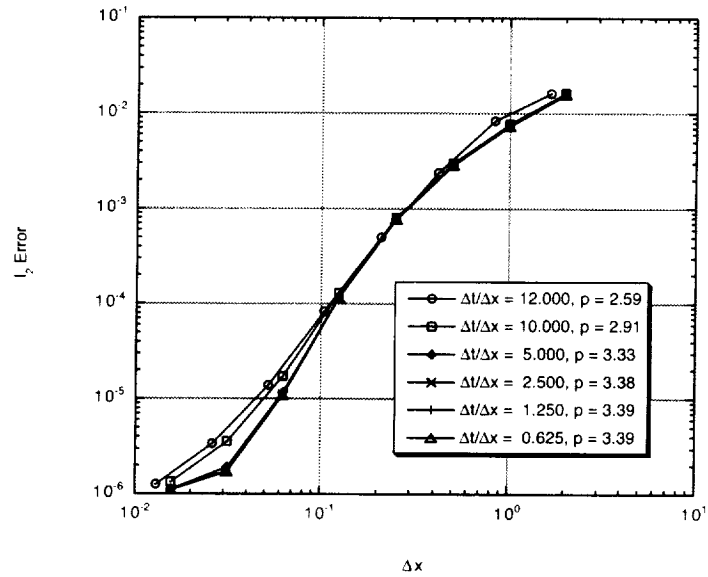
(a) Spatial error
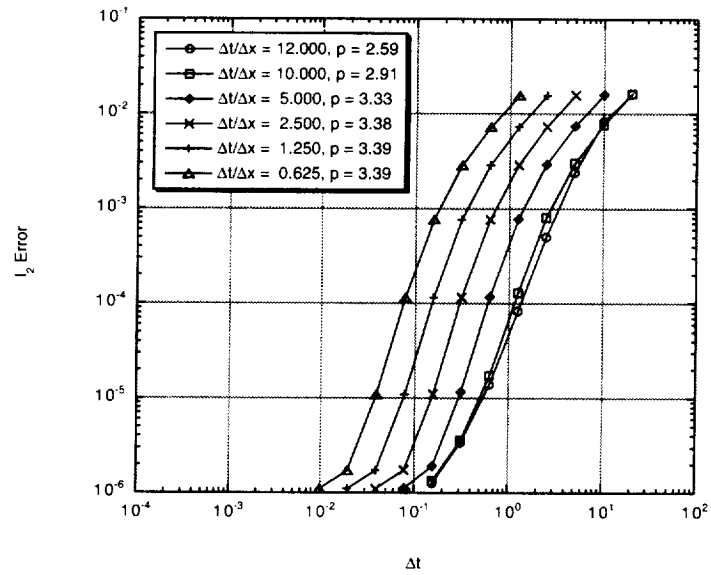
(b) Temporal error

Figure 4.9: Error of Runge-Kutta scheme for the smooth nonlinear problem
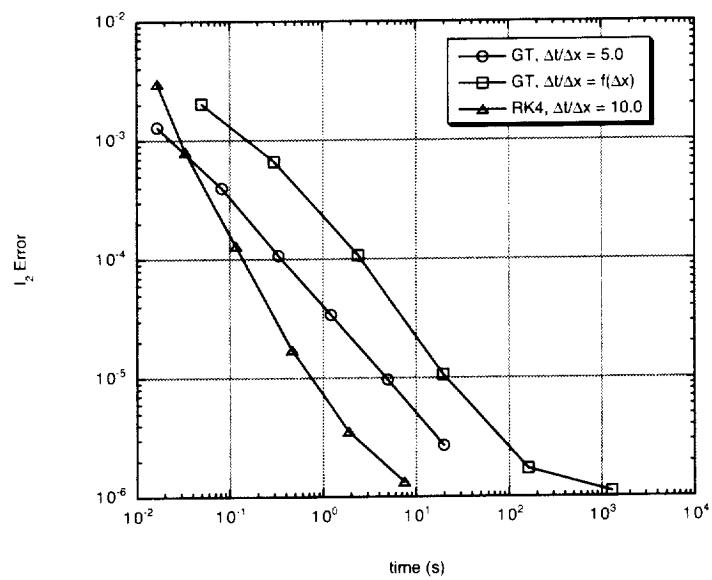
Figure 4.10: Efficiency of the numerical schemes for the linear convection problem
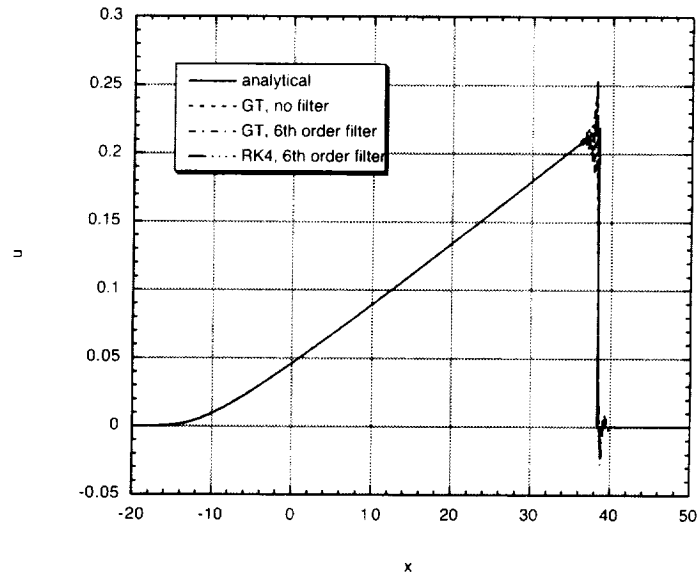
(a) Complete wave
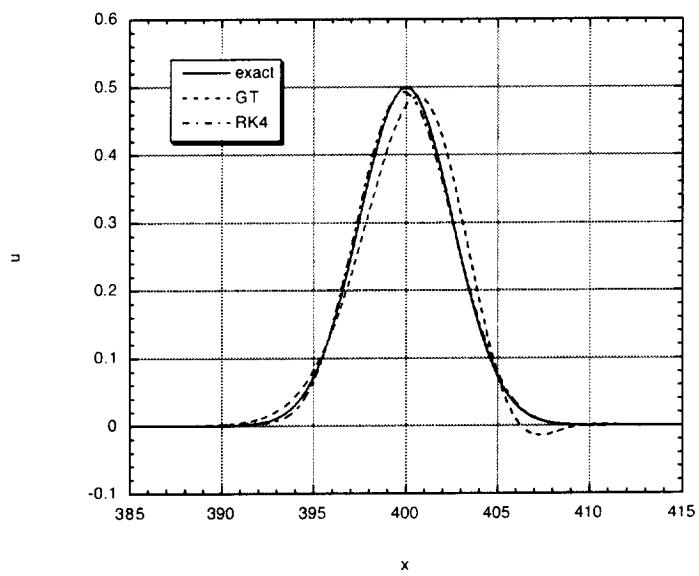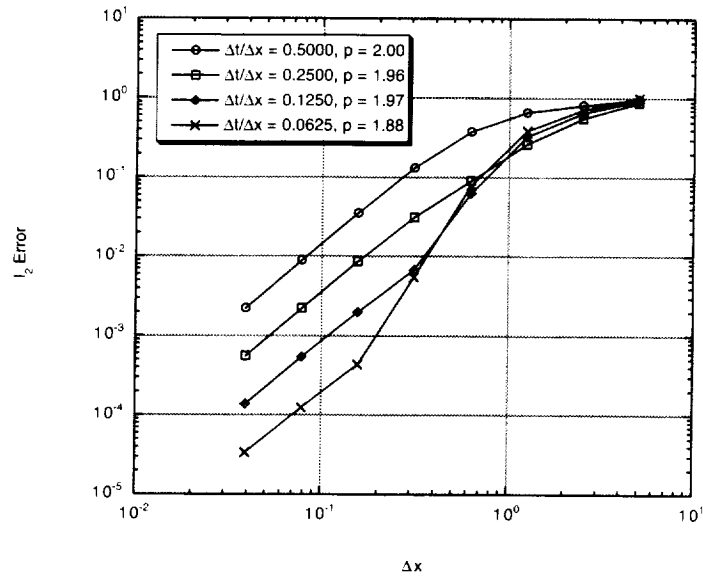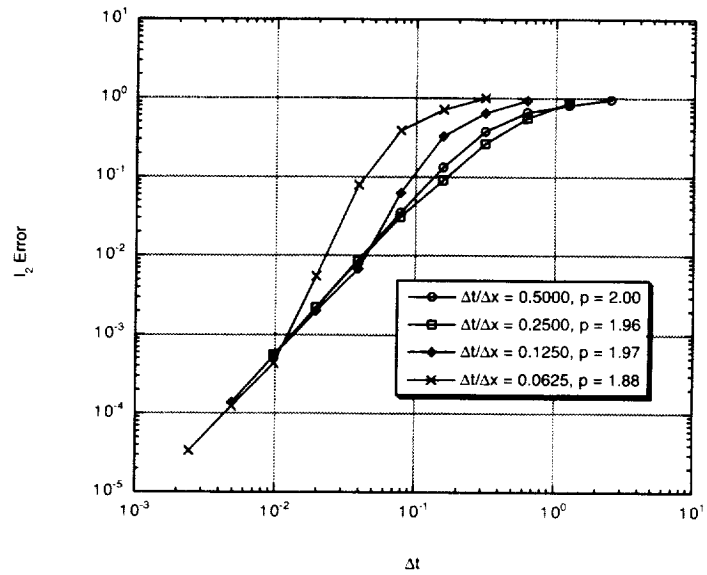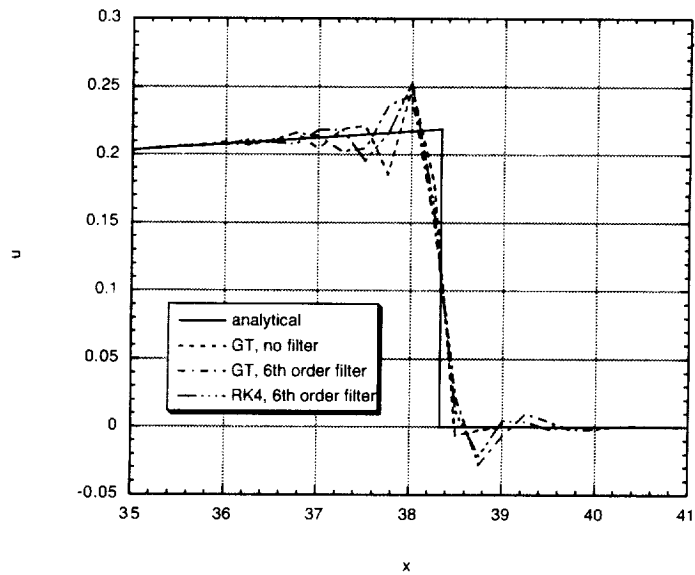

(b) Detail of shock

Figure 4.11: Solution to nonlinear convection problem with shock
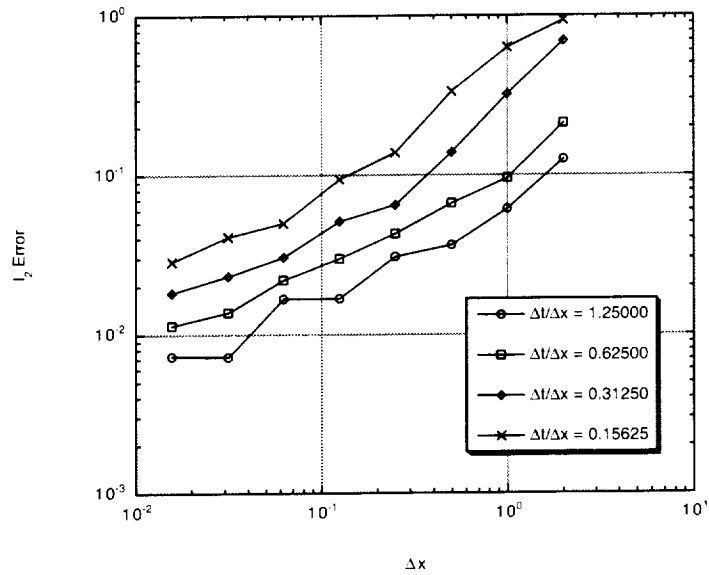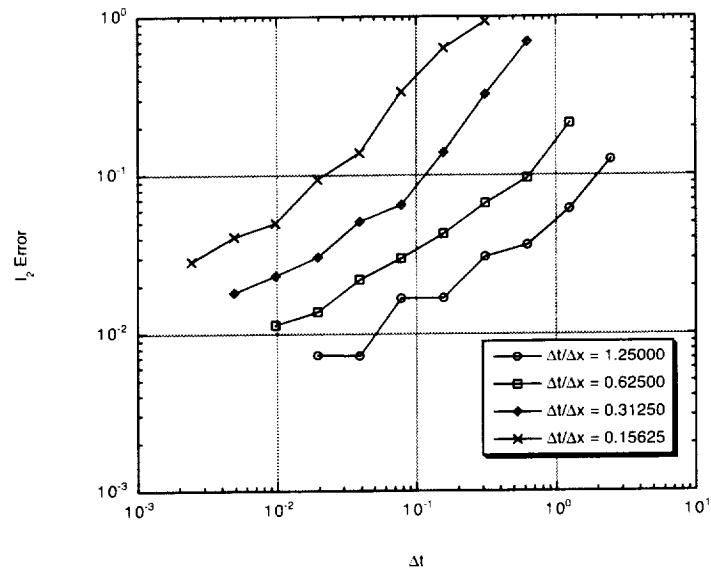
(a) Spatial error

(b) Temporal error

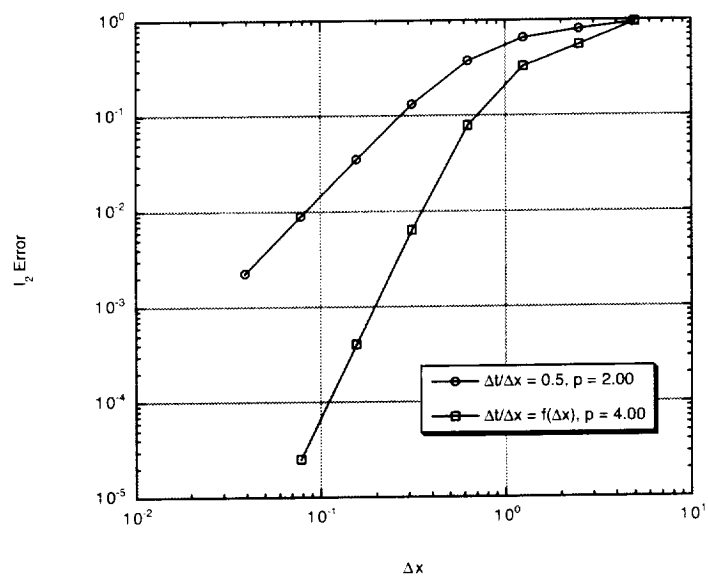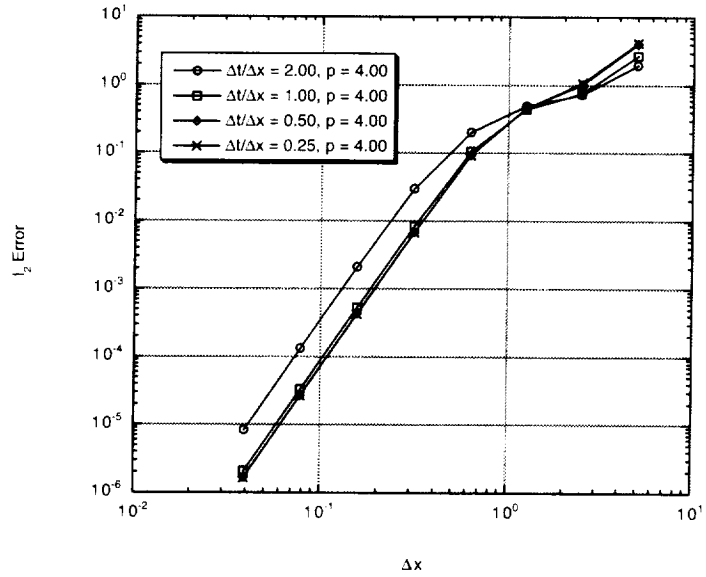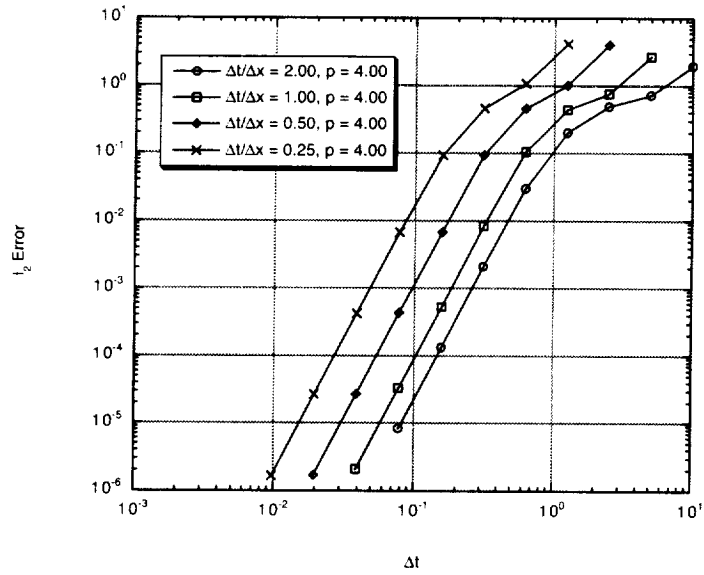Figure 4.12: Error of Gottlieb-Turkel scheme for the nonlinear problem with shock
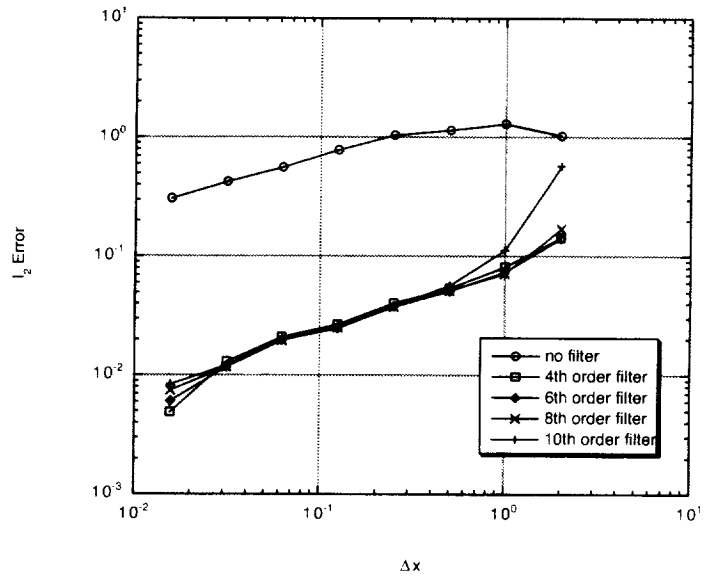
(a) Spatial error
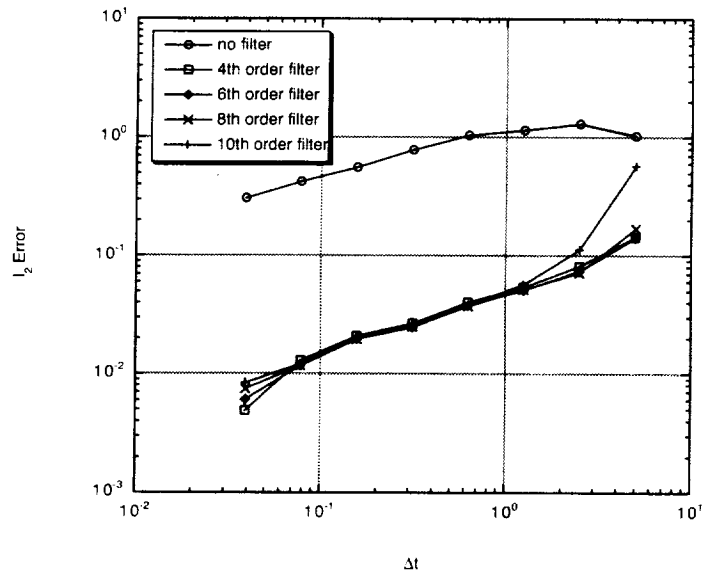
(b) Temporal error

Figure 4.13: Error of Runge-Kutta scheme for the nonlinear problem with shock

CHAPTER 5

LARGE-EDDY SIMULATION

In this chapter the equations for Large-Eddy Simulation are presented. The modeling of the unresolved (sub-grid) terms and implementation into the flow solver is discussed.

The basis of LES is the separation of the large and small scale turbulent fluctuations. To separate the large (resolved) and small (unresolved) scales the equations are filtered. A spatial filter G with a filter width Δ is used.

$$\bar{f} = \int_{-\infty}^{\infty} G(x - \xi) f(\xi) d\xi \tag{5.1}$$

The overbar represents the resolved, filtered, or large-scale portion of the function. Commonly used filter functions are a box filter, a Gaussian filter, or a spectral cutoff filter [30]. Typically, it is not necessary to know the exact form of the filter function G, but only that it exists. In practice, the solution is not explicitly filtered. It is assumed that the numerically computed solution is a filtered representation of the exact solution. This assumption is justified based on the Fourier analysis results of sections 3.3 and 3.4. There, the numerical schemes and solution filtering were shown to behave as a spectral cutoff filter of the exact solution.

Several constraints are imposed on the filter function.

1) $\quad G(-\xi) = G(\xi)$

2) $\quad \displaystyle\int_{-\infty}^{\infty} G(\xi)d\xi = 1$

3) $\quad G(\xi) \to 0 \quad \text{as} \quad |\xi| \to \infty$

4) $\quad G(\xi) \quad \text{is small outside} \quad \left(-\frac{\Delta}{2}, \frac{\Delta}{2}\right)$

These constraints are necessary to insure that the filter function will commute with the derivative.

$$\overline{\frac{\partial f}{\partial x}} = \frac{\partial \overline{f}}{\partial x} \tag{5.2}$$

Favre (density) weighting is used in the filtering process. This allows for convenient recovery of terms corresponding to the unfiltered equations.

$$\tilde{f} = \frac{\overline{\rho f}}{\overline{\rho}} \tag{5.3}$$

5.1 Filtered Equations

The filtering process is applied to the continuity, momentum, and energy equations. Details of this process can be found in Appendix A. The resulting equations are comprised of resolved and unresolved terms. The resolved terms in the filtered equations directly correspond, in form, to the unfiltered equations. The additional unresolved or sub-grid terms are modeled as source terms to the equations.

5.1.1 Continuity Equation

The filtered continuity equation contains only resolved terms. Thus, it corresponds directly to the unfiltered equation (2.1).

$$\frac{\partial \rho}{\partial t} + \frac{\partial \bar{\rho}\tilde{u}_i}{\partial x_i} = 0 \qquad (5.4)$$

5.1.2 Momentum Equation

The momentum equation contains two unresolved terms (underbraced) that must be modeled.

$$\frac{\partial \bar{\rho}\tilde{u}_i}{\partial t} + \frac{\partial \bar{\rho}\tilde{u}_i\tilde{u}_j}{\partial x_j} + \frac{\partial \bar{p}}{\partial x_i} = \frac{\partial \hat{\sigma}_{ij}}{\partial x_j} - \underbrace{\frac{\partial \tau_{ij}}{\partial x_j}}_{i} + \underbrace{\frac{\partial}{\partial x_j}\left(\bar{\sigma}_{ij} - \hat{\sigma}_{ij}\right)}_{ii} \qquad (5.5)$$

Three stress tensors occur in (5.5). The filtered stress tensor

$$\bar{\sigma}_{ij} = -\overline{\tfrac{2}{3}\mu\delta_{ij}S_{kk}} + \overline{2\mu S_{ij}} \qquad (5.6)$$

The resolved stress tensor

$$\hat{\sigma}_{ij} = -\tfrac{2}{3}\tilde{\mu}\delta_{ij}\widetilde{S}_{kk} + 2\tilde{\mu}\widetilde{S}_{ij} \qquad (5.7)$$

where $\tilde{\mu} = \mu(\widetilde{T})$, and

$$\widetilde{S}_{ij} = \frac{1}{2}\left(\frac{\partial \tilde{u}_j}{\partial x_i} + \frac{\partial \tilde{u}_i}{\partial x_j}\right) \qquad (5.8)$$

The third is the unresolved or sub-grid scale stress tensor, τ_{ij}. It is this term that provides the effect of the sub-grid scale turbulence on the larger resolved scales.

5.1.3 Energy Equation

The Favre filtered energy equation contains five additional unresolved terms (underbraced) that must be modeled.

$$\frac{\partial \bar{\rho}\tilde{e}_t}{\partial t} + \frac{\partial \bar{\rho}\tilde{u}_i\tilde{e}_t}{\partial x_i} + \frac{\partial \tilde{u}_i\bar{p}}{\partial x_i} = \frac{\partial \tilde{u}_j\hat{\sigma}_{ij}}{\partial x_i} - \frac{\partial \hat{q}_i}{\partial x_i} - \underbrace{\frac{\partial}{\partial x_i}\left(\frac{\gamma R}{\gamma-1}Q_i\right)}_{i} + \underbrace{\epsilon}_{ii} - \underbrace{\frac{\partial \bar{\rho}D_i}{\partial x_i}}_{iii}$$

$$+ \underbrace{\frac{\partial}{\partial x_i}\left(\overline{u_j\frac{\partial \sigma_{ij}}{\partial x_i}} - \tilde{u}_j\frac{\partial \hat{\sigma}_{ij}}{\partial x_i}\right)}_{iv} - \underbrace{\frac{\partial}{\partial x_i}(\bar{q}_i - \hat{q}_i)}_{v} \quad (5.9)$$

where the filtered total energy is

$$\tilde{e}_t = \tilde{e} + \tfrac{1}{2}\widetilde{u_k u_k} \quad (5.10)$$

and the filtered and resolved heat flux vectors are

$$\bar{q}_i = -\overline{k\frac{\partial T}{\partial x_i}} \quad (5.11a)$$

$$\hat{q}_i = -\tilde{k}\frac{\partial \tilde{T}}{\partial x_i} \quad (5.11b)$$

where $\tilde{k} = k(\tilde{T})$. The sub-grid scale heat flux is given by

$$Q_i = \bar{\rho}\left(\widetilde{u_i T} - \tilde{u}_i\tilde{T}\right) \quad (5.12)$$

The sub-grid scale turbulent dissipation rate is

$$\epsilon = \overline{\sigma_{ij}\frac{\partial u_j}{\partial x_i}} - \hat{\sigma}_{ij}\frac{\partial \tilde{u}_j}{\partial x_i} \quad (5.13)$$

and the sub-grid scale turbulent diffusion is

$$\bar{\rho}D_i = \tfrac{1}{2}\left(\widetilde{u_i u_k u_k} - \tilde{u}_i\widetilde{u_k u_k}\right) \quad (5.14)$$

The equation of state becomes

$$\bar{p} = \bar{\rho} R \widetilde{T} \tag{5.15}$$

Since the total energy, equation (5.10), contains the unknown $\widetilde{u_k u_k}$, pressure must be obtained using the following expression

$$\bar{p} = (\gamma - 1) \left(\bar{\rho} \tilde{e}_t - \tfrac{1}{2} \bar{\rho} \tilde{u}_k \tilde{u}_k - \tfrac{1}{2} \tau_{kk} \right) \tag{5.16}$$

5.2 Sub-Grid Scale Modeling

The unresolved or sub-grid scale contributions to equations (5.9) and (5.5) must be modeled. The methodology used here is based on the incompressible sub-grid scale model of Smagorinsky [24]. Additional terms to account for compressibility were added based on the work of Moin et. al. [28] and Vreman et. al. [52].

5.2.1 Momentum Equation

The Smagorinsky model is a very popular and widely used model for the sub-grid scale stress tensor. It is an eddy viscosity model where the sub-grid scale stress tensor is modeled as an eddy viscosity multiplying the resolved stress tensor. It was developed for incompressible flows and has been frequently extended to compressible flows. The compressible form of the model, given by Moin et. al., was used here.

$$\tau_{ij} = \tfrac{2}{3} C_I \bar{\rho} \Delta^2 |\widetilde{S}|^2 \delta_{ij} - 2 C \bar{\rho} \Delta^2 |\widetilde{S}| \left(\widetilde{S}_{ij} - \tfrac{1}{3} \widetilde{S}_{kk} \delta_{ij} \right) \tag{5.17}$$

The coefficients C and C_I are user defined constants. The second unresolved term in the equation results from the nonlinearity of the viscous stresses and is neglected.

The final form of the modeled momentum equation is

$$\frac{\partial \bar{\rho} \tilde{u}_i}{\partial t} + \frac{\partial \bar{\rho} \tilde{u}_i \tilde{u}_j}{\partial x_j} + \frac{\partial \bar{p}}{\partial x_i} = \frac{\partial}{\partial x_j} \left[(\tilde{\mu} + \mu_t) \frac{\hat{\sigma}_{ij}}{\tilde{\mu}} - \Phi \delta_{ij} \right] \tag{5.18}$$

The eddy viscosity is

$$\mu_t = C\bar{\rho}\Delta^2|\widetilde{S}|$$ (5.19)

and Φ is

$$\Phi = \tfrac{2}{3}C_I\rho\Delta^2|\widetilde{S}|^2$$ (5.20)

5.2.2 Energy Equation

There are many different sub-grid models for the energy equation and no one set of models is as popular as the Smagorinsky model for the momentum equation. This is because there are many forms of the energy equation that result in different sub-grid scale terms. It is also because the majority of work in LES has been done for incompressible flows. The filtered energy equation (5.9) contains five unresolved terms.

The first term. the sub-grid scale heat flux is modeled based on Moin's work [28]

$$Q_i = \frac{\mu_t}{Pr_t}\frac{\partial \widetilde{T}}{\partial x_i}$$ (5.21)

The model for the second term comes from Vreman [52] and is given by

$$\epsilon = \frac{C_3}{2\Delta}\tau_{kk}$$ (5.22)

The coefficient C_3 is a user defined constant. The last three terms are typically considered to be much smaller than the other terms and are neglected.

The final form of the modeled energy equation is

$$\frac{\partial \bar{\rho}\widetilde{e}_t}{\partial t} + \frac{\partial \bar{\rho}\widetilde{u}_i\widetilde{e}_t}{\partial x_i} + \frac{\partial \widetilde{u}_i\bar{p}}{\partial x_i} = \frac{\partial}{\partial x_i}\left[\widetilde{u}_i\hat{\sigma}_{ij} + \left(\widetilde{\mu} + \mu_t\frac{Pr}{Pr_t}\right)\frac{\gamma R}{\gamma - 1}\frac{1}{Pr}\frac{\partial \widetilde{T}}{\partial x_i}\right] + \epsilon \quad (5.23)$$

5.3 Implementation

The sub-grid scale terms in equations (5.18) and (5.23) and their corresponding models were implemented in both the two-dimensional/axisymmetric and three-dimensional Navier-Stokes flow solvers. It is important to note that the modified definition of the pressure (equation (5.16)) must be used.

Because the resolution of scales in a numerical scheme is directly related to the grid resolution, the filter width Δ was chosen to be a characteristic length of the computational grid. Since the grid is not uniform, this length varies widely over the grid. The filter width at each location was defined as the cubed root of the volume associated with each grid point.

To maintain a laminar sub-layer in wall bounded regions, the effect of the sub-grid model must be diminished near the wall. To accomplish this, a Van Driest damping function [53] was used to scale the effect of the sub-grid terms.

$$f_{VD} = \left(1 - e^{-\left(\frac{y^+}{A^+} \right)} \right) \tag{5.24}$$

where y^+ is the inner variable distance and the constant A^+ is set to 26.

The constants for the sub-grid models were chosen based on previous studies. Erlebacher et. al. [54], Moin [28], and Vreman [52] derived the model constants based on DNS results. Erlebacher concluded that, $C = 0.012$, and Moin gave a range of values of, $0.008 \leq C \leq 0.014$. Moin also provide a range of values for C_I, where $0.0025 \leq C_I \leq 0.009$. From these data the coefficients were chosen to be $C = 0.012$, and $C_I = 0.00575$. Vreman determined that $C_3 = 0.6$.

Results from LES simulations are obtained in terms of filtered conservation variables. These variables differ from the exact conservation variables by equation (5.1).

However, since the form of the filter function, G, is unknown, we cannot recover the exact conservation variables. We must assume that the difference between the two forms is small. For convenience, when reporting LES simulation results the overbar ( ) and tilde (~) are dropped in the notation and must be assumed.

CHAPTER 6

FLOW SOLVER

The numerical methods outlined in Chapter 3 are implemented in two computer codes to solve the unsteady Navier-Stokes equations. Separate three-dimensional and two-dimensional/axisymmetric codes were created. The codes were written in the FORTRAN 77 computer language and should run on any computer platform with a FORTRAN compiler.

While the purpose of the codes is to simulate compressible turbulent jets, they were written so that they can be easily adapted to a wide range of flows and geometries.

Large-Eddy simulations can be performed by solving the filtered unsteady Navier-Stokes equations with the sub-grid scale model, or direct solution of the equations without approximation can be made. By neglecting the viscous terms in the Navier-Stokes equations the Euler equations can also be solved.

6.1   Generalized Curvilinear Coordinates

To allow easy solution to a wide range of geometries the Navier-Stokes equations are solved using generalized curvilinear coordinates [55]. This enables the computational grids to be fitted to complex shapes and allows for grid stretching.

6.1.1 Coordinate Transformation

Easy and efficient implementation of the numerical scheme is done by working in a computational domain. This domain is rectangular and consists of equally spaced grid points. The computational domain (ξ, η, ζ) is mapped onto the physical domain (x, y, z) using the following transformation

$$\xi = \xi(x, y, z)$$

$$\eta = \eta(x, y, z)$$

$$\zeta = \zeta(x, y, z) \tag{6.1}$$

Derivatives in cartesian coordinates are computed using the chain rule

$$\frac{\partial}{\partial x} = \xi_x \frac{\partial}{\partial \xi} + \eta_x \frac{\partial}{\partial \eta} + \zeta_x \frac{\partial}{\partial \zeta}$$

$$\frac{\partial}{\partial y} = \xi_y \frac{\partial}{\partial \xi} + \eta_y \frac{\partial}{\partial \eta} + \zeta_y \frac{\partial}{\partial \zeta}$$

$$\frac{\partial}{\partial z} = \xi_z \frac{\partial}{\partial \xi} + \eta_z \frac{\partial}{\partial \eta} + \zeta_z \frac{\partial}{\partial \zeta} \tag{6.2}$$

The terms ξ_x, ξ_y, ξ_z, η_x, η_y, η_z, ζ_x, ζ_y, and ζ_z are the grid metrics associated with the transformation. The grid metrics are computed numerically using the following

method.

$$\xi_x = J(y_\eta z_\zeta - y_\zeta z_\eta)$$

$$\xi_y = J(x_\zeta z_\eta - x_\eta z_\zeta)$$

$$\xi_z = J(x_\eta y_\zeta - x_\zeta y_\eta)$$

$$\eta_x = J(y_\zeta z_\xi - y_\xi z_\zeta)$$

$$\eta_y = J(x_\xi z_\zeta - x_\zeta z_\xi)$$

$$\eta_z = J(x_\zeta y_\xi - x_\xi y_\zeta)$$

$$\zeta_x = J(y_\xi z_\eta - y_\eta z_\xi)$$

$$\zeta_y = J(x_\eta z_\xi - x_\xi z_\eta)$$

$$\zeta_z = J(x_\xi y_\eta - x_\eta y_\xi) \tag{6.3}$$

The Jacobian of the transformation. J. is defined as

$$J = \frac{1}{x_\xi(y_\eta z_\zeta - y_\zeta z_\eta) - x_\eta(y_\xi z_\zeta - y_\zeta z_\xi) + x_\zeta(y_\xi z_\eta - y_\eta z_\xi)} \tag{6.4}$$

The terms x_ξ, x_η, x_ζ, y_ξ, y_η, y_ζ, z_ξ, z_η. and z_ζ are computed using fourth-order central differences in the interior of the grid and one sided differences on the boundaries. The calculation is easily done in computational space because the grid is evenly spaced in the ξ, η. and ζ directions.

6.1.2   Chain Rule Form of the Governing Equations

The chain rule form of the governing equations is

$$\frac{\partial Q}{\partial t} + \xi_x \frac{\partial}{\partial \xi}(E - E_v) + \eta_x \frac{\partial}{\partial \eta}(E - E_v) + \zeta_x \frac{\partial}{\partial \zeta}(E - E_v)$$
$$+ \xi_y \frac{\partial}{\partial \xi}(F - F_v) + \eta_y \frac{\partial}{\partial \eta}(F - F_v) + \zeta_y \frac{\partial}{\partial \zeta}(F - F_v) \tag{6.5}$$
$$+ \xi_z \frac{\partial}{\partial \xi}(G - G_v) + \eta_z \frac{\partial}{\partial \eta}(G - G_v) + \zeta_z \frac{\partial}{\partial \zeta}(G - G_v) = 0$$

This form of the equations is a weak conservation form. Most CFD solvers use a strong conservation law form of the equations developed by Vinokur [56]. However, Hixon et. al. [57] recently showed that in practice, the chain rule form of the equations is more accurate than the strong conservation form when the metric terms are computed numerically.

6.2 Time Stepping

The time step used to advance the solution is based on the relation

$$\Delta t = CFL \left(\frac{\Delta x}{A} \right) \tag{6.6}$$

where A is the local wave propagation speed and CFL is the Courant Friedrichs Lewey number [8], a constant which is based on stability considerations. The term $\frac{\Delta x}{A}$ is a characteristic time and is computed using the inviscid CFL condition [58].

$$\Delta t_{CFL} = \frac{\Delta x}{A} = \left(\frac{|u|}{\Delta x} + \frac{|v|}{\Delta y} + \frac{|w|}{\Delta z} + a\sqrt{\frac{1}{\Delta x^2} + \frac{1}{\Delta y^2} + \frac{1}{\Delta z^2}} \right)^{-1} \tag{6.7}$$

For time accuracy all points in the domain must be advanced at the same time step. Therefore, Δt_{CFL} is computed at every grid point and the minimum value is used to compute the time step.

$$\Delta t = CFL \cdot \Delta t_{CFL_{min}} \tag{6.8}$$

6.3 Treatment of the Viscous Terms

The computation of the derivatives within the viscous fluxes (equations (2.4), (2.8), (2.13), & (2.15a)) is done differently for both numerical methods. The predictor-corrector schemes require a fairly complex treatment of the viscous terms. Bayliss et.

al. [36] proposed the following method to maintain the order of accuracy of the Mac-Cormack type schemes. If the derivative within the viscous flux is being differenced in the same direction as the flux is differenced, then the derivative in the viscous flux is computed using a one-sided difference in the direction opposite of direction the flux is being differenced. If the derivative within the viscous flux is being differenced in a direction other than the direction the flux is differenced, then the derivative in the viscous flux is computed using a central difference. Consequently, the derivatives in the viscous terms are computed twice (one-sided and central differenced) for each step. The Runge-Kutta based schemes simply use fourth-order central differences for all viscous derivatives.

6.4 Boundary Conditions

Boundary conditions can be specified on any portion of any grid surface within the computational grid. This allows for a large range of complex shapes to be modeled within a single computational domain. Internal portions of the grid that are enclosed by computational boundaries are specified as "holes". The conservation variables within the hole regions are not updated during the solution process. Figure 6.1 illustrates the use of internal boundaries and holes to model a nozzle wall.

6.4.1 Inflow and Outflow Boundaries

The formulation of these boundary conditions is based on the local one-dimensional propagation properties of the flow [46]. These properties are obtained from the eigenvalues of the Jacobian matrix in the quasi-linear one-dimensional Euler equations.

The flow is assumed to be one-dimensional in the direction normal to the boundary. The resulting characteristic variables are $u_i n_i$, $u_i n_i + a$, and $u_i n_i - a$, where n_i is the unit normal vector to the boundary and a is the speed of sound. The variable $u_i n_i$ occurs twice in two-dimensional flows and three times in three dimensional flows. These eigenvalues determine the propagation direction of the characteristic variables at the boundary.

Subsonic Inflow

For a subsonic inflow boundary $u_i < a$. This results in four (three in two-dimensions) positive characteristic variables and one negative variable. Therefore four variables propagate from the boundary into the domain and one variable propagates out of the boundary from the domain. To correctly mimic this behavior in the computation, so that the problem is mathematically well posed, four of the five conservation variables are specified at the boundary and one is determined from the interior.

The flow from the inflow boundary is assumed to be normal to the boundary so that the transverse velocity components are set to zero. The total pressure, p_0, and total temperature, T_0 are specified. The velocity normal to the boundary is extrapolated from the interior. For a constant ξ surface (constant i) with its normal

vector aligned in the x direction. the conservation variables are are obtained as follows.

$$Q_{1_{(i,j,k)}} = \frac{p_0}{RT_0}\left(1 + \frac{u^2_{(i+1,j,k)}}{\frac{2\gamma RT_0}{\gamma-1} - u^2_{(i+1,j,k)}}\right)^{-\frac{1}{\gamma-1}}$$

$$Q_{2_{(i,j,k)}} = Q_{1_{(i,j,k)}} u_{(i+1,j,k)}$$

$$Q_{3_{(i,j,k)}} = 0$$

$$Q_{4_{(i,j,k)}} = 0$$

$$Q_{5_{(i,j,k)}} = Q_{1_{(i,j,k)}}\left[\frac{RT_0}{\gamma-1} + \left(\frac{\gamma-1}{\gamma}\right)\frac{u^2_{(i+1,j,k)}}{2}\right] \tag{6.9}$$

Supersonic Inflow

For a supersonic inflow boundary $u_i > a$. This results in five (four in two-dimensions) positive eigenvalues. Therefore all information propagates along the characteristics from the boundary to the interior.

All five conservation variables are specified on the inflow boundary and are held fixed. For a constant ξ boundary the conservation variables are

$$Q_{1_{(i,j,k)}} = \rho_\infty$$

$$Q_{2_{(i,j,k)}} = \rho_\infty u_\infty$$

$$Q_{3_{(i,j,k)}} = \rho_\infty v_\infty$$

$$Q_{4_{(i,j,k)}} = \rho_\infty w_\infty$$

$$Q_{5_{(i,j,k)}} = \rho_\infty e_{t_\infty} \tag{6.10}$$

Subsonic Outflow

For a subsonic outflow boundary $u_i < a$. This results in four (three in two-dimensions) negative eigenvalues and one positive one. Here information from four

of the characteristics propagates from the interior to the boundary and information from one characteristic propagates from the boundary to the interior.

The static pressure, p_e, is specified on the outflow boundary. Density and all three velocity components are extrapolated from the interior. Total energy is computed using the specified static pressure and the extrapolated density and velocities.

$$Q_{1_{(imax,j,k)}} = Q_{1_{(imax-1,j,k)}}$$

$$Q_{2_{(imax,j,k)}} = Q_{2_{(imax-1,j,k)}}$$

$$Q_{3_{(imax,j,k)}} = Q_{3_{(imax-1,j,k)}}$$

$$Q_{4_{(imax,j,k)}} = Q_{4_{(imax-1,j,k)}}$$

$$Q_{5_{(imax,j,k)}} = \frac{p_e}{\gamma - 1} + \frac{Q_{2_{(imax,j,k)}}^2 + Q_{3_{(imax,j,k)}}^2 + Q_{4_{(imax,j,k)}}^2}{2Q_{1_{(imax,j,k)}}} \tag{6.11}$$

Supersonic Outflow

For a supersonic outflow boundary $u_i > a$. This results in all five (four in two-dimensions) eigenvalues being negative. Information from all characteristics propagates from the interior out through the boundary.

All five conservation variables are extrapolated from the interior onto the boundary.

$$Q_{1_{(imax,j,k)}} = Q_{1_{(imax-1,j,k)}}$$

$$Q_{2_{(imax,j,k)}} = Q_{2_{(imax-1,j,k)}}$$

$$Q_{3_{(imax,j,k)}} = Q_{3_{(imax-1,j,k)}}$$

$$Q_{4_{(imax,j,k)}} = Q_{4_{(imax-1,j,k)}}$$

$$Q_{5_{(imax,j,k)}} = Q_{5_{(imax-1,j,k)}} \tag{6.12}$$

Non-Reflecting Exit Zone

Waves that propagate from the interior of the domain to the outflow boundaries can reflect off the boundary and back into the computational domain. These reflected waves are non-physical and may contaminate or distort the solution. These reflections occur because the extrapolation of interior information to the boundary is done along grid lines and not in the direction of the propagating waves.

Expanding the computational domain so that the boundaries are far away from the area of interest reduce this problem, but adds significantly to the computational cost. Several authors have attempted to eliminate these reflections through the use of characteristic boundaries [59–61]. However, these efforts have met with limited success for two- and three-dimensional applications.

A relatively simple and more effective method to reduce reflections is the use of "exit zones" [18,61,62]. In this method a simple outflow boundary condition, such as those outlined above are used. In the region adjacent to the outflow boundary, a combination of grid stretching and solution filtering is used to damp the outgoing and reflected waves. Rapid grid stretching increases Δx and therefore increases the associated dissipation in the truncation error of the numerical scheme (equations (3.5), (3.8) and (3.10)). Solution filtering (section 3.4) provides additional dissipation that damps a large range of wavelengths.

6.4.2 Solid Surfaces

Two options exist to model solid surfaces. Surfaces in viscous calculations are specified with a no-slip wall boundary condition. Surfaces in inviscid calculations and planes of symmetry are specified using a slip wall boundary condition.

No-Slip Wall

The no-slip wall boundary imposes no relative motion between the fluid and the solid surface. Enforcing no-slip at the wall is done by setting all velocity components on the boundary to zero. The density and total energy are determined using two additional constraints. The first constraint stems from boundary layer theory. The pressure gradient normal to the wall is set to zero. The second constraint assumes no heat transfer through the wall, and consequently the temperature gradient normal to the wall is set to zero. For an η constant wall (constant j), the conservation variables are written as

$$Q_{1_{(i,j,k)}} = Q_{1_{(i,j+1,k)}}$$

$$Q_{2_{(i,j,k)}} = 0$$

$$Q_{3_{(i,j,k)}} = 0$$

$$Q_{4_{(i,j,k)}} = 0$$

$$Q_{5_{(i,j,k)}} = Q_{5_{(i,j+1,k)}} - \frac{Q_{2_{(i,j+1,k)}}^2 + Q_{3_{(i,j+1,k)}}^2 + Q_{4_{(i,j+1,k)}}^2}{2Q_{1_{(i,j+1,k)}}} \tag{6.13}$$

This formulation assumes that the grid lines are normal to the wall.

Slip Wall

An inviscid wall surface and a symmetry plane share the same constraints and hence the same boundary condition. The velocity vector of the flow along the surface must be tangent to the surface. To accomplish this, the velocity vector one point off the wall is decomposed into components that are normal and tangential to the surface. The normal component is then removed from the velocity vector and this vector is imposed on the boundary. The loss in kinetic energy due to the normal

velocity is compensated for by correcting the total energy on the boundary based on conservation of total enthalpy. The density gradient at the wall is assumed to be constant. For an η constant wall (constant j), the conservation variables are written as

$$Q1_{(i,j,k)} = Q1_{(i,j+1,k)}$$

$$Q2_{(i,j,k)} = Q2_{(i,j+1,k)} - Q1_{(i,j+1,k)} U_n \frac{\eta_x}{\sqrt{\eta_x^2 + \eta_y^2 + \eta_z^2}}$$

$$Q3_{(i,j,k)} = Q3_{(i,j+1,k)} - Q1_{(i,j+1,k)} U_n \frac{\eta_y}{\sqrt{\eta_x^2 + \eta_y^2 + \eta_z^2}}$$

$$Q4_{(i,j,k)} = Q4_{(i,j+1,k)} - Q1_{(i,j+1,k)} U_n \frac{\eta_z}{\sqrt{\eta_x^2 + \eta_y^2 + \eta_z^2}}$$

$$Q5_{(i,j,k)} = Q5_{(i,j+1,k)} - \frac{1}{2}\left(\frac{\gamma - 1}{\gamma}\right) Q1_{(i,j+1,k)} U_n^2 \tag{6.14}$$

where the magnitude of the normal velocity, U_n, is

$$U_n = u_{(i,j+1,k)} \frac{\eta_x}{\sqrt{\eta_x^2 + \eta_y^2 + \eta_z^2}} + v_{(i,j+1,k)} \frac{\eta_y}{\sqrt{\eta_x^2 + \eta_y^2 + \eta_z^2}} + w_{(i,j+1,k)} \frac{\eta_z}{\sqrt{\eta_x^2 + \eta_y^2 + \eta_z^2}} \tag{6.15}$$

The metric terms η_x, η_y, and η_z are evaluated on the boundary.

6.4.3 Other

The following boundary conditions result from computational necessity, not physical modeling.

Changes for Fourth-Order Schemes

The fourth-order schemes call for special treatment one grid point away from the boundaries. Both fourth-order numerical schemes require two points on either side of a grid point to compute the derivative at that point. One point from a boundary, the scheme must be modified using a skewed difference stencil to prevent over-running

the bounds of the storage arrays and to maintain fourth-order accuracy. The "skewed forward" and "skewed backward" fourth-order difference stencils are

$$\frac{\partial f}{\partial x}\bigg|_{fwd} = \frac{f_{i+3} - 6f_{i+2} + 18f_{i+1} - 10f_i - 3f_{i-1}}{12(\Delta x)} \tag{6.16a}$$

$$\frac{\partial f}{\partial x}\bigg|_{bwd} = \frac{3f_{i+1} + 10f_i - 18f_{i-1} + 10f_{i-2} - f_{i-3}}{12(\Delta x)} \tag{6.16b}$$

Pole Boundary

The collapsing of a grid surface to a line or "pole" is often done to model cylindrical objects in generalized curvilinear coordinates. Figure 6.2 illustrates how a volume in computational space is transformed to a sector of a right circular cylinder. Values for the variables on the collapsed surface (j_{min} in figure 6.2) are obtained by averaging the values over the collapsed index, one point off of the collapsed surface. For example, on a constant η surface where ζ lines are collapsed to a point, the values of the variables at each ξ point on the η surface are obtained by taking the mass average of the variables over all ζ at $\eta + 1$. This boundary condition is used for the axis in a three-dimensional cylindrical calculation. The average flowfield values are determined

by

$$\rho_{avg} = \sum_{k=1}^{k_{max}} \frac{\rho_k}{J_k} \left(\sum_{k=1}^{k_{max}} \frac{1}{J_k} \right)^{-1}$$

$$u_{avg} = \sum_{k=1}^{k_{max}} \frac{\rho_k u_k}{J_k} \left(\sum_{k=1}^{k_{max}} \frac{\rho_k}{J_k} \right)^{-1}$$

$$v_{avg} = \sum_{k=1}^{k_{max}} \frac{\rho_k v_k}{J_k} \left(\sum_{k=1}^{k_{max}} \frac{\rho_k}{J_k} \right)^{-1}$$

$$w_{avg} = \sum_{k=1}^{k_{max}} \frac{\rho_k w_k}{J_k} \left(\sum_{k=1}^{k_{max}} \frac{\rho_k}{J_k} \right)^{-1}$$

$$p_{avg} = \sum_{k=1}^{k_{max}} \frac{\rho_k p_k}{J_k} \left(\sum_{k=1}^{k_{max}} \frac{\rho_k}{J_k} \right)^{-1}$$

(6.17)

The conservation variables on the boundary are then

$$Q_{1_{(i,j,k)}} = \rho_{avg}$$

$$Q_{2_{(i,j,k)}} = \rho_{avg} u_{avg}$$

$$Q_{3_{(i,j,k)}} = \rho_{avg} v_{avg}$$

$$Q_{4_{(i,j,k)}} = \rho_{avg} w_{avg}$$

$$Q_{5_{(i,j,k)}} = \frac{p_{avg}}{\gamma - 1} + \frac{1}{2} \rho_{avg} \left(u_{avg}^2 + v_{avg}^2 + w_{avg}^2 \right) \qquad (6.18)$$

Axis of Symmetry

A boundary condition is needed for axisymmetric analyses on the bounding grid line where $r = 0$, the axis of symmetry. Since the flow is symmetric about this axis no flow may cross the grid line. Therefore, the velocity vector must be tangent to the boundary. This restriction is the same as the restriction for the slip wall boundary and hence, the same method is used to impose the constraints (equation (6.14)).

Overlap

The grid topology commonly referred to as an "O"-grid is frequently used to model round objects and domains, such as cylinders, airfoils and pipes. The domain is formed by wrapping the grid around upon itself so that the minimum and maximum boundaries of a common index are coincident (figure 6.3). The coincident computational boundaries are in the interior of the physical domain and must be treated as if they were also on the interior of the computational domain so that they do not create a non-physical barrier on the interior of the domain. In other words, the governing equations should be solved on these boundaries as if they are in the interior of the computational domain and information must be readily passed across the boundaries. This is done by overlapping the grid so that at every point where a skewed difference is performed the result can be replaced with a central differenced value from a coincident point in the overlapped region. Table 6.1 lists the skewed differenced grid points and the coincident central differenced points necessary for the overlap boundary condition.

boundary point (skewed difference)	interior point (central difference)
1	$k_{max} - 4$
2	$k_{max} - 3$
$k_{max} - 1$	3
k_{max}	4

Table 6.1: Coincident grid points in overlap region

6.5 Computer Resource Requirements

The memory and CPU time required are reported for both the 2D and 3D codes. The resource requirements reported are for Silicon Graphics workstations, which were used for all the large scale calculations in this document.

Memory requirements for the two-dimensional/axisymmetric and three-dimensional codes are reported in table 6.2. Both single and double precision requirements are given.

code	bytes/grid pt. single precision	double precision
2D/Axi.	244	472
3D	360	700

Table 6.2: Memory required

Table 6.3 contains CPU times for all possible combinations of code (2D, axisymmetric, or 3D), equations (Euler, Navier-Stokes, or LES) and numerical scheme. The execution times are presented as time per iteration per grid point in seconds. The CPU times were obtained using a Silicon Graphics Power Indigo^2 workstation with a MIPS R8000 processor running at 75MHz. The code was compiled using double precision data and the compiler options were chosen for maximum performance.

6.6 Parallel Implementation

Parallel processing is an efficient and inexpensive method to speed the execution of computer programs [63–65]. UNIX workstations with multiple central processing

code	equations	scheme	time/iter./grid pt. (sec)
2D	Euler	Gottlieb-Turkel	$9.092 \cdot 10^{-6}$
	Euler	Runge-Kutta	$1.654 \cdot 10^{-5}$
	Navier-Stokes	Gottlieb-Turkel	$1.218 \cdot 10^{-5}$
	Navier-Stokes	Runge-Kutta	$2.122 \cdot 10^{-5}$
	LES	Gottlieb-Turkel	$1.655 \cdot 10^{-5}$
	LES	Runge-Kutta	$3.196 \cdot 10^{-5}$
Axi.	Euler	Gottlieb-Turkel	$9.415 \cdot 10^{-6}$
	Euler	Runge-Kutta	$1.732 \cdot 10^{-5}$
	Navier-Stokes	Gottlieb-Turkel	$1.498 \cdot 10^{-5}$
	Navier-Stokes	Runge-Kutta	$2.808 \cdot 10^{-5}$
	LES	Gottlieb-Turkel	$1.982 \cdot 10^{-5}$
	LES	Runge-Kutta	$3.945 \cdot 10^{-5}$
3D	Euler	Gottlieb-Turkel	$6.898 \cdot 10^{-5}$
	Euler	Runge-Kutta	$1.069 \cdot 10^{-4}$
	Navier-Stokes	Gottlieb-Turkel	$1.182 \cdot 10^{-4}$
	Navier-Stokes	Runge-Kutta	$1.555 \cdot 10^{-4}$
	LES	Gottlieb-Turkel	$1.394 \cdot 10^{-4}$
	LES	Runge-Kutta	$2.074 \cdot 10^{-4}$

Table 6.3: CPU time required

units (CPU's) are widely available and cost a fraction of the price of super-computers. Codes written to take advantage of the parallel architecture of these machines can execute as fast or faster than on a comparable super-computer. Parallel processing achieves this performance increase by dividing the work normally done by a single central processing unit amongst several CPU's.

There are two primary methods used for the parallel processing of CFD solvers. The first is distributed memory processing. In this method each CPU uses a separate bank of memory for its calculations. Communication of data between CPU's is done explicitly through user implemented interfaces. Often the CPU's do not reside in the

same computer, but operate as separate workstations connected through a network. A typical distributed memory CFD solver divides the computational domain into several sub-domains which are each solved on separate processors. The interfaces between sub-domains are treated as boundary conditions and are updated by passing updated solution values to adjacent sub-domains. This method requires limited communication between processors, and is therefore suitable for networked workstations, because data is only passed at the end of each iteration or set of iterations. It works very well for low order steady-state flow calculations. High order unsteady calculations are ill suited for this method because it would be necessary to pass large amounts of data between interfaces at every iteration to maintain both temporal and spatial accuracy.

The second method, shared memory processing, was used in this study. In this method, a set of CPU's share access to a common bank of memory. Communication between processors is implicit and no special interfaces are required. Shared memory systems consist of multiple processors housed in the same computer with a high speed high volume bus connecting the processors to the memory bank. Because the processors are closely coupled through the shared memory, the division of labor between processors can also be closely coupled. This division of labor is done at the loop level. The work performed in a FORTRAN "DO" loop is divided between CPU's with each processor working on a fraction of the total loop. For example, a "DO" loop which is indexed from 1 to 100 could be split between 2 processors with one processor operating from 1 to 50 and the second operating from 51 to 100. Implementing this method is done through the insertion of compiler directives into the code. The directives indicate which loop is to be parallelized and how the variables are shared in memory. Care must be taken to identify data dependencies so that variables whose

value depends on the current loop index are not overwritten by processors operating on another portion of the loop. Explicit CFD methods are well suited for this type of parallelization because the data dependencies are limited and easily overcome.

The performance of a parallel code is measured by its speedup and efficiency. Speedup is simply the ratio of the time required for single processor computation to the time required for a multi-processor computation.

$$S(n) = \frac{T_1}{T_n} \tag{6.19}$$

where T_n is the time required for an n processor computation. The efficiency of the job is the ratio of the speedup to the number of processors.

$$E(n) = \frac{S(n)}{n} = \frac{T_1}{nT_n} \tag{6.20}$$

Ideally a the speedup of a parallel code would vary linearly with the number of processors. Two primary factors limit the speedup: processor idle time and communication time between processors. Processor idle time is the time the code spends outside the parallelized loops. During this time only one processor is active and the potential work of the other processors is wasted. Communication time is the delay during which data is passed between processors and the shared memory. It is a property of the computer and varies greatly between machine types.

The performance of the 2D/axisymmetric code was measured on a Silicon Graphics 36 processor Power Challenge computer. The code was run on a representative jet calculation using a grid containing 38,829 grid points. A calculation consisting of 1.000 iterations using the Runge-Kutta scheme was repeated 10 times using an even number of processors from 2 to 20. Results were compared to a baseline calculation performed on one processor. This procedure was repeated four times. Speedup and

efficiency are presented in figures 6.4 and 6.5. The variation in results between each set of data is due to the architecture of the computer that was used. The data (memory) bus for this machine was insufficiently sized to transfer data for all 36 processors. The communication delay time varies with the number of jobs being run on the system and the number of processors for a given parallel job. Each set of parallel runs were made with the computer under different loads and hence the time required for the runs differed. Regardless, the data do show that a linear speedup is seen up to about 16 processors. Because the computer's performance varied with its load, the parallel efficiency cannot be definitively determined. In fact figure 6.5 shows some efficiencies exceeding one. This is most likely due to the load on the machine being reduced after the one processor job was run. Consequently, the baseline one processor run is not appropriate for computing the efficiency of the current multi-processor run.

6.7 Validation

To insure accurate implementation of the numerical schemes, the codes were validated using three simple test cases in both two and three dimensions. The code's results were compared to exact solutions to insure that they produced acceptable solutions.

The standard Runge-Kutta scheme (section 3.2.1) was unstable with or without solution filtering and did not provide a converged solution for any of the two- or three-dimensional calculations. The low dispersion Runge-Kutta scheme (section 3.2.2) did provide stable solutions for all calculations attempted. All Runge-Kutta results reported hereafter were obtained with the low dispersion scheme (equation (3.9)).

6.7.1 Laminar Flat Plate

Laminar flow over a flat plate was used to check the accuracy of a viscous solution. Skin friction along the plate and the self-similar velocity profile are compared to the exact solution of Blasius, as given by Schlicting [66]. The skin friction is computed using

$$C_f = \frac{\mu \left.\frac{\partial u}{\partial y}\right|_w}{\frac{1}{2}\rho_\infty U_\infty^2} \tag{6.21}$$

and the plate Reynolds number is

$$Re_x = \frac{\rho_\infty U_\infty x}{\mu_\infty} \tag{6.22}$$

The velocity profiles normal to the plate surface can be made self-similar by introducing a dimensionless coordinate.

$$\eta = y\sqrt{\frac{U_\infty}{\nu x}} \tag{6.23}$$

The Reynolds number based on plate length is 10,000 and the freestream Mach number is 0.2.

Two-dimensional solutions were obtained with both numerical schemes. The sixth-order filter was used for both calculations. The grid that was used is shown in figure 6.7. The grid dimensions were 157 points in the streamwise direction and 117 points normal to the plate surface. Subsonic inflow and subsonic outflow boundaries were specified on the left and right boundaries respectively. A no-slip wall was specified on the lower boundary and an extrapolation condition (the same as supersonic outflow) was specified on the upper boundary.

Skin friction results for both the Runge-Kutta and Gottlieb-Turkel scheme are shown in figure 6.8. The Runge-Kutta scheme slightly over predicts the skin friction

relative to the Blasius solution. The Gottlieb-Turkel scheme underpredicts the skin friction and is in greater error than the Runge-Kutta scheme.

The self-similar velocity profiles are shown in figure 6.9. Several streamwise stations. $Re_x = 2000$, 4000, 6000, and 8000 are plotted to verify the code reproduces the self-similarity. The Runge-Kutta results are very close to the Blasius solution. The Gottlieb-Turkel profiles show a thicker boundary layer thickness with a smaller velocity gradient at the wall. This is consistent with the skin friction data.

To validate the three-dimensional code, a 3D grid was created that consists of fifteen evenly spaced 2D grid planes. The 3D code was run using both numerical schemes and the results were compared to those of their 2D counterparts. Skin friction and velocity profiles at $Re_x = 4000$ are compared for both schemes (figures 6.10 & 6.11). The agreement between between the two- and three-dimensional codes is excellent for both schemes.

6.7.2 Supersonic Wedge

Supersonic flow over a two-dimensional wedge was used to test the ability of the code to predict inviscid flows and shock waves. A 15 degree wedge in a Mach 2 freestream flow was simulated (figure 6.12). Pressure coefficient on the wedge surface was compared to the exact solution.

$$C_p = \frac{p - p_\infty}{\frac{1}{2}\rho_\infty U_\infty^2} \tag{6.24}$$

The grid dimensions used were 121 points in the axial direction and 81 points in the vertical direction. The grid is shown in figure 6.13. Uniform supersonic flow was set at the inflow boundary. Supersonic outflow conditions (extrapolation) were set on the right and upper boundaries. A slip wall was specified on the lower boundary.

Two-dimensional results are shown in figure 6.14. Overall the results are in good agreement with the exact solution. But, the shock location is smeared over several grid points and some oscillation in the solution exist both upstream and downstream of the shock wave. A comparison of numerical schemes using the sixth-order filter shows very little difference. The presence of the shock wave reduces both schemes to first-order accuracy (the location of the shock is directly related to the grid spacing) nullifying any accuracy advantage of the Runge-Kutta scheme. The affect of fourth, sixth, and eighth order filters on the shock location and oscillations was examined with the Runge-Kutta scheme (figure 6.14(b)). The lower order filters reduced the oscillation without significant affect on shock location or strength.

Results of the 2D and 3D codes are shown in figure 6.15. For both numerical schemes the 2D and 3D pressure distributions compare very well.

6.7.3   Supersonic Cone

To test the axisymmetric terms in the two-dimensional/axisymmetric code and provide a true three-dimensional flowfield for the three-dimensional code, flow over a supersonic cone was validated. This test case uses the same flow conditions and turning angle as the wedge case. But, the body is treated as a body of revolution rather than a planar object. For the axisymmetric simulation, the grid for the wedge case was used (figure 6.13) and the axisymmetric source terms in the flow solver were activated.

The three-dimensional grid represents a 15 degree section of the cone and its flowfield. It was generated by rotating the 2D/axisymmetric grid about the centerline. A 2D/axisymmetric grid plane is located every one degree in the physical domain.

The exact solution for the pressure coefficient on the cone surface was obtained from the charts in NACA Report 1135, "Equations, Tables, and Charts for Compressible Flow" [67].

Results for both schemes in 2D are very good (figure 6.17). Both schemes smear the shock location over several grid points. Unlike the wedge calculation the shock oscillations are weaker and do not over-shoot the pressure behind the shock. The 3D results from the Gottlieb-Turkel scheme (figure 6.18(a)) differ from the 2D results due to a more pronounced pressure oscillation about the shock. The 3D results from the Runge-Kutta scheme (figure 6.18(b)) compare well to its 2D counterpart.
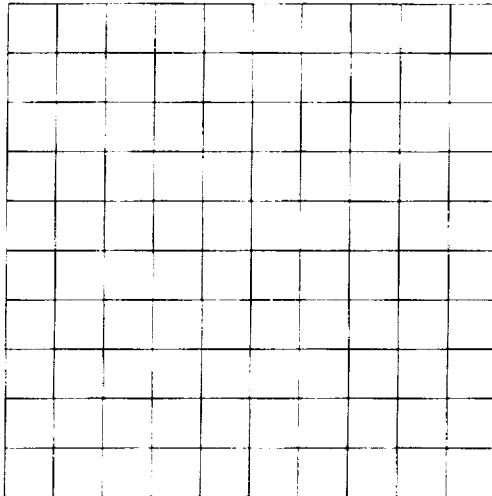
(a) computational grid
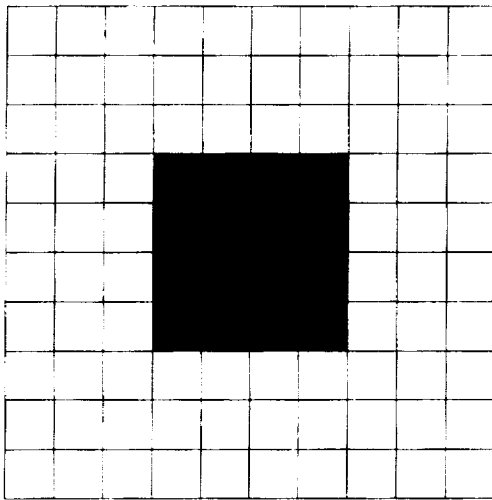
(b) internal object in grid
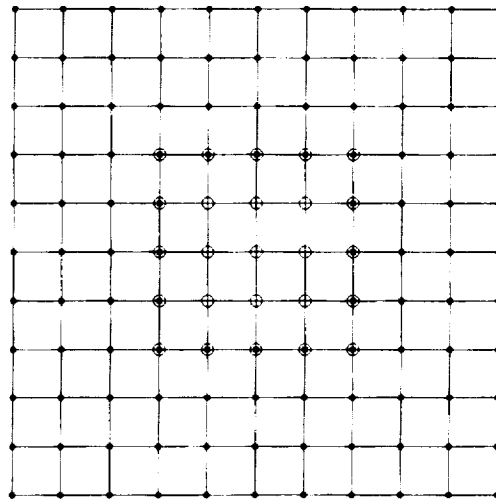
(c) grid point specification (filled = active, open = hole, both = boundary)

Figure 6.1: Modeling an internal object using hole points

(a) computational space   (b) physical space
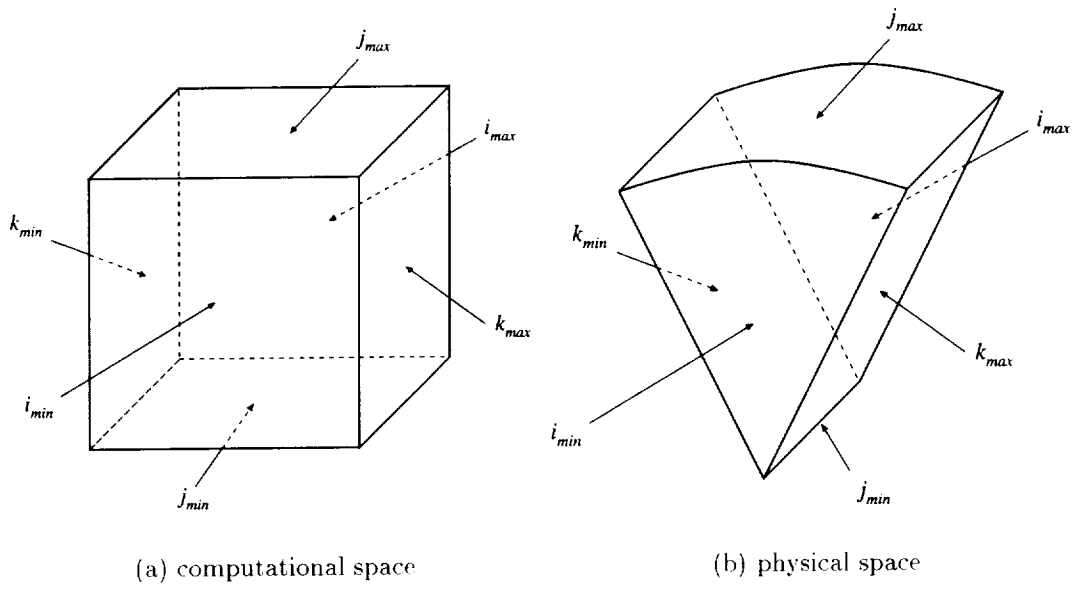
Figure 6.2: Pole boundary condition
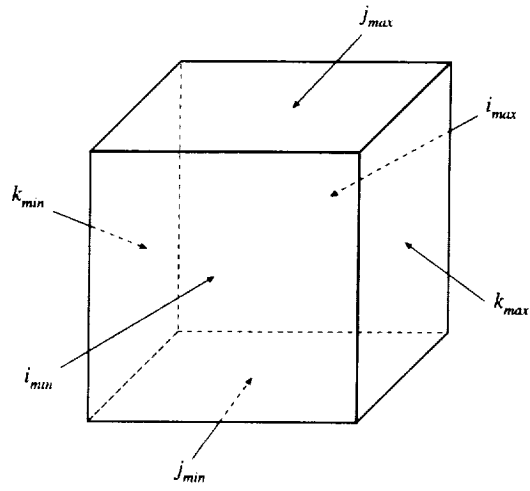
(a) computational space
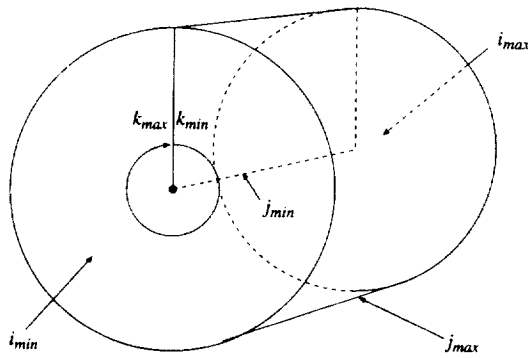
(b) physical space without overlap
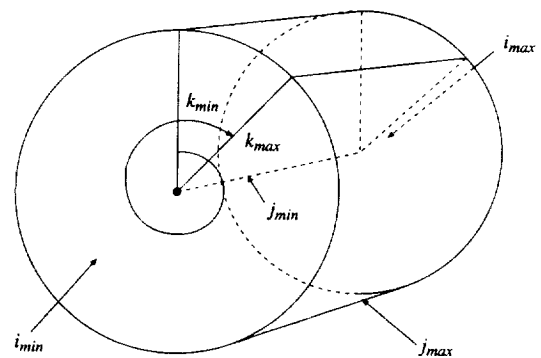
(c) physical space with overlap

Figure 6.3: Overlap boundary condition
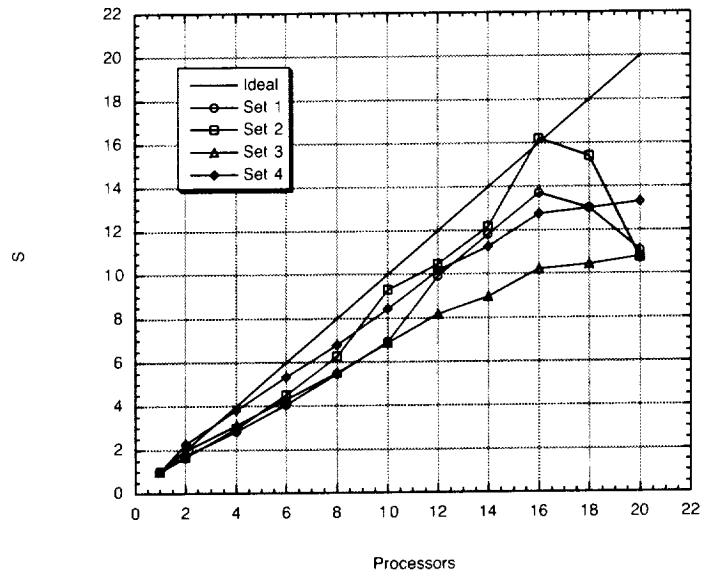
Figure 6.4: Parallel processing speedup
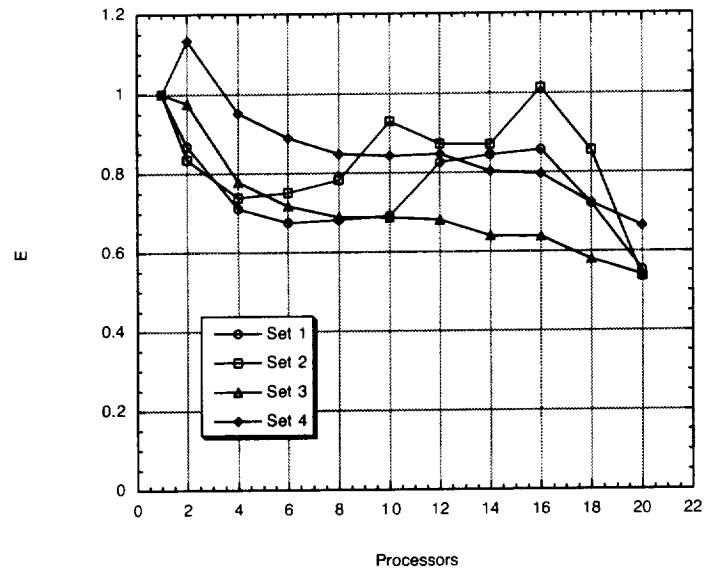
Figure 6.5: Parallel processing efficiency
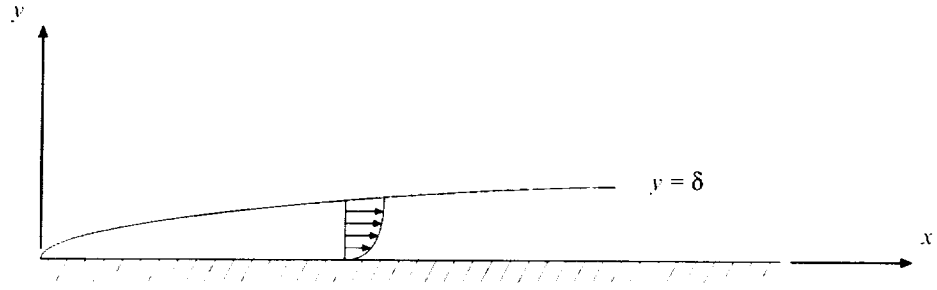
Figure 6.6: 2D laminar flat plate
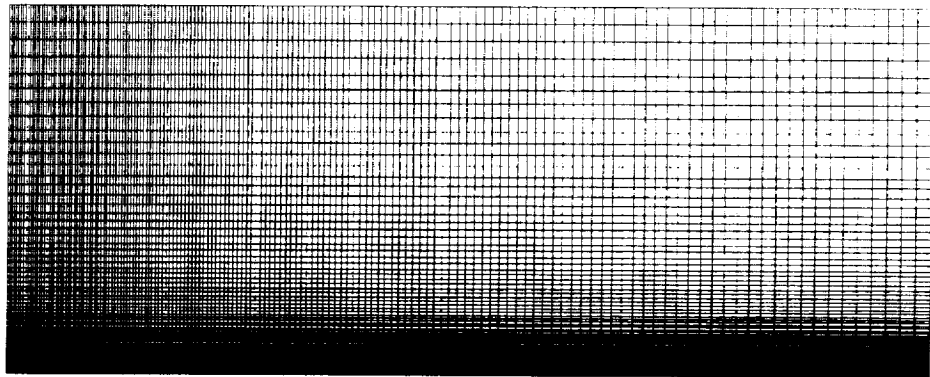
Figure 6.7: 2D grid for laminar flat plate calculations
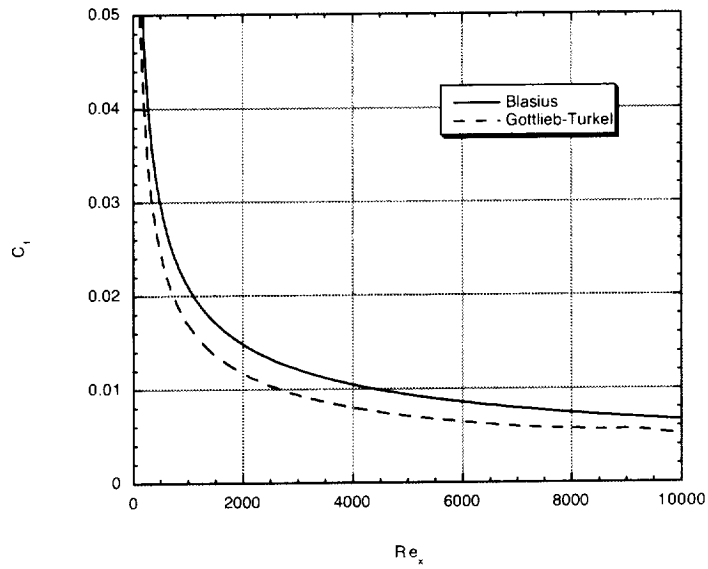
(a) Gottlieb-Turkel scheme
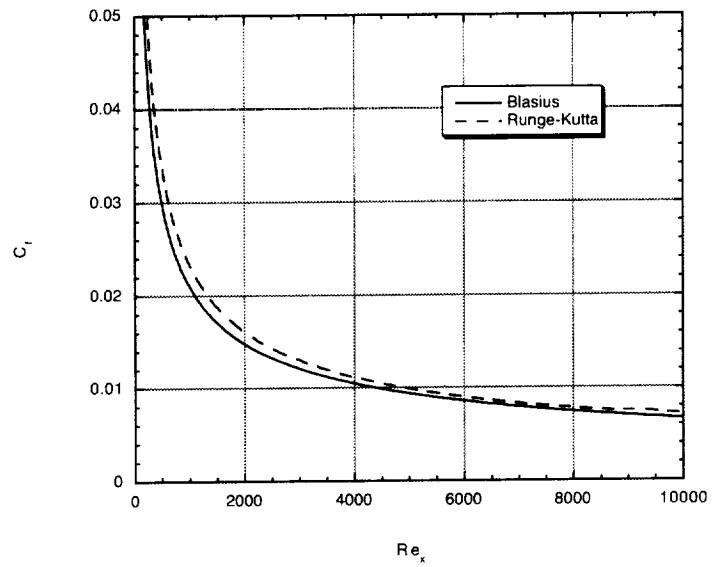
(b) Runge-Kutta scheme

Figure 6.8: Skin friction coefficient for laminar flat plate
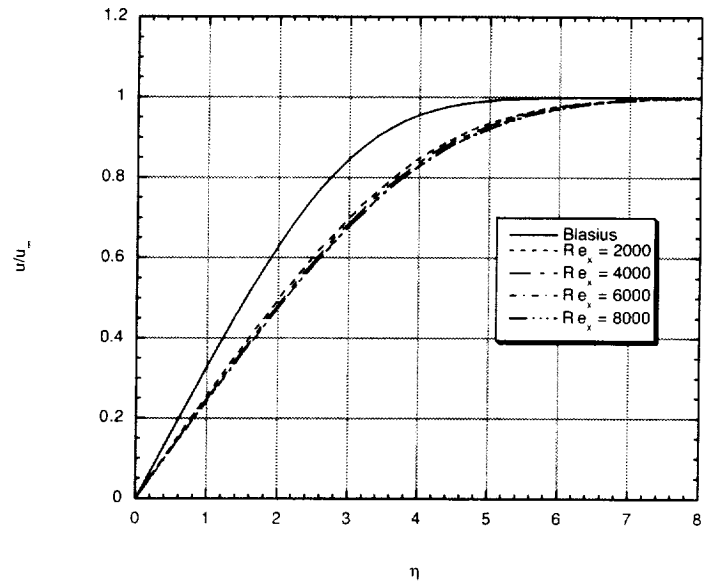
(a) Gottlieb-Turkel scheme
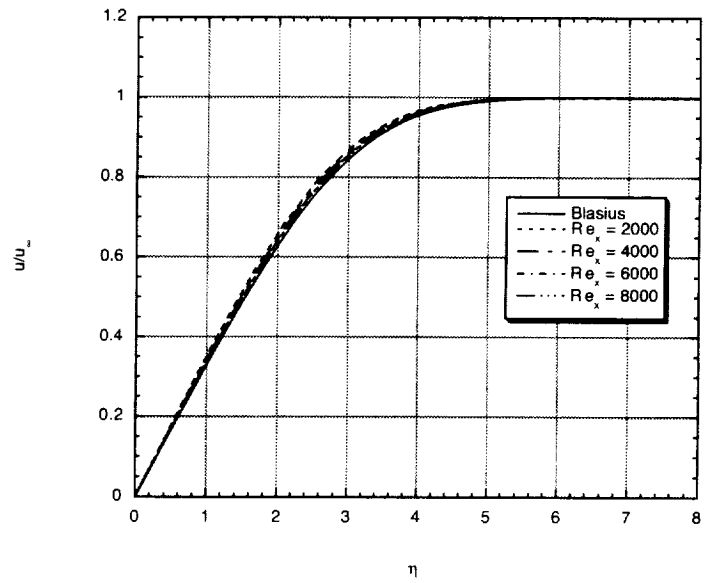
(b) Runge-Kutta scheme

Figure 6.9: Velocity profiles for laminar flat plate
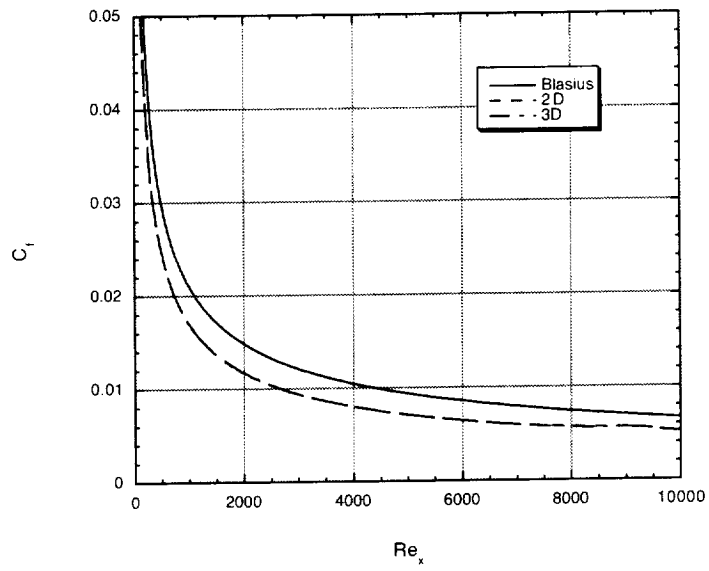
(a) skin friction coefficient
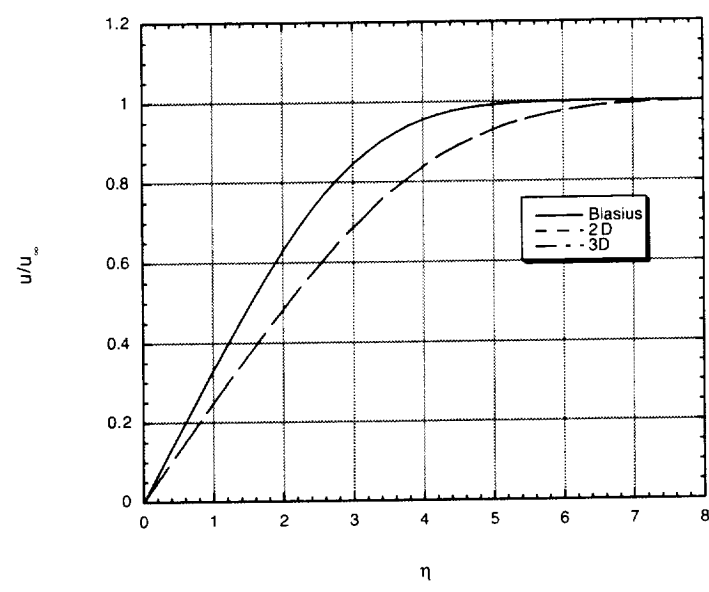
(b) velocity profiles at $Re_x = 4000$

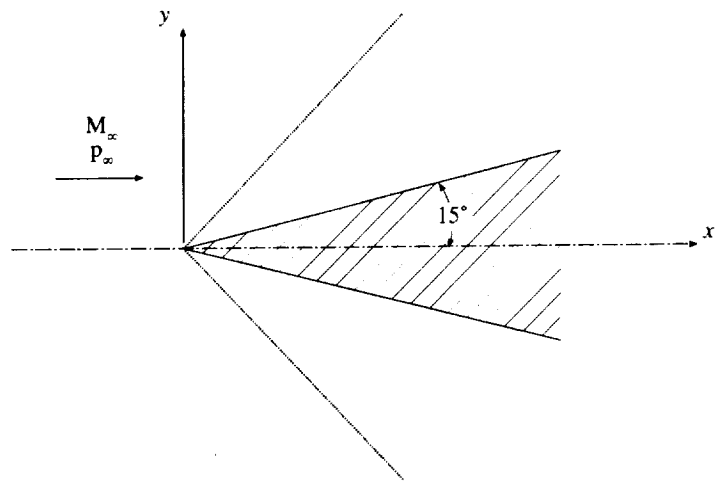Figure 6.10: Comparison of 2D and 3D Gottlieb-Turkel schemes for laminar flat plate
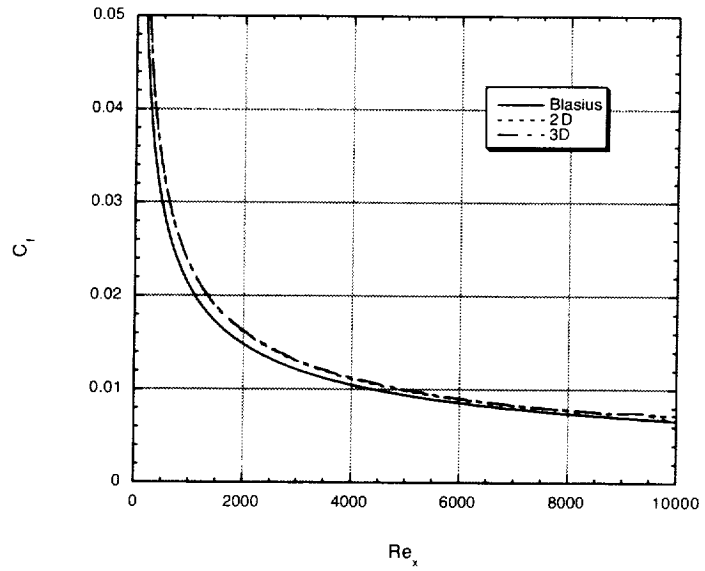
(a) skin friction coefficient
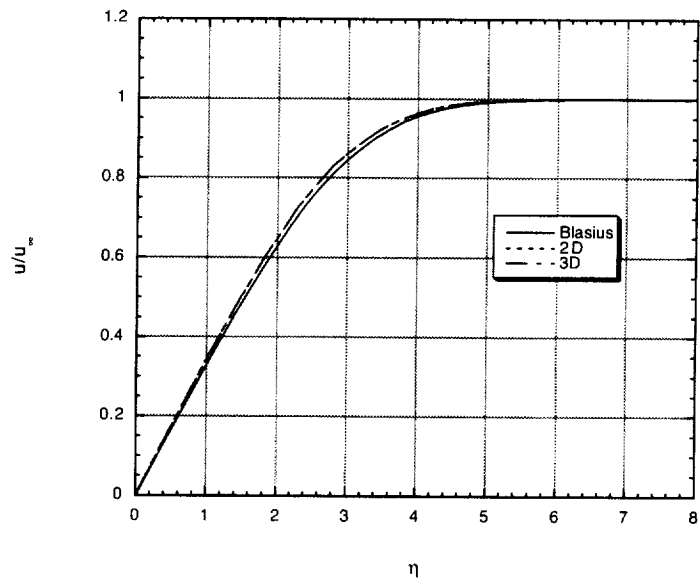
(b) velocity profiles at $Re_x = 4000$

Figure 6.11: Comparison of 2D and 3D Runge-Kutta schemes for laminar flat plate
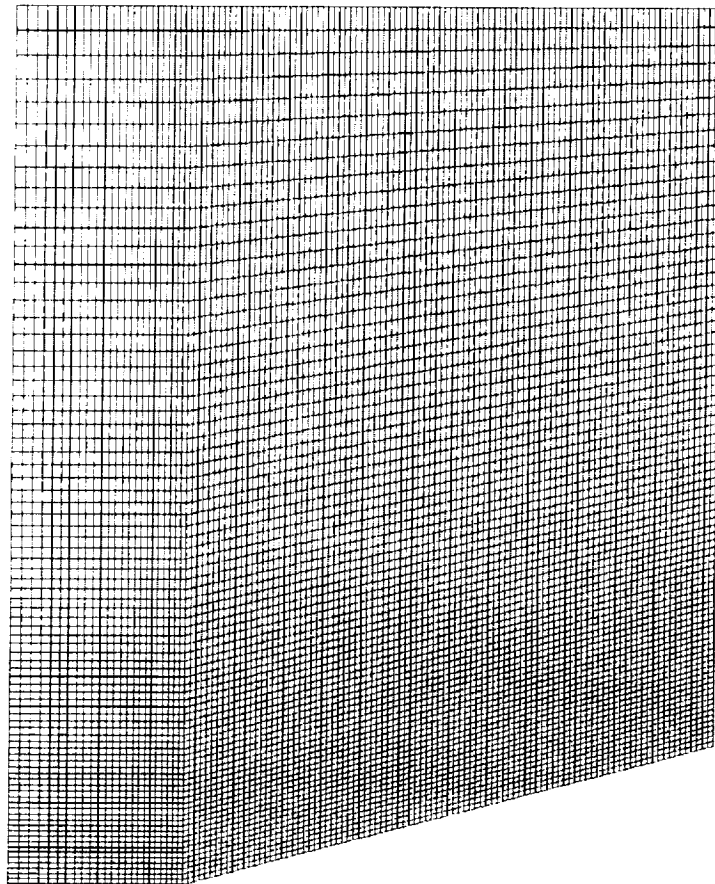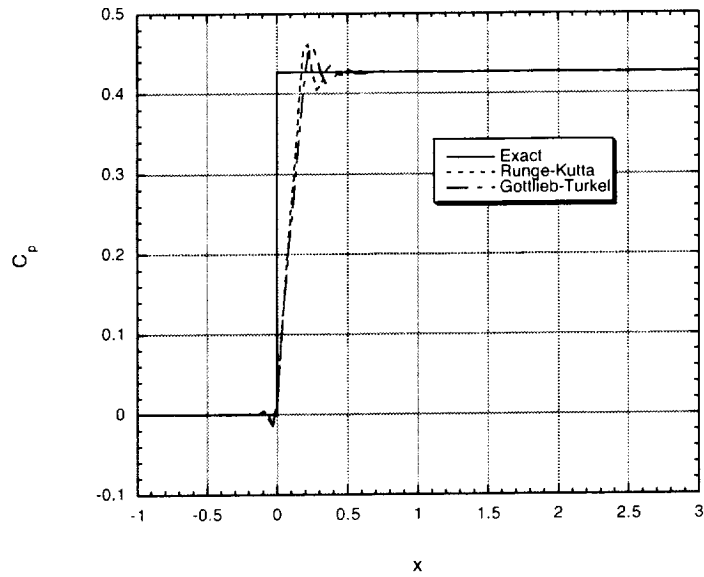
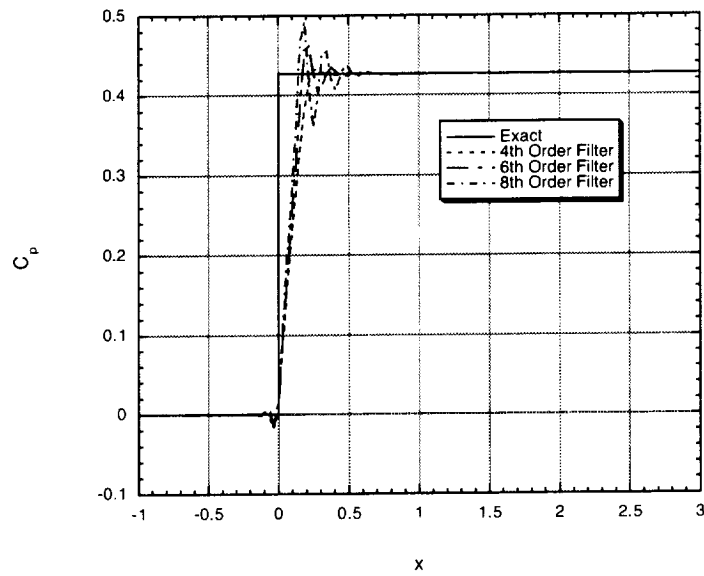Figure 6.12: Mach 2 flow over a 15 degree wedge

Figure 6.13: 2D grid for wedge and cone calculations
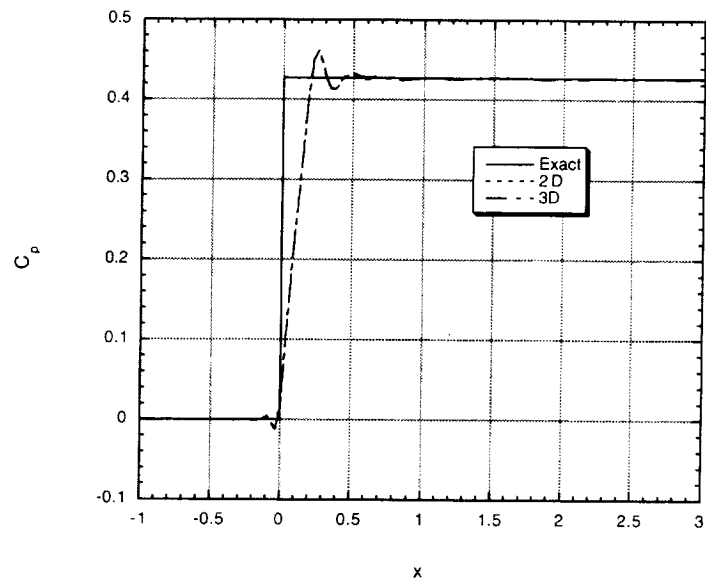
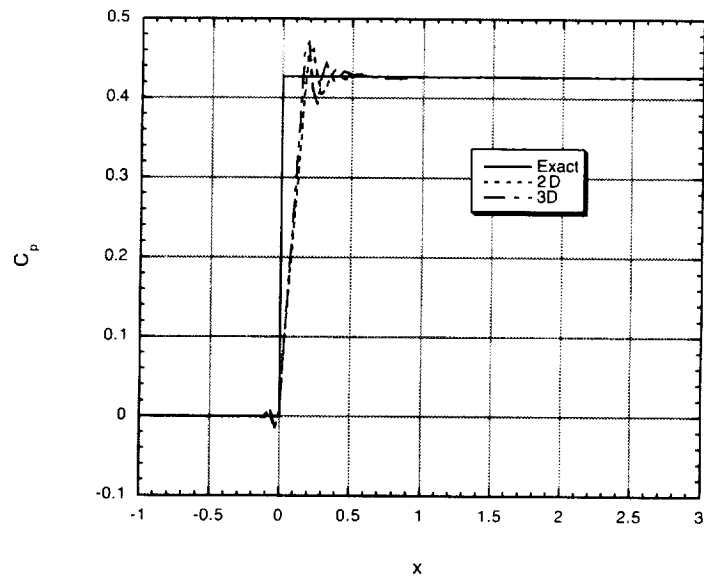(a) Comparison of numerical schemes with 6th order filter

(b) Comparison of filters with Runge-Kutta scheme

Figure 6.14: Pressure distribution on wedge surface

(a) Gottlieb-Turkel scheme

(b) Runge-Kutta scheme

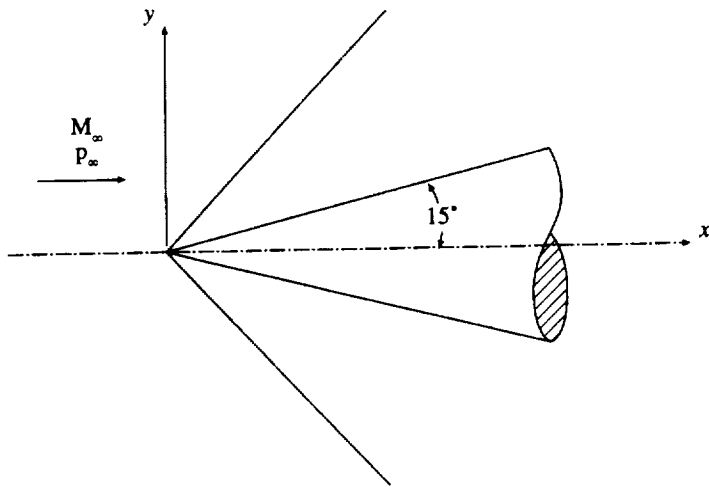Figure 6.15: Comparison of 2D and 3D codes for wedge calculation

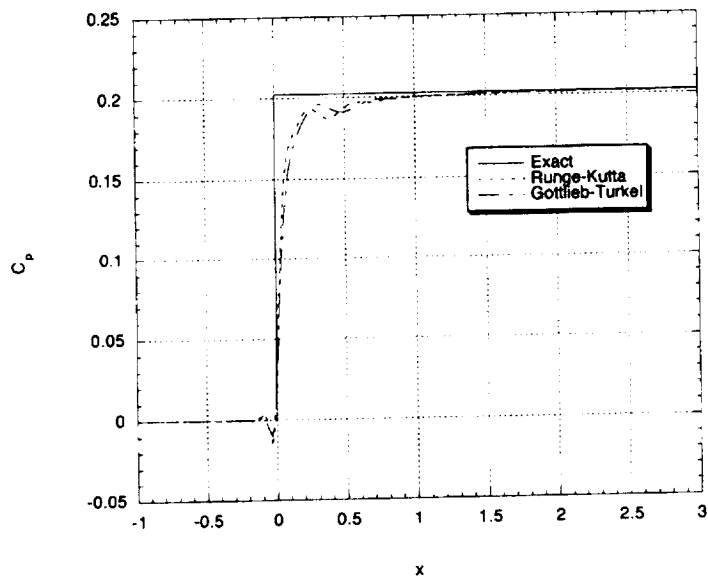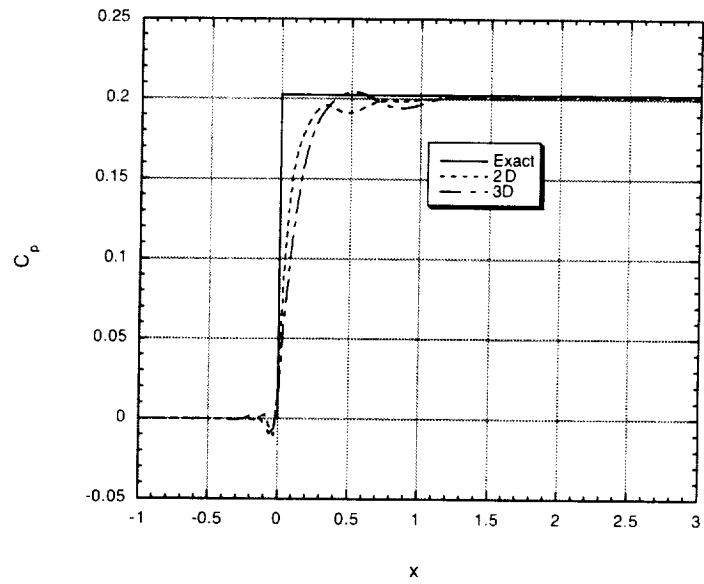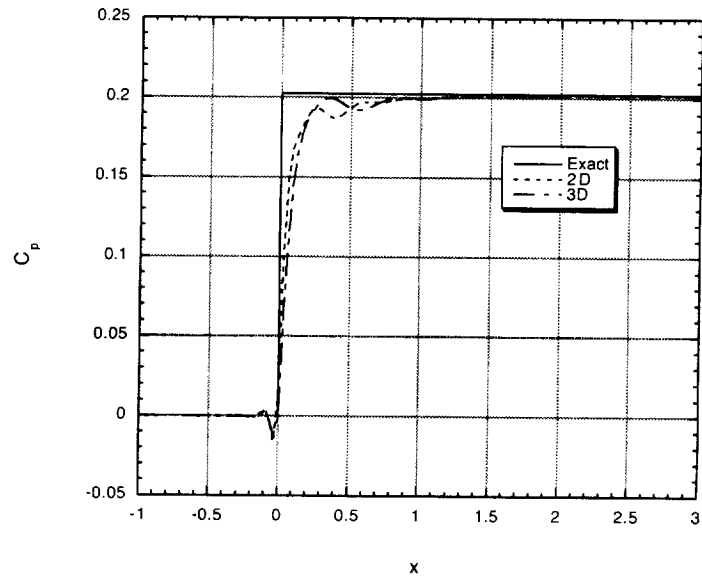Figure 6.16: Mach 2 flow over a 15 degree cone

Figure 6.17: Pressure distribution on cone surface

(a) Gottlieb-Turkel scheme

(b) Runge-Kutta scheme

Figure 6.18: Comparison of 2D and 3D codes for cone calculation

CHAPTER 7

COMPUTATION OF A NOZZLE FLOWFIELD

The flow solver described in the previous chapter is now applied to a round super-
sonic jet. The computational results are compared to high quality detailed data. The
effects of grid resolution and several numerical modeling parameters on the solution
are studied. Finally, a thorough examination of the flowfield is presented.

7.1   Description of the Nozzle

The nozzle geometry and data of Panda and Seasholtz [68-71] were selected for
study. This data set was obtained using the non-intrusive Rayleigh scattering tech-
nique. It is based on the measurement of laser light scattered by the air molecules.
This technique eliminates errors due to probe interference in hot wire and pitot probe
measurements and biasing errors due to seed particles in Laser Doppler Velocimetry
(LDV) and Particle Image Velocimetry (PIV) measurements. The data consists of
time averaged centerline and radial velocity profiles.

The nozzle is a one inch diameter convergent-divergent round nozzle with a de-
signed exit Mach number of 1.4. The nozzle exhausts into quiescent air. The Reynolds

number based on nozzle diameter is 1.2 million. The nozzle was operated at its minimum shock condition which was slightly less than its design Mach number. The operating conditions are given in table 7.1.

quantity	symbol	value	units
ratio of specific heats	γ	1.4	
nozzle plenum pressure	p_{0_j}	6524.9	$\frac{lbs}{ft^2}$
nozzle plenum temperature	T_{0_j}	540.0	R
nozzle exit Mach number	M_j	1.395	
nozzle exit diameter	D_j	0.0833	ft
jet velocity	U_j	1348.4	$\frac{ft}{}$
ambient pressure	p_∞	2064.8	$\frac{lbs}{ft^2}$
ambient temperature	T_∞	534.6	R
Reynolds number	Re_j	$1.2 \cdot 10^6$	

Table 7.1: Nozzle operating conditions

7.2 Flowfield Statistics

Analysis of RANS solutions is both simplified and limited by the Reynolds averaging process. The RANS codes readily provide a time averaged solution for analysis. However, these solutions lack any unsteady flowfield information. The unsteady solutions obtained here contain much more information. But the amount of information is overwhelming and must be processed and simplified before it can be successfully analyzed.

7.2.1 Time Averaging

The instantaneous solutions produced by the analysis code sometimes bear little resemblance to the time average of the flowfield. To compare the present results

with experimental data, empirical correlations and exact solutions a time average is computed as

$$\bar{\bar{f}}(x) = \frac{1}{\Delta t} \int_{t}^{t+\Delta t} f(x,t)dt \qquad (7.1)$$

and the instantaneous value of the function can be written as a sum of the time averaged and fluctuating quantities

$$f = \bar{\bar{f}} + f'' \qquad (7.2)$$

In this notation the traditional over-bar ($^-$) and prime ($'$) have been replaced with a double bar ($^=$) and double prime ($''$) to avoid confusion with the filtered quantities in the LES equations.

For the jet calculations a time average of density, pressure, and the three velocity components were kept. In addition, the time average of the squares of density and velocity components are kept to compute turbulent statistics.

7.2.2 Turbulent Statistics

Turbulent statistics can readily be computed from the time averaged flow variables being stored during the calculation.

$$\overline{\overline{f''^2}} = \overline{\overline{f^2}} - \overline{\bar{f}}^2 \qquad (7.3)$$

By substituting the velocity components into equation (7.3) we obtain the normal components of the Reynolds stress $\overline{\overline{u''^2}}$, $\overline{\overline{v''^2}}$, and $\overline{\overline{w''^2}}$. The root mean square value is simply

$$f_{rms} = \sqrt{\overline{\overline{f''^2}}} \qquad (7.4)$$

The root mean square velocities are typically expressed as turbulent intensities.

$$\hat{u} = \frac{u_{rms}}{U_j} = \frac{\sqrt{\overline{u''^2}}}{U_j} \tag{7.5}$$

$$\hat{v} = \frac{v_{rms}}{U_j} = \frac{\sqrt{\overline{v''^2}}}{U_j} \tag{7.6}$$

$$\hat{w} = \frac{w_{rms}}{U_j} = \frac{\sqrt{\overline{w''^2}}}{U_j} \tag{7.7}$$

Turbulent kinetic energy is defined as

$$k = \frac{1}{2}\left(\overline{u''^2} + \overline{v''^2} + \overline{w''^2}\right) \tag{7.8}$$

For the LES calculations the turbulent kinetic energy is comprised of resolved and sub-grid scale components.

$$k = \frac{1}{2}\left(\overline{\tilde{u}''^2} + \overline{\tilde{v}''^2} + \overline{\tilde{w}''^2}\right) + k_{sgs} \tag{7.9}$$

where

$$k_{sgs} = \frac{\bar{\bar{\tau}}_{kk}}{2\bar{\rho}} \tag{7.10}$$

We nondimensionalize k using the jet velocity.

$$k^* = \frac{k}{\frac{1}{2}U_j^2} \tag{7.11}$$

7.2.3   Two Point Correlations

Correlations of velocity signals at two points within the flowfield can lend insight into the structure of the turbulence [72] & [2]. Chu [73] experimentally applied two point correlations to jet flows. He obtained a turbulent length scale (eddy size) and convection velocity from the correlated data. Scott [74] presented preliminary two

point correlation data, obtained with CFD, for Chu's jet. While the comparison of the CFD and experimental correlations was inconclusive, due to insufficient simulation time, this work indicated CFD obtained correlations were were possible. Chu's methodology was followed in this study.

The location where the turbulent information is desired is specified by the vector φ_i, whose origin is at the center of the nozzle exit (figure 7.1). A pair of points evenly spaced on either side of this location is specified by a separation ψ_i. Instantaneous velocity data at these three points are saved for the correlations.

The general form of the two point space-time correlation coefficient is

$$\mathcal{R}(\psi_i, \tau) = \frac{\overline{U_\theta''(\varphi_i - \psi_i/2, t)\, U_\theta''(\varphi_i + \psi_i/2, t + \tau)}}{\overline{U_\theta''^2(\varphi_i, t)}} \tag{7.12}$$

where U_θ is the component of velocity that makes an angle θ with the jet axis and τ is a delay time. The correlation coefficient is a measure of similarity of the two signals. A value of $\mathcal{R}$ near ± 1 indicates that the two measurements are highly correlated.

The location about which the two point correlations were taken was located six jet diameters downstream of the nozzle exit on the jet lip line. Eight separations in the axial direction of up to one jet diameter were used. Table 7.2 summarizes the location and separation vectors for the two point correlations.

Turbulent Length Scale

Two point space correlations, where the delay time is zero ($\tau = 0$), can be used to determine a turbulent length scale. Several sets of correlation coefficients at different separations are computed. The separation distance over which the velocities are highly correlated is used as an estimate of the length scale ℓ.

$$\ell = \int_0^\infty \mathcal{R}(\psi_i, 0)\, d\psi_i \tag{7.13}$$

vector		coordinates
location	o_i	$[6D_j, D_j/2.0]^T$
1st separation	ψ_i^1	$[D_j/8, 0, 0]^T$
2nd separation	ψ_i^2	$[D_j/7, 0, 0]^T$
3rd separation	ψ_i^3	$[D_j/6, 0, 0]^T$
4th separation	ψ_i^4	$[D_j/5, 0, 0]^T$
5th separation	ψ_i^5	$[D_j/4, 0, 0]^T$
6th separation	ψ_i^6	$[D_j/3, 0, 0]^T$
7th separation	ψ_i^7	$[D_j/2, 0, 0]^T$
8th separation	ψ_i^8	$[D_j, 0, 0]^T$

Table 7.2: Two point correlation location information

Convection Velocity

Two point space-time correlations can be used to determine the convection velocity of a turbulent eddy. For a given separation, ψ_i, the correlation coefficient is computed over a range of delay times. The value of τ where the correlation coefficient is a maximum indicates the time necessary for a disturbance at the upstream point ($\phi_i - \psi_i/2$) to reach the downstream point ($\phi_i + \psi_i/2$). This time and the separation distance are then used to compute the convection velocity.

$$U_c = \frac{|\psi_i|}{\tau|_{R_{max}}} \qquad (7.14)$$

7.3 Axisymmetric Solutions

Assuming that the flow is symmetric about the jet axis reduces the problem to two dimensions. Using this assumption would significantly decrease the computational expense of a solution and allow for a greater number of parametric investigations to be done. However, turbulence is inherently three-dimensional and it is not expected

that a solution obtained with the axisymmetric version of the CFD solver will yield physically realistic results. Here, the axisymmetric analyses are used to investigate numerical issues, grid resolution, numerical scheme, and boundary conditions, and the knowledge gained is applied to the three-dimensional simulations.

7.3.1 Grid Generation

The computational grid specifies the nozzle geometry and computational domain for the calculations. Unlike previous LES analyses of jets, the internal nozzle contour and nozzle lip were modeled. The internal nozzle boundary layer and vortex shedding from the nozzle lip may affect the growth and stability of the shear layer. It was felt that it was important to include these effects in the simulation. Also, by including the internal nozzle the inflow boundary is moved away from the region of interest, the jet shear layer, reducing the influence of the artificial boundary condition.

The computational grids used for the analyses were generated using the commercial software package Gridgen [75]. The grid points were clustered near the nozzle walls using hyperbolic tangent stretching to resolve the boundary layers [76]. The grid was also clustered near the nozzle exit plane to capture the unsteady vortex shedding from the nozzle lip and the initial formation of the shear layer. The cell aspect ratio at the upper and lower corners of the nozzle lip was set to one. Grid point clustering in the expected region of the shear layer downstream of the nozzle lip was also implemented. The computational domain extends 20 nozzle diameters downstream of the nozzle exit in the axial direction and 10 nozzle diameters from the jet centerline in the radial direction. A representative grid with 301 point in the axial direction and 129 points in the radial direction is shown in figure 7.2.

7.3.2   Specification of Boundary Conditions

All the axisymmetric jet computations used the same boundary conditions (figure 7.3). Subsonic inflow using the jet plenum conditions was specified at the inflow of the internal nozzle section. The no-slip wall condition was used for the internal and external nozzle surfaces. An axis of symmetry/slip wall condition was used on the jet centerline.

Simulating the quiescent conditions of the surroundings can cause numerical difficulties. The boundary conditions are formulated assuming a known flow direction (inflow or outflow). In the still air small disturbances may cause portions of a boundary to have an inflow and other portions to have an outflow. This leads to over or under specification of the boundary and numerical errors result. To overcome this problem a small freestream flow is imparted to ensure a coherent flow direction and properly specified boundaries. In this case a Mach 0.05 freestream was used. Subsonic inflow was specified on the upstream external boundary using the freestream total conditions. Conditions on the upper boundary were extrapolated from the freestream.

The subsonic outflow boundary condition imposes a constant pressure over the entire boundary. In reality the pressure on the outflow boundary varies in both time and space. To accommodate this pressure variation while maintaining the correct freestream flow a combination of subsonic outflow and extrapolation conditions were used. The subsonic outflow condition was specified on the upper portion of the downstream boundary to maintain the correct pressure level in the freestream. Conditions on the rest of the downstream boundary were extrapolated from the interior to accommodate both temporal and spatial pressure variations near the jet centerline.

7.3.3 Effect of Grid Resolution

The effect of grid resolution on the solution was investigated. Three grids were used, where the grid spacing in each direction was halved from the previous grid. All solutions were obtained with the Runge-Kutta scheme using an eighth-order filter. The sub-grid scale model was not used. Because the grid spacing is not uniform, it is difficult to quantify. Here, the spacing was represented by a nondimensional computational grid size.

$$\Delta x^* = \sqrt{\Delta \xi \cdot \Delta \eta} \qquad (7.15)$$

As the grid resolution was increased, the resolution of the unsteady flowfield im-

grid	dimensions			Δx^*	$\hat{\hat{u}}_{max}$	$\hat{\hat{v}}_{max}$	k^*_{max}
coarse	151	x	65	$1.0206 \cdot 10^{-2}$	0.20006	0.15480	0.047999
medium	301	x	129	$5.1031 \cdot 10^{-3}$	0.26266	0.20305	0.096392
fine	601	x	257	$2.5516 \cdot 10^{-3}$	0.32909	0.22788	0.12178

Table 7.3: Effect of grid resolution on axisymmetric solution

proved. The change in entropy of the flowfield can be used to visualize the turbulent structures in the flowfield. The viscous mixing of the jet and ambient air increases the entropy of the flow. The vortices alter the shape of the mixing region and this altered shape can be seen in the gradients of entropy in the mixing layer. Figure 7.4 shows contours of entropy for the three grids used. The plots show a dramatic increase in the resolution of vortical structures with grid resolution. A more quantitative measure, the maximum of the turbulent statistics in the flowfield, are shown in figure 7.5. The turbulent intensities and kinetic energy increase as the grid spacing decreases (as the

grid	dimensions			$\overline{\Delta x}/\kappa$
coarse	151	x	65	2081.5
medium	301	x	129	1040.8
fine	601	x	257	520.40

Table 7.4: Comparison of grid spacing to the Kolmogorov scale

grid resolution increases). This result is expected as the intensities and kinetic energy should increase as the grid is refined and the scheme increasingly captures more of the smaller energy containing eddies. With even further resolution one could expect the energy to decrease as the inertial subrange and Kolmogorov scales are reached, where the energy is dissipated.

To compare the grid spacing to the Kolmogorov scale, an average cell size was computed as follows

$$\overline{\Delta x} = \Delta x^* \sqrt{L_{grid} \cdot H_{grid}} \qquad (7.16)$$

where L_{grid} and H_{grid} are the overall length and height of the grid. The Kolmogorov scale was estimated using equation (1.1) and assuming the integral length scale is approximately $\frac{1}{2}D_j$. Table 7.4 shows that even for the finest grid the cell size is over 500 times larger than the Kolmogorov scale.

7.3.4 Comparison of Numerical Schemes

A comparison of the two numerical schemes was performed on the medium sized grid (301 x 129). The solutions were run for two characteristic acoustic times (the time for an acoustic wave to pass through the solution domain) to establish proper initial conditions for obtaining turbulent statistics. The solutions were then run for an

additional two characteristic times and the flowfield was averaged. Both schemes were run using their maximum stable time step. Figure 7.6 shows the entropy contours for the two schemes. The Runge-Kutta scheme exhibits more vortical structure and the initial vortex roll-up of the shear layer occurs earlier. Table 7.5 quantifies the results in terms of turbulent intensities and kinetic energy. The Runge-Kutta scheme predicts higher maximum turbulent intensities and kinetic energy than the Gottlieb-Turkel scheme. indicating better resolution of the flowfield. The simulation time presented in the table is the ratio of the time required to the time required for the Gottlieb-Turkel scheme. Consistent with the one-dimensional results. the Runge-Kutta scheme is more computationally efficient, using 16.5 percent less CPU time.

scheme	$\widehat{\widehat{u}}_{max}$	$\widehat{\widehat{v}}_{max}$	k^{*}_{max}	time
Gottlieb-Turkel	0.26033	0.18561	0.080193	1.00000
Runge-Kutta	0.26266	0.20305	0.096392	0.83523

Table 7.5: Effect of numerical scheme on axisymmetric solution

7.3.5 Evaluation of Exit Zone Boundary Condition

The use of an exit zone outflow boundary has been advocated in the area of computational aeroacoustics where proper resolution of very low magnitude acoustic waves is critical. It is not clear that an exit zone is required when the simulation is not intended to capture acoustic waves. The need for and effectiveness of the exit zone boundary condition was tested by comparing solutions with and without this boundary treatment. The computational grid was modified by adding an exit zone.

a region of highly stretched grid cells downstream of the previous outflow boundary (figure 7.7). Fifteen additional grid planes were added using a ten percent geometric stretching factor. The simulations were run using the Runge-Kutta scheme with a sixth-order filter.

Entropy contours show some differences in the turbulent structures. But, it is not clear that the differences are due to any reflecting waves. Turbulence levels given in table 7.6 indicate very little difference between the two solutions.

boundary condition	$\widehat{u}_{max}$	$\widehat{v}_{max}$	k^*_{max}
Exit Zone	0.30181	0.20379	0.096595
No Exit Zone	0.26266	0.20305	0.096392

Table 7.6: Effect of exit zone boundary condition on axisymmetric solution

7.3.6   Effect of the Sub-Grid Scale Model

The solutions obtained thus far have not used the sub-grid scale model. They are in effect DNS solutions. However, the grids used are not fine enough to resolve all the turbulent scales. Scales smaller than the grid size are not computed and their contribution is lost. Since these scales tend to dissipate the larger eddies, the solutions without the sub-grid model should predict larger more energetic eddies than a corresponding LES solution. The use of the term DNS to describe these solutions is misleading because DNS implies that all the turbulent scales are computed. Therefore, these solutions will be referred to as "coarse grid DNS" solutions.

An LES solution on the medium grid was run and compared to its "coarse grid DNS" counterpart. Entropy contours are compared in figure 7.9. The additional dissipation from the sub-grid model serves to damp the large scale structures. This behavior is evident by observing the initial vortex roll-up in the mixing layer. The first large eddies occur further downstream in the LES solution due to the eddy viscosity from the sub-grid model. Overall, the LES solution produces less turbulent mixing, 7 percent less turbulent intensity and 14 percent less turbulent kinetic energy (table 7.7).

small scale modeling	$\widehat{\widehat{u}}_{max}$	$\widehat{\widehat{v}}_{max}$	k^*_{max}
without sub-grid model	0.26266	0.20305	0.096392
with sub-grid model	0.24247	0.18797	0.082770

Table 7.7: Effect of sub-grid scale model on axisymmetric solution

7.3.7 Evaluation of the Axisymmetric LES Solution

To obtain a steady time averaged solution, the LES solution was run for 100,000 iterations, which corresponds to 0.0052 seconds of simulation time. The instantaneous solution was averaged every 100 iterations.

Analysis of the Flowfield

Contour plots of sample instantaneous and time averaged flowfield quantities are shown in figures 7.10 through 7.12. The turbulent structures present in the mixing layer are clearly seen in the instantaneous contour plots. The density contours (figure 7.10) reveal the shock structure in the potential core. The radial velocity contours

(figure 7.12) provide good visualization of the vortical structures. The time averaged plots show smoothly varying gradients in the mixing layer and are analogous to a flowfield obtained from a RANS solution or analytic method.

Plots of $\hat{\rho}$, $\hat{u}$, $\hat{v}$, and k, are show in figures 7.13 through 7.16. All the turbulent quantities exhibit a similar structure. The detail plots of the nozzle exit show a small concentrated unsteady region at the nozzle lip caused by vortex shedding. This region is followed by a region dominated by very small scale turbulence. Radial velocity contours in this region (figure 7.17(a)) show that no large scale structures exist. But, a plot of the sub-grid scale turbulent kinetic energy, τ_{kk}, shows that the energy from the small scales peak in this region (figure 7.17(b)). Downstream of the small scale region, the mixing layer becomes unstable and large vortical structures begin to form and grow larger with increasing distance from the nozzle exit.

Comparison to Experimental Data

The time averaged solution is compared to the experimental data in figures 7.18 and 7.19. The experimental data exhibits the behavior of a typical jet [77,78]. A series of weak shock waves can be seen near the nozzle exit. The end of the potential core, as indicated by the start of the velocity decay on the centerline, is at approximately 7.5 jet diameters. The predicted velocity on the jet centerline captures the first few shock waves near the exit. The remaining shocks are not captured due to grid stretching away from the nozzle exit. The predicted centerline velocity does not decay within the computational domain indicating that the axisymmetric assumption has constrained the mixing layer to lie above the jet axis. Radial profiles of axial velocity at $x/D_j = 2$, 4, 6, 8, 10, and 12 are shown in figure 7.19. The experimental data

was taken both above and below the jet axis. All these data are plotted to show the asymmetry in the data. For comparison the LES solution is reflected about the axis. Agreement between the CFD and experiment is very good up to 6 jet diameters. Beyond this point the prediction departs from the experiment due to the lack of decay of the potential core. The peak in the experimental profiles begins to decrease and the jet spreads at a greater rate than the CFD indicates. The good agreement upstream of the end of the potential core indicates that the axisymmetric assumption is valid in this region. In the region where the potential core breaks down, highly three-dimensional turbulent structures may be the cause.

7.4 Three-Dimensional Solutions

A large-eddy simulation of the full three-dimensional jet flowfield is a large undertaking. The number of grid points and time necessary for a solution severely limit the size and number of calculations. The results from the axisymmetric solutions, code validation, and one-dimensional error analysis were used to guide the simulation process. The Runge-Kutta scheme has been proven superior to the Gottlieb-Turkel scheme and was used for all 3D computations.

Three computations were performed. The first used the sixth-order filter and provided time averaged flowfield data. The second calculation used the eighth-order filter and was used to ascertain the effect of the solution filter and to obtain turbulent statistics and a series of instantaneous velocity distributions. The third used the sixth-order filter and a modified grid to obtain two point correlation information.

7.4.1 Grid Generation

The axisymmetric grid study showed an increase in resolution of the turbulent structures with increasing grid resolution. But, a trade between accuracy and computational cost must be made to keep the simulation time reasonable. The resolution used in the fine grid would create a prohibitively large 3D grid and the coarse grid showed no visible turbulent structures. The medium grid (301 x 129) showed resolution of large scale turbulence and provides a basis for a reasonably sized 3D grid. Also, a reasonable sub-grid model should replace the effect of the unresolved terms. To form the three-dimensional grid, a grid plane corresponding to the axisymmetric grid was positioned at every ten degrees around the jet axis resulting in a cylindrical domain. Four additional grid planes were added overlapping the first four planes to facilitate use of the overlap boundary condition. The final grid has dimensions 301 x 129 x 40 and contains 1,553,160 points. Figure 7.20 shows streamwise and cross-stream grid planes.

The grid was modified slightly for the two point correlation work. The grid points were redistributed locally so that a grid point was located at each correlation location (table 7.2). The overall grid structure and size remained the same.

7.4.2 Specification of Boundary Conditions

Boundary conditions are specified in the same manner as done in the axisymmetric case (section 7.3.2). No-slip walls are specified on the nozzle surfaces. Subsonic inflow conditions are used for the nozzle plenum and freestream inflow boundaries. The combination of extrapolation and subsonic outflow are used on the outflow plane to allow for pressure variation and extrapolation is used on the upper boundary.

Two additional boundary conditions are necessary for the 3D grid. First the overlap condition is used to create a continuous domain in the azimuthal direction. Second, the jet centerline consists of a grid plane that is collapsed to a line. The pole boundary is used here.

7.4.3 Presentation of the Time Averaged Flowfield

The LES simulation was run until the time averaged centerline velocity profile remained unchanged for over 5,000 iterations. This required 50,500 iterations using an average time step of approximately $48 \cdot 10^{-9}$ seconds. Using 16 processors on the Silicon Graphics Power Challenge machine, the simulation required about two months of calendar time for completion. The solution was averaged every 100 iterations.

Contours comparing instantaneous and time averaged velocities in both the streamwise and cross-stream planes are presented in figures 7.21 - 7.26. The difference between the instantaneous and time average is striking. The instantaneous velocities show large turbulent structures that average to zero over time. Large azimuthal velocities and the appearance of turbulent structures that cross the jet axis near the end of the potential core indicate a highly three-dimensional flowfield.

Radial velocity and sub-grid turbulent kinetic energy near the jet lip are shown in figure 7.27 and differ from the axisymmetric solution (figure 7.17). In the mixing layer the vortical structures in the 3D solution appear weaker because of the 3D relief effect not accounted for in the axisymmetric solution. Also, the 3D solution does not show any resolved vortices near the jet lip. The sub-grid turbulent kinetic is much higher, in the 3D solution, indicating that the sub-grid model has dissipated this motion. The increased effect of the sub-grid model may be caused by the large grid

spacing in the azimuthal direction. This large grid spacing results in a larger filter width, which increases the amount of eddy viscosity (equation (5.19)).

Contours of dilatation, $\frac{\partial u_i}{\partial x_i}$, are shown in figure 7.28. By rewriting the continuity equation (equation 2.1) we can see that dilatation is related to the convection of density waves, which can be related to the convection of sound waves.

$$\frac{\partial u_i}{\partial x_i} = -\frac{1}{\rho} \left(\frac{\partial \rho}{\partial t} + u_i \frac{\partial \rho}{\partial x_i} \right) \tag{7.17}$$

The dilatation contours show that the sound for this jet would emanate from the mixing layer near and the end of the potential core.

The time averaged velocities closely resemble both experimental data and RANS calculations. But, clearly the LES solution is capable of providing much more insight into the flow physics of the jet through the unsteady information.

The time averaged velocity profiles on the jet centerline are presented in figure 7.29. The LES solution predicts that the potential core is shorter than found experimentally indicating that the turbulent eddies are too energetic. The sub-grid model may not be providing adequate dissipation of the large scale eddies. Adjusting the constants to the model may correct this problem. The rate of velocity decay beyond the potential core is very close to that of the experimental data.

Radial profiles of axial velocity at $x/D_j = 2$, 4, 6, 8, 10, and 12 are shown in figure 7.4.5. At $x/D_j = 2$ and 4 the 3D prediction shows less spreading than either the experimental data or the axisymmetric prediction. This difference may be caused by the truncation error due to the large grid spacing in the azimuthal direction. The spacing in the azimuthal direction is much larger than the spacing in the axial and radial directions and is the reason for the difference between the axisymmetric

and 3D solutions. Since the grid resolution is not sufficient to capture the turbulent structures in this region, the sub-grid model should provide the equivalent effect through increased eddy viscosity. The fact that the LES solution predicts less jet spreading than the experiment indicates that the sub-grid model is not adequate.

While the agreement with the experimental data is far from perfect, this calculation is superior to the other high Reynolds number LES calculations in the literature [31–33].

7.4.4 Presentation of the Instantaneous Flowfield and Turbulent Statistics

A second nearly identical simulation was run to obtain turbulent statistics and instantaneous flowfield data not saved during the first simulation. The order of the filter was changed from sixth to eighth to ascertain its effect. The simulation was again run until the centerline velocity profile did not change over a period of 5.000 iterations. The time step was fixed at $50 \cdot 10^{-9}$ seconds and 70.200 iterations were required. The solution was averaged every 80 iterations. The increase in the filter's order reduced the amount of numerical dissipation in the solution and increased the resolution of the high wave number disturbances. This leads to increased turbulent mixing as shown in the centerline velocity profile (figure 7.31). The increased turbulent structures are most likely the reason why more simulation time was required to obtain a suitable average. In theory the sub-grid scale model should adjust to the change in flowfield resolution and filter and grid independence should be possible. The increase in resolution of the turbulent eddies, with a corresponding increase in $|\widetilde{S}|$ should be compensated for by an increase in eddy viscosity (equation 5.19). It is evident that the current model and the choice of coefficients are not adequate for this problem.

Instantaneous velocity contours at three times are shown in figures 7.32 - 7.37. The contours indicate that the jet flowfield is highly three dimensional with very large scale structures. Significant variation with time is found not only in the mixing layer, but also in the potential core. Here the core flow "flaps" and rotates about the jet axis. Also, the shock structure varies considerably due to the variation in the boundary between the core flow and mixing layer caused by the vortical motion in the mixing layer.

Turbulent intensities and turbulent kinetic energy are presented in figures 7.38 and 7.39. The axial turbulent intensity peaks at $\hat{\hat{u}} = 0.4123$ in the mixing layer near the nozzle lip. Unsteady motion is also found in the potential core, due to the unsteady shock structure, and in the freestream, due to acoustic waves. The radial and azimuthal intensity plots are lower in magnitude and peak at a value of $\hat{\hat{u}} = 0.2002$ at the end of the potential core. They have very similar structures except for two very low intensity regions. The first is the unsteady radial component of velocity induced by the shocks in the potential core. The second is a wide region of unsteadiness in radial velocity at the downstream boundary.

Turbulent kinetic energy is plotted in figure 7.39. The peak values, $k^* = 0.1760$, occur in the mixing layer just downstream of the nozzle lip. A second lower peak, $k^* = 0.1210$, occurs near the end of the potential core.

The anisotropy of the turbulence is easily seen in figure 7.40. The ratio of radial to axial turbulent intensity, $\hat{\hat{u}}/\hat{\hat{v}}$, is shown in three plots with different contour levels to separate the regions of isotropy and anisotropy. The vast majority of turbulent structures are anisotropic with a peak ratio of 2.775. The majority of the flowfield

has a ratio in the range $1.2 \leq \widehat{\bar{u}}/\widehat{\bar{v}} \leq 2.0$ This result indicates that the isotropic assumptions of most RANS turbulence models are not applicable for this flow.

7.4.5 Presentation of the Two Point Correlation Data

A simulation on the modified 3D grid was run using the sixth-order filter and axial and radial velocity data were saved for correlation. These velocity components can be combined to form the velocity vector making an angle theta with the jet axis.

$$U_\theta = u \cos\theta + v \sin\theta \qquad (7.18)$$

A time history of the velocity signals at the points for the fourth separation, $1/2D_j$, are shown in figure 7.4.5. Three angles are examined 0, 45, and 90 degrees. There is very little change in the velocity signal as it convects from the upstream to the downstream point. The average velocity and turbulent intensity for each angle is given in table 7.8

θ	$\bar{U}_\theta/U_j$	$\widehat{\bar{U}}_\theta/U_j$
0	0.65417	0.26473
45	0.46029	0.26601
90	-0.0032162	0.17076

Table 7.8: Velocity statistics at the two point correlation location

Two Point Space Correlation

A plot of the two point correlation coefficients versus separation distance is shown in figure 7.42. The correlation of the velocity signal decreases towards zero with

increasing separation distance indicating that the average size of the turbulent structures is less than the maximum separation distance (one jet diameter). The turbulent length scale was estimated using equation (7.13). To evaluate the integral, the data was fit with a sixth-order polynomial using the method of least squares [79]. The polynomial is of the form

$$y = c_6 x^6 + c_5 x^5 + c_4 x^4 + c_3 x^3 + c_2 x^2 + c_1 x + c_0 \qquad (7.19)$$

The coefficients obtained in the curve fitting are found in table 7.9. The polynomial

angle	coefficient							
	c_0	c_1	c_2	c_3	c_3	c_5	c_6	l_2 norm
0	1.000	0.04124	-4.230	5.458	-1.940	-1.458	1.105	$8.564 \cdot 10^{-6}$
45	1.004	-0.01181	-5.249	6.480	-1.736	-2.002	1.305	$9.989 \cdot 10^{-6}$
90	1.003	0.03630	-11.13	16.46	-2.633	-8.769	4.687	$4.052 \cdot 10^{-5}$

Table 7.9: Curve fit coefficients for two point space correlations

was then integrated analytically to obtain the length scale. The results are shown in table 7.10. The data at 0 degrees indicate that the extent of turbulent structures in

θ	ℓ/D_j
0	0.50161
45	0.37032
90	0.10422

Table 7.10: Turbulent length scales

this direction are approximately a half of one jet diameter. The smaller length scales

obtained from the 45 and 90 degree data are caused by the relatively large region of negative correlation coefficients for this data. This effect was also noted by Chu [73].

Two Point Space-Time Correlations

Plots of the two point space-time correlations for each separation are shown in figure 7.4.5. For each separation there is a delay time where the signals are clearly correlated (a distinct peak in the correlation curve). This delay time increases with increasing separation distance.

The exact location of the maximum correlation coefficient cannot be determined from the discrete data obtained in the analysis. To find this location, the correlation data was again curve fit with a polynomial (equation (7.19)). The maximum in the curve is found by differentiating the polynomial equation. The location of the peak in the correlation curves corresponds to the time required for a signal at the upstream point to convect to the downstream point. The resulting convection speed. U_c, (equation (7.14)) is shown in figure 7.44. The convection speed decreases slightly with increasing separation distance due to viscous effects. An average of the computed convection speeds is $0.6260U_j$ which is consistent with the results of Chu [73].

sep.	c_0	c_1	c_2	c_3	c_4	c_5	c_6	l_2 norm
				coefficient				
0 degrees								
1	0.9517	0.5115	-1.585	0.4060	0.5007	-0.3738	0.07827	$9.673 \cdot 10^{-6}$
2	0.8214	0.8444	-1.224	-0.04053	0.3132	-0.06564	-0.004293	$1.296 \cdot 10^{-4}$
3	0.6650	0.7884	-0.04775	-1.256	0.7415	-0.1015	-0.009149	$1.333 \cdot 10^{-4}$
4	0.5054	0.6288	0.7048	-1.583	0.6886	-0.07523	-0.005351	$2.419 \cdot 10^{-4}$
5	0.3478	0.4978	0.9339	-1.208	0.2545	0.06518	-0.01998	$2.083 \cdot 10^{-4}$
6	0.2043	0.3583	1.027	-0.9395	0.1094	0.06236	-0.01272	$6.915 \cdot 10^{-4}$
7	0.07140	0.4665	0.06638	0.6771	-0.8747	0.3248	-0.03882	$1.119 \cdot 10^{-4}$
8	0.005264	-0.01440	1.018	-0.3707	-0.1664	0.09207	-0.01089	$2.219 \cdot 10^{-3}$
45 degrees								
1	0.9332	0.6871	-2.083	0.5811	0.7198	-0.5646	0.1216	$2.791 \cdot 10^{-5}$
2	0.7569	1.148	-1.619	-0.06277	0.5037	-0.1413	0.003079	$3.132 \cdot 10^{-4}$
3	0.5481	1.097	-0.1815	-1.449	0.8416	-0.07731	-0.02293	$5.145 \cdot 10^{-4}$
4	0.3468	0.8275	0.9012	-1.943	0.7837	-0.04498	-0.01681	$1.168 \cdot 10^{-3}$
5	0.1574	0.5952	1.208	-1.316	0.04382	0.2163	-0.04732	$5.548 \cdot 10^{-4}$
6	-0.003487	0.3590	1.333	-0.9435	-0.1417	0.1981	-0.03372	$1.312 \cdot 10^{-3}$
7	-0.1408	-0.4605	0.1026	1.045	-1.271	0.4671	-0.05632	$6.762 \cdot 10^{-4}$
8	-0.1878	0.2468	-0.3164	1.754	-1.508	0.4642	-0.04896	$3.617 \cdot 10^{-3}$
90 degrees								
1	0.8634	1.365	-4.007	1.197	1.654	-1.234	0.2449	$1.173 \cdot 10^{-4}$
2	0.5451	1.661	-0.3637	-6.358	7.044	-2.941	0.4417	$2.954 \cdot 10^{-4}$
3	0.2079	1.348	2.144	-6.379	4.328	-1.096	0.08009	$1.018 \cdot 10^{-3}$
4	0.05870	0.6330	3.639	-5.640	2.585	-0.3642	-0.007533	$3.972 \cdot 10^{-3}$
5	-0.2577	0.3414	2.409	-1.468	-0.9120	0.7960	-0.1435	$3.272 \cdot 10^{-3}$
6	-0.3373	-0.2450	2.282	-0.4172	-1.284	0.6962	-0.1013	$5.808 \cdot 10^{-3}$
7	-0.3705	-0.07766	-0.1704	3.000	-2.931	0.9961	-0.1147	$6.802 \cdot 10^{-3}$
8	-0.3132	0.03557	-2.236	5.467	-3.921	1.129	-0.1155	$1.882 \cdot 10^{-2}$

Table 7.11: Curve fit coefficients for two point space-time correlations
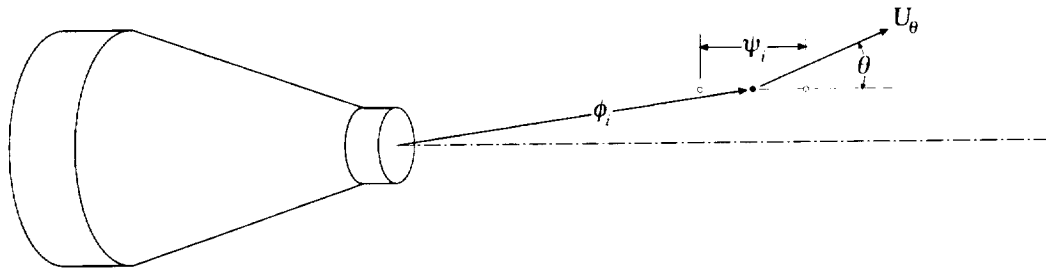
Figure 7.1: Two point correlation schematic
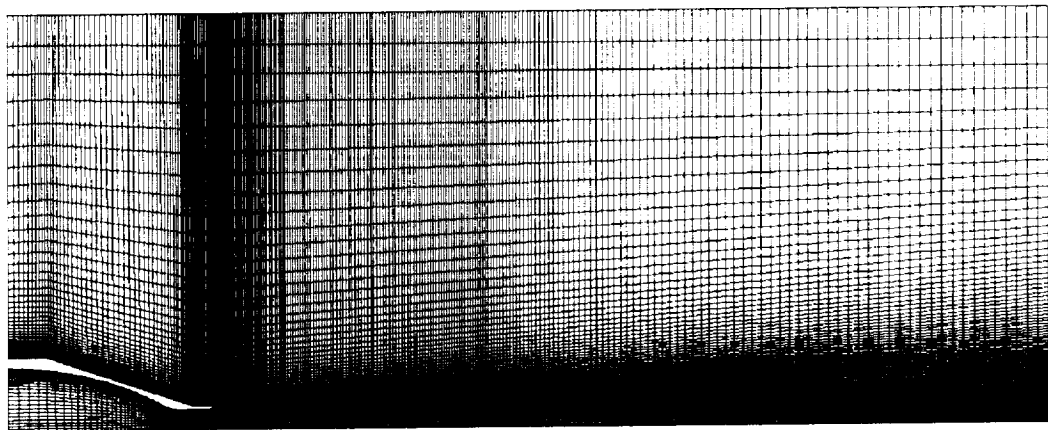
Figure 7.2: Axisymmetric computational grid
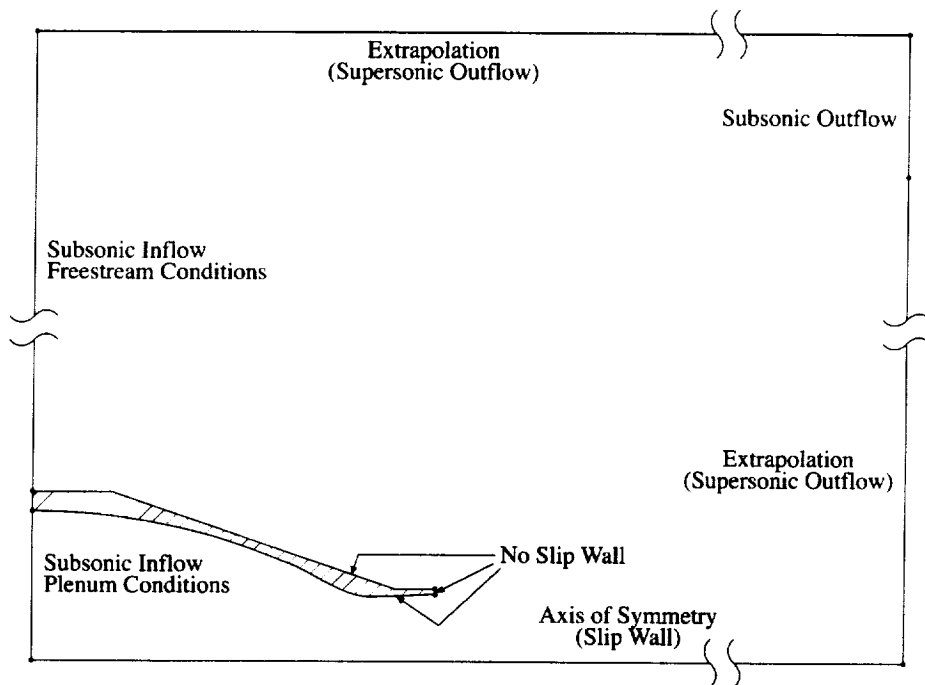
Figure 7.3: Boundary conditions for axisymmetric calculations
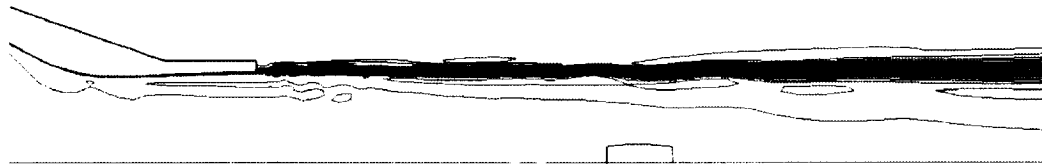
(a) Coarse grid
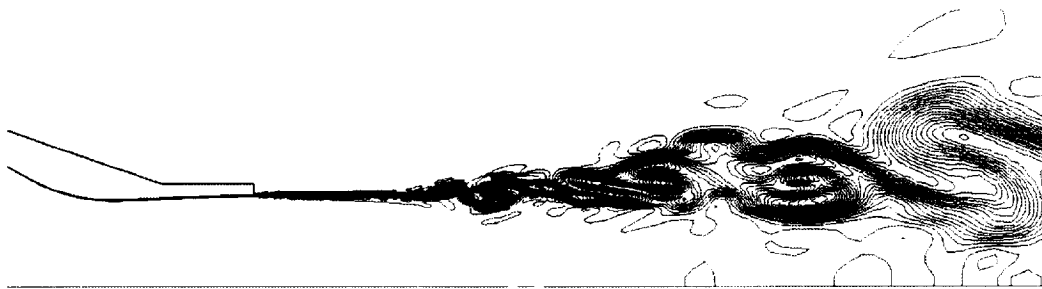
(b) Medium grid

(c) Fine grid

Figure 7.4: Entropy contours for axisymmetric grid study
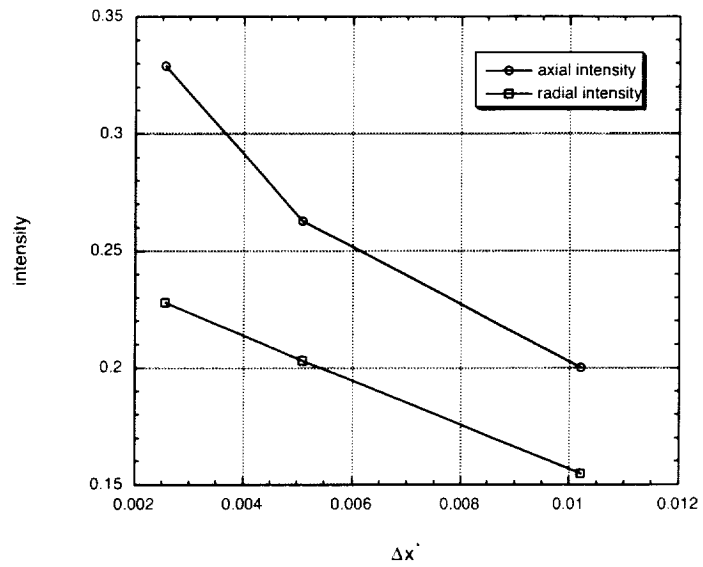
(a) Turbulent intensities
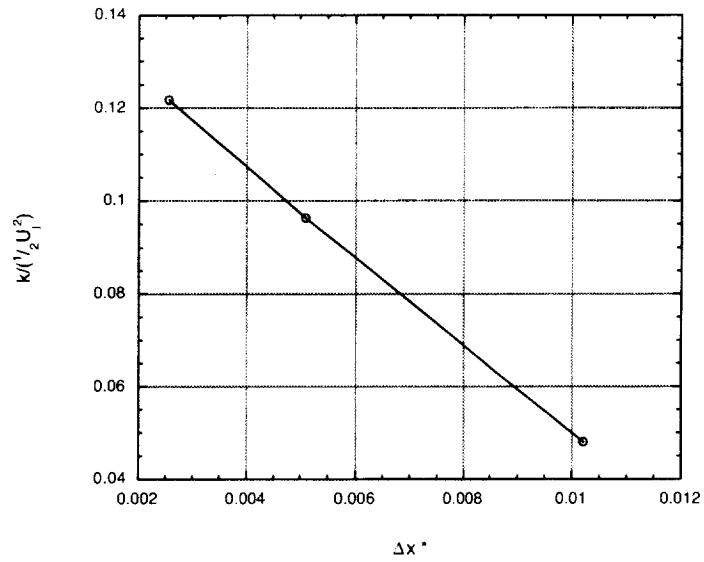
(b) Turbulent kinetic energy

Figure 7.5: Turbulent statistics for axisymmetric grid study
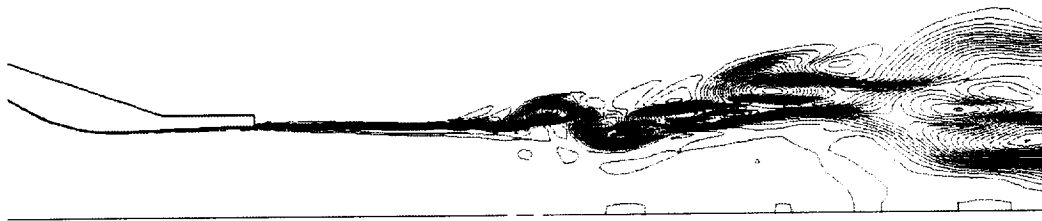
(a) Gottlieb-Turkel
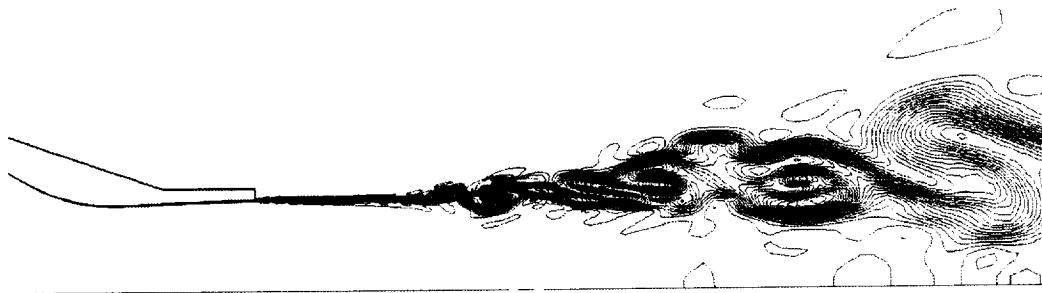
(b) Runge-Kutta

Figure 7.6: Entropy contours for axisymmetric scheme comparison
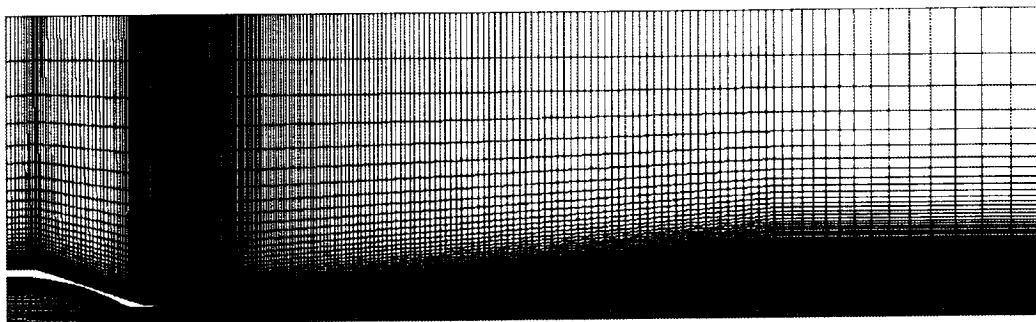
Figure 7.7: Axisymmetric computational grid with exit zone

(a) with exit zone
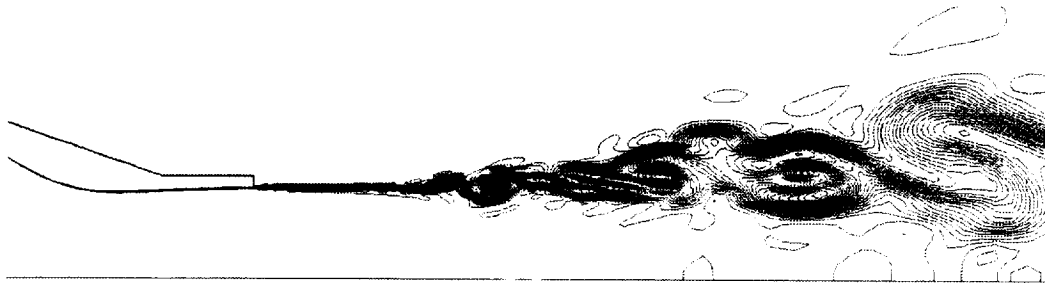
(b) without exit zone

Figure 7.8: Entropy contours for exit zone boundary condition comparison

(a) without sub-grid model
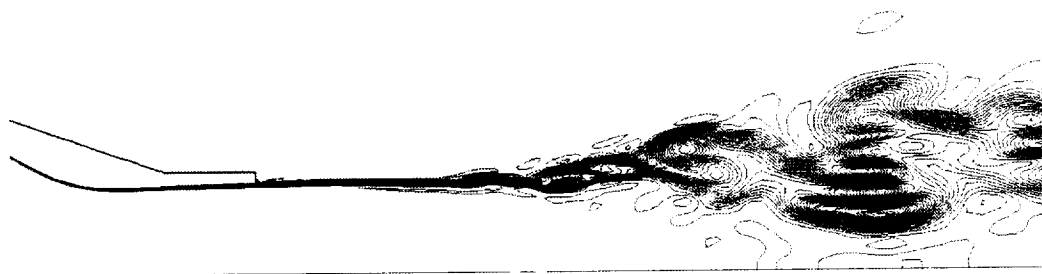
(b) with sub-grid model

Figure 7.9: Entropy contours showing effect of the sub-grid model

(a) instantaneous

(b) time averaged

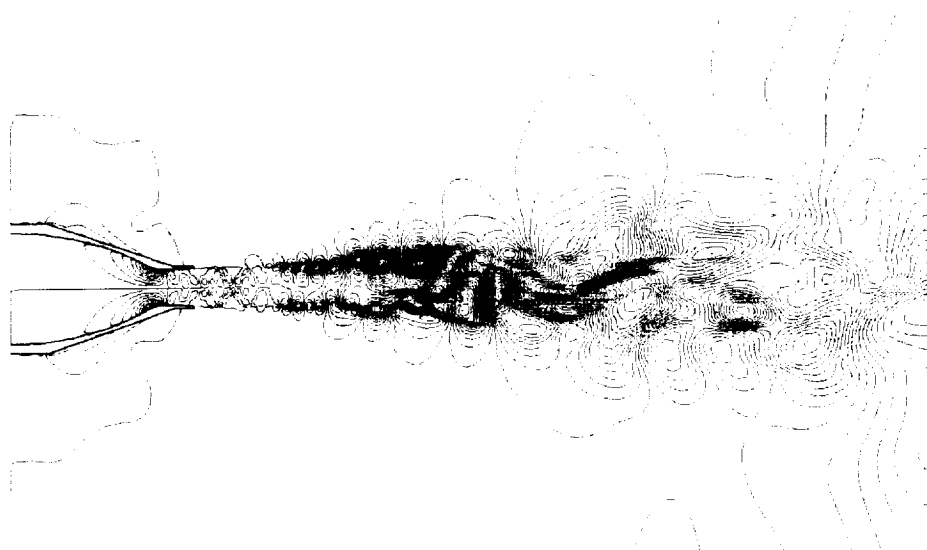Figure 7.10: Density contours for the axisymmetric solution
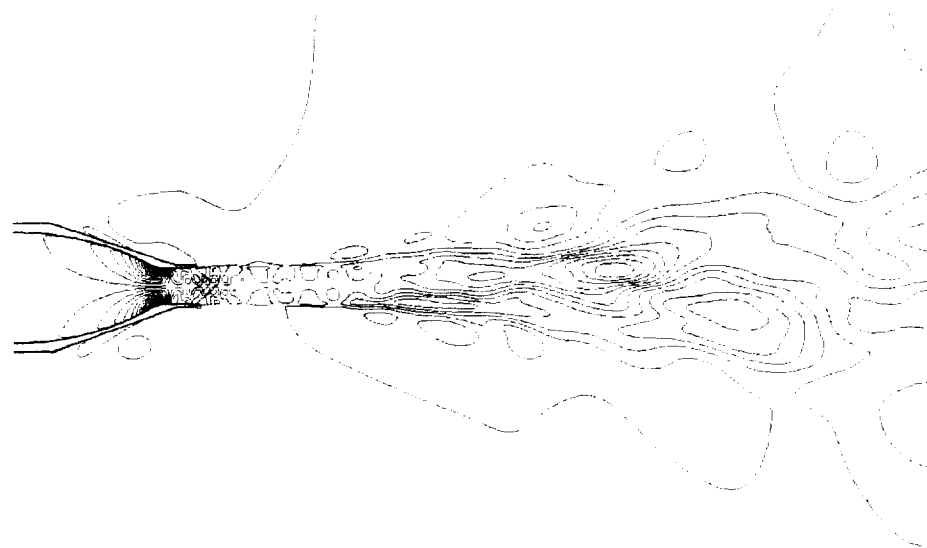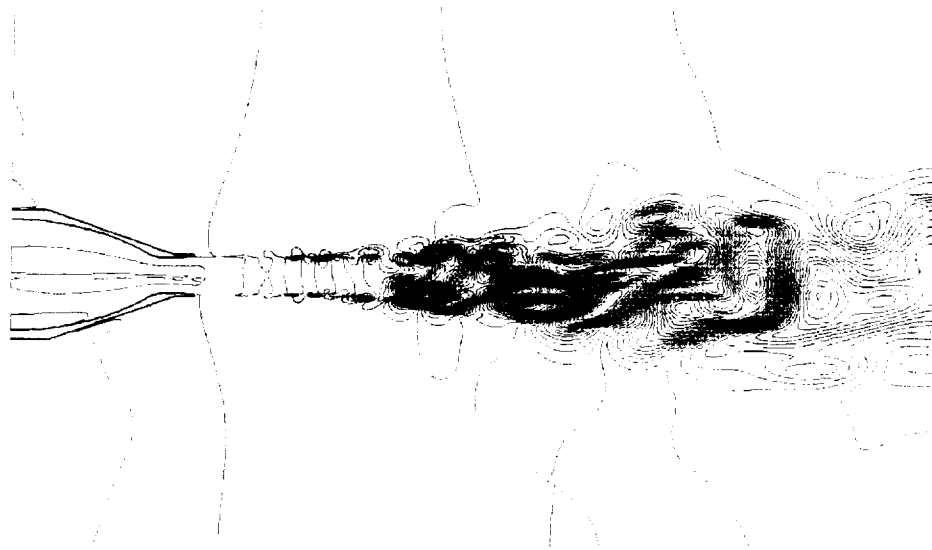

(a) instantaneous

(b) time averaged

Figure 7.11: Axial velocity contours for the axisymmetric solution
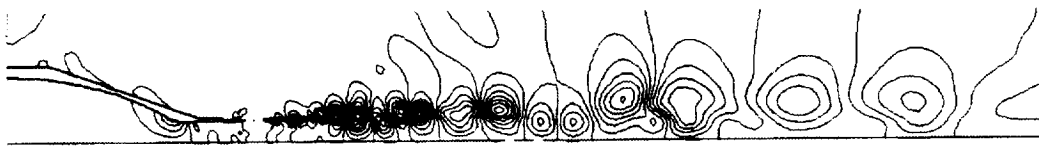
(a) instantaneous
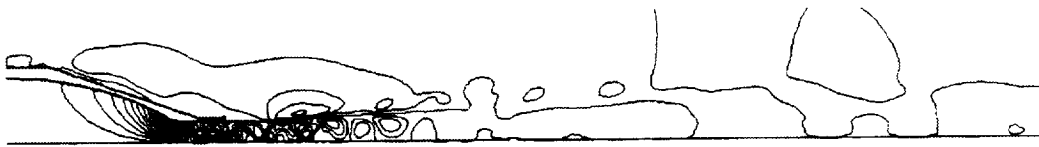
(b) time averaged

Figure 7.12: Radial velocity contours for the axisymmetric solution
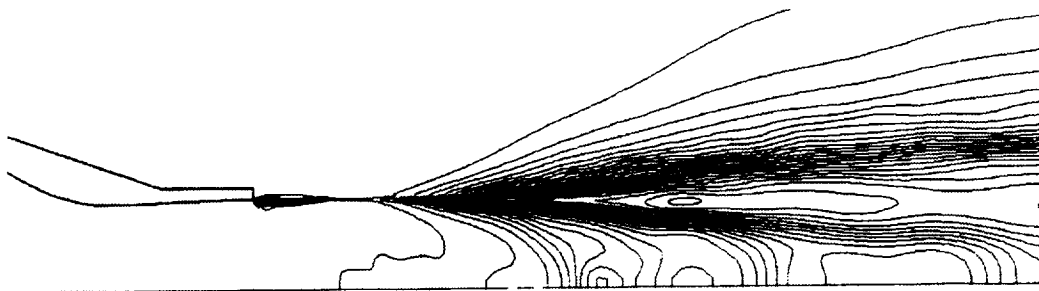
(a) entire domain

(b) detail of nozzle exit

Figure 7.13: Root mean square density contours for the axisymmetric solution
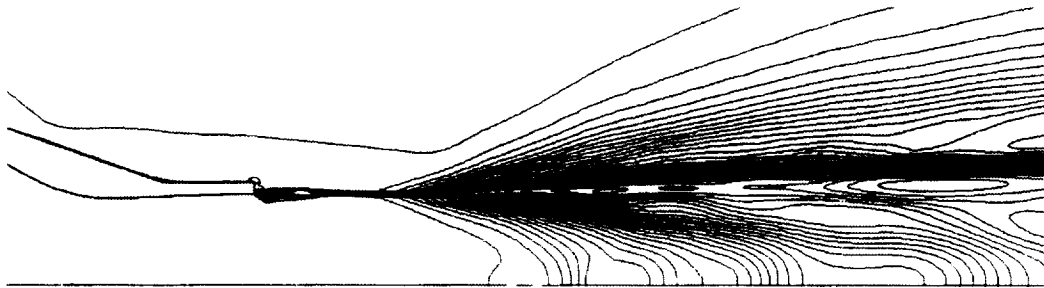
(a) entire domain

(b) detail of nozzle exit

Figure 7.14: Root mean square axial velocity contours for the axisymmetric solution
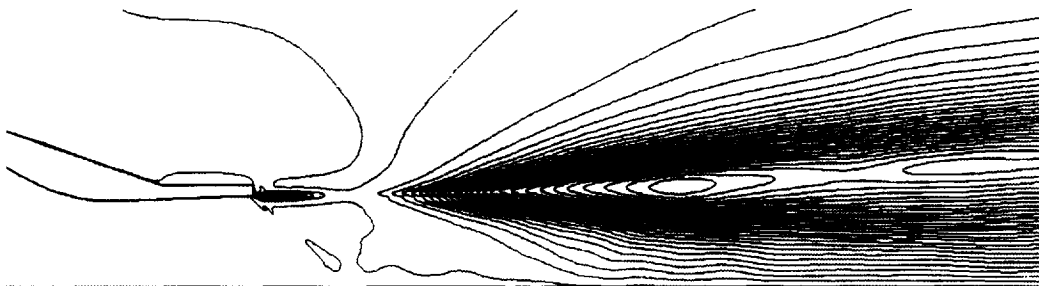
(a) entire domain

(b) detail of nozzle exit

Figure 7.15: Root mean square radial velocity contours for the axisymmetric solution
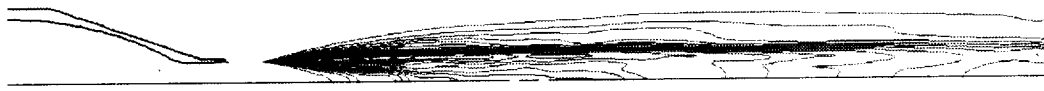
(a) entire domain
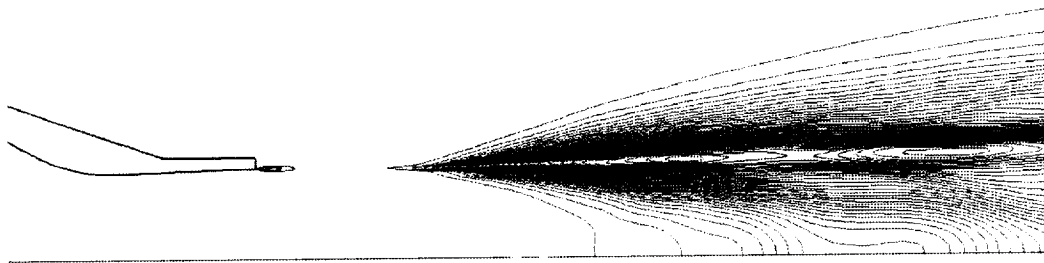
(b) detail of nozzle exit

Figure 7.16: Turbulent kinetic energy contours for the axisymmetric solution
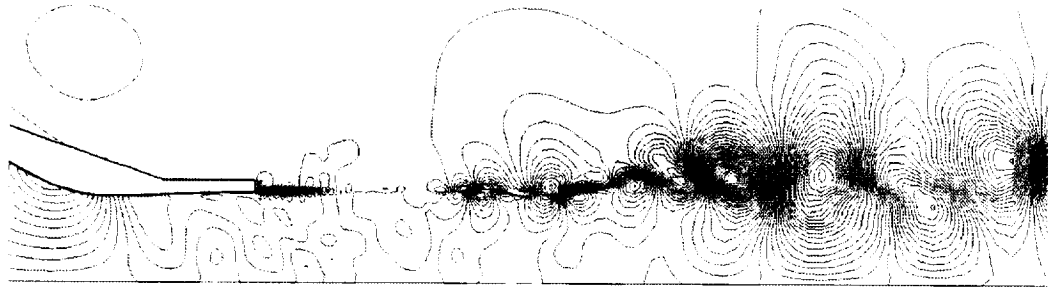
(a) instantaneous radial velocity
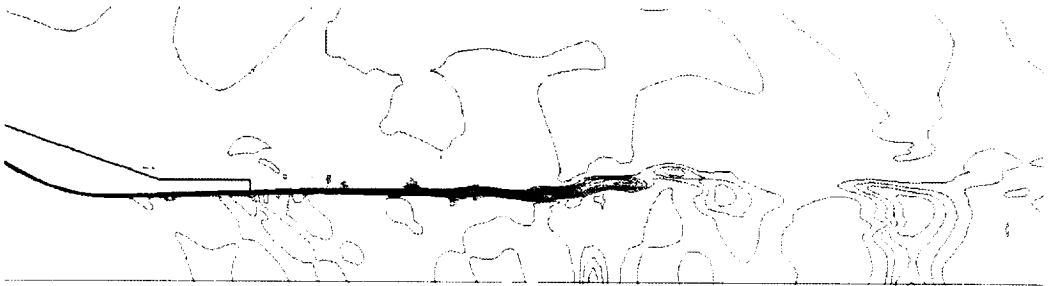
(b) sub-grid turbulent kinetic energy

Figure 7.17: Nozzle exit detail for axisymmetric solution
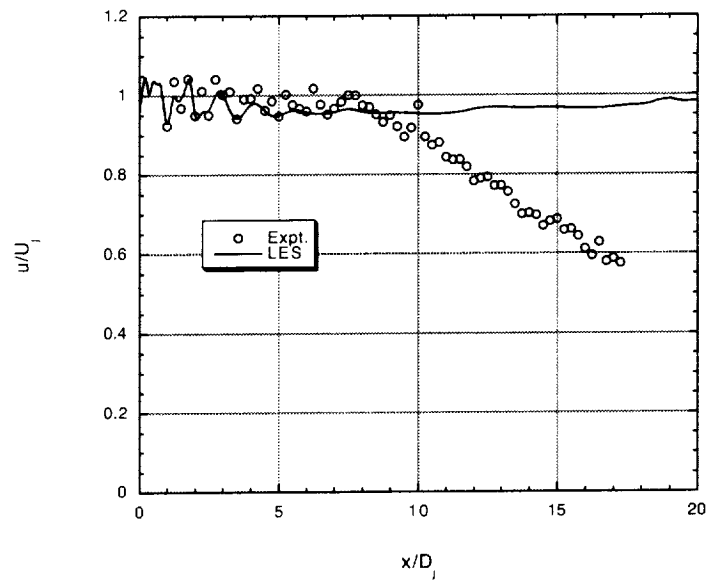
Figure 7.18: Time averaged centerline velocity profile for the axisymmetric LES solution
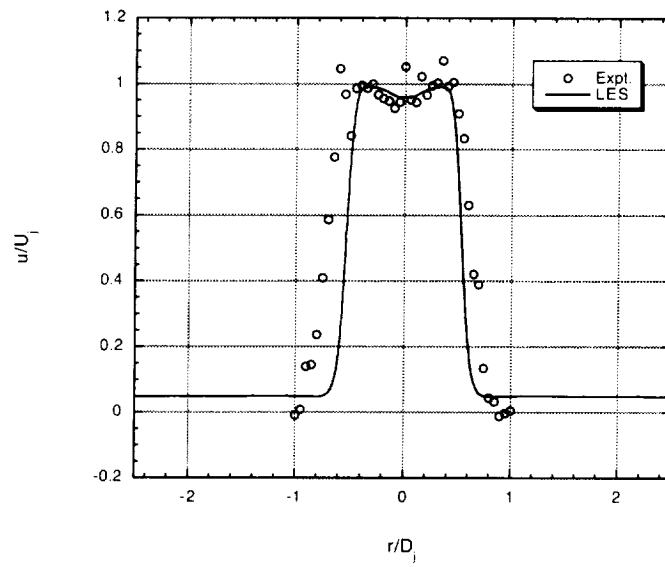
(a) $x/D_j = 2$
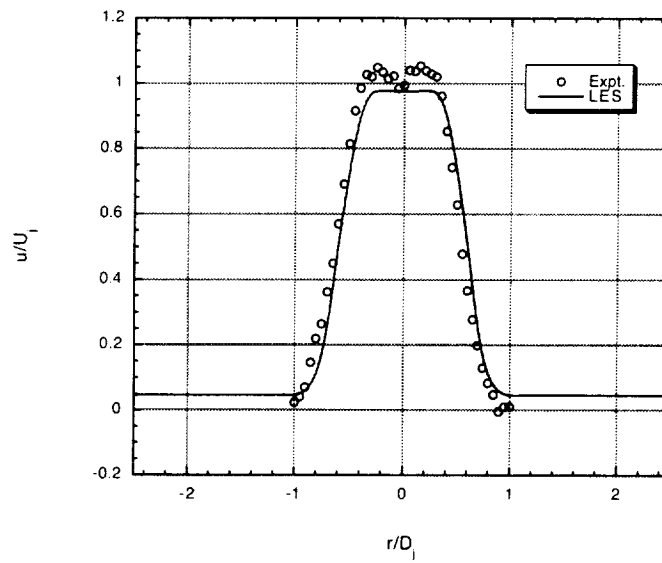
(b) $x/D_j = 4$

Figure 7.19: Time averaged radial profiles of axial velocity for the axisymmetric LES solution

Figure 7.19: continued

(c) $x/D_j = 6$
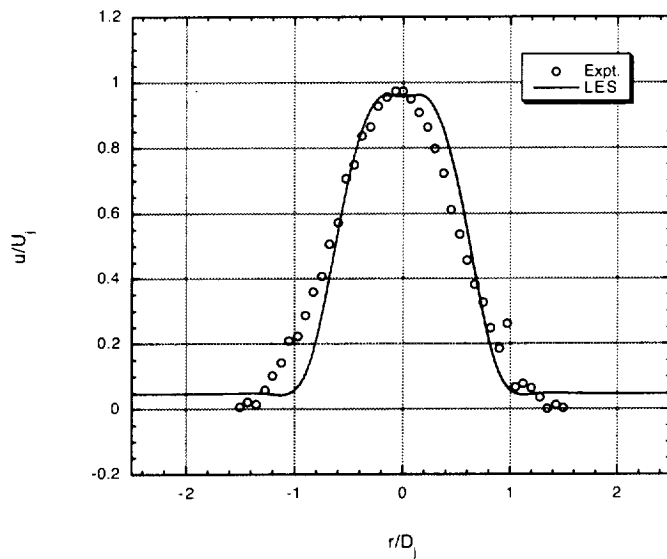
(d) $x/D_j = 8$

Figure 7.19: continued

(e) $x/D_j = 10$
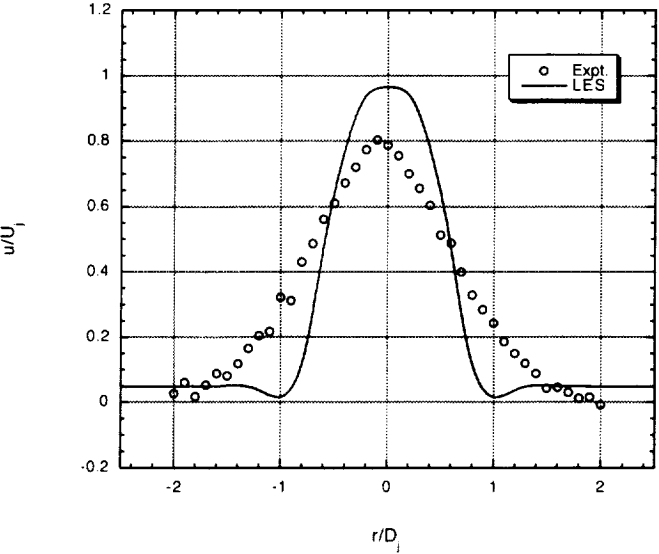
(f) $x/D_j = 12$
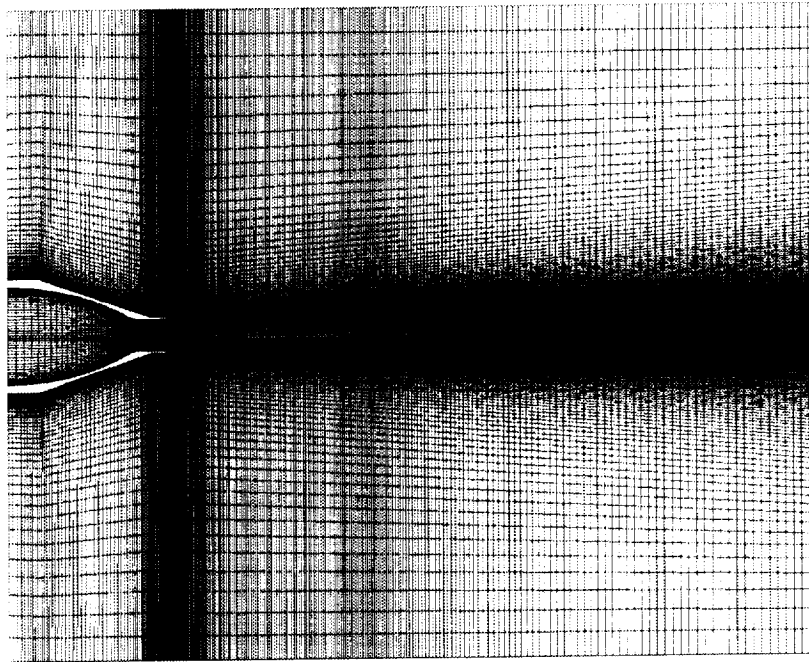
(a) streamwise, x-y plane
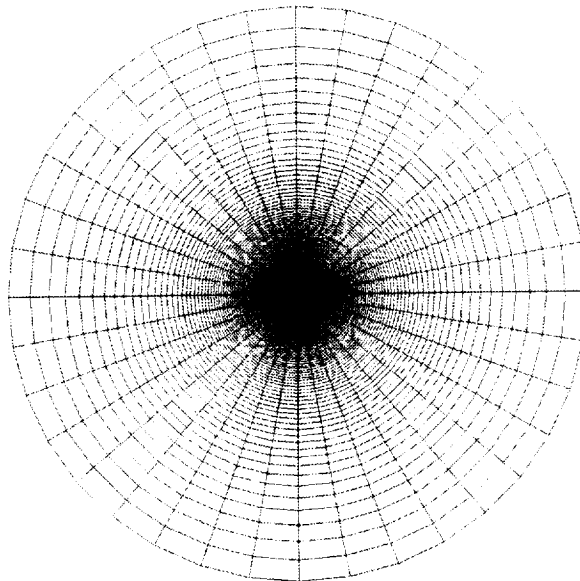
(b) crossstream, y-z plane at outflow boundary

Figure 7.20: Three-dimensional grid
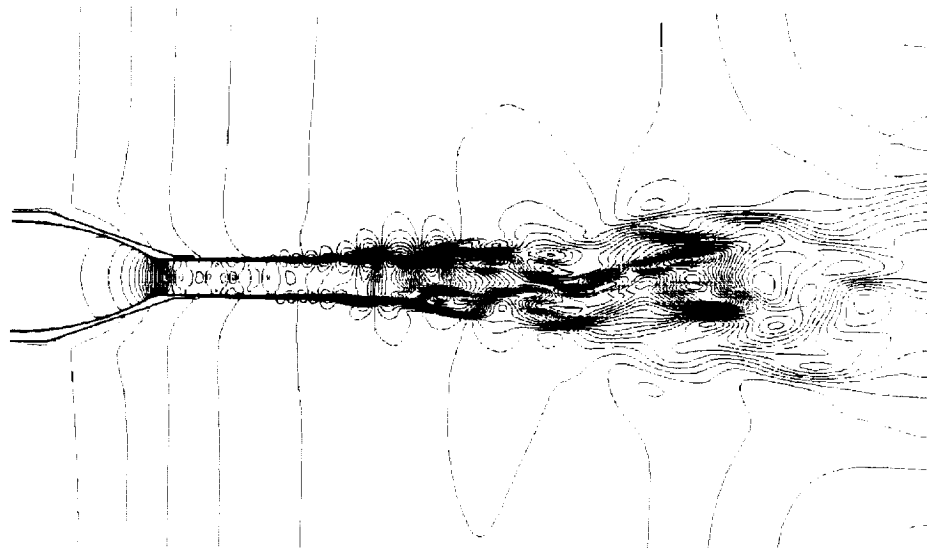
(a) instantaneous
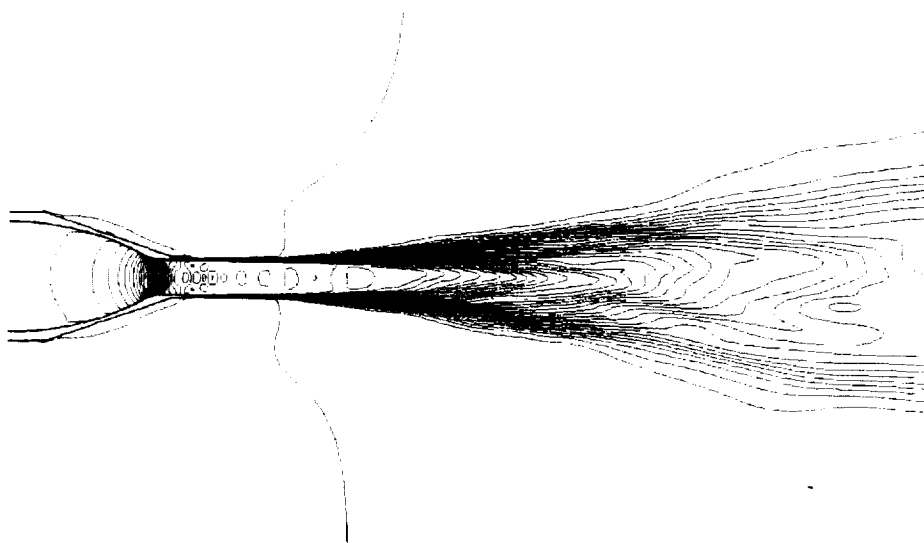
(b) time averaged

Figure 7.21: Axial velocity contours for 3D LES solution

(a) instantaneous

(b) time averaged

Figure 7.22: Radial velocity contours for 3D LES solution

(a) instantaneous
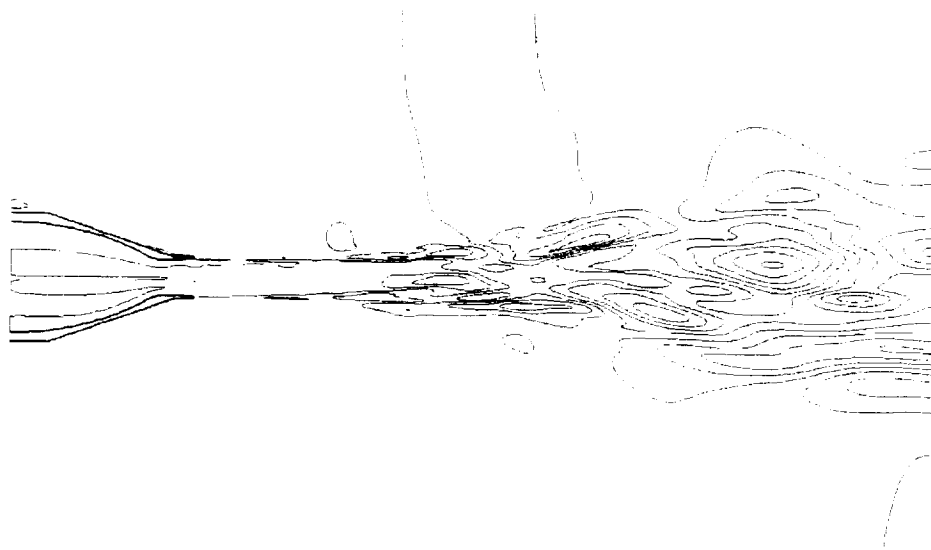
(b) time averaged

Figure 7.23: Azimuthal velocity contours for 3D LES solution

(a) instantaneous   (b) time averaged
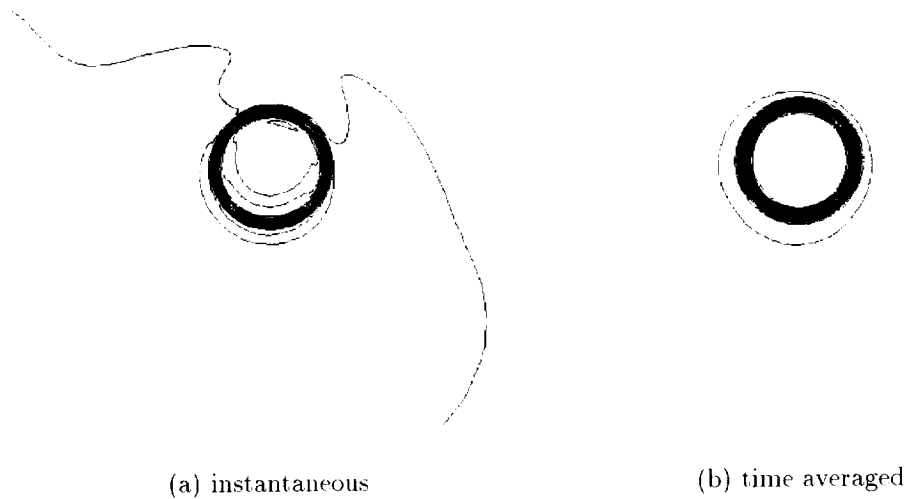
Figure 7.24: Total velocity contours at $x/D_j = 3$ for 3D LES solution

(a) instantaneous   (b) time averaged
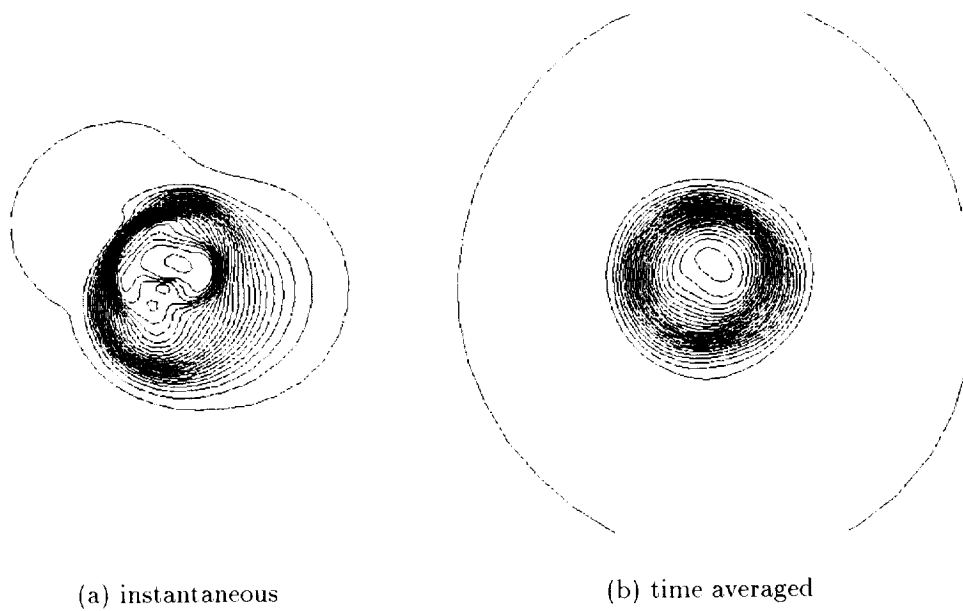
Figure 7.25: Total velocity contours at $x/D_j = 6$ for 3D LES solution

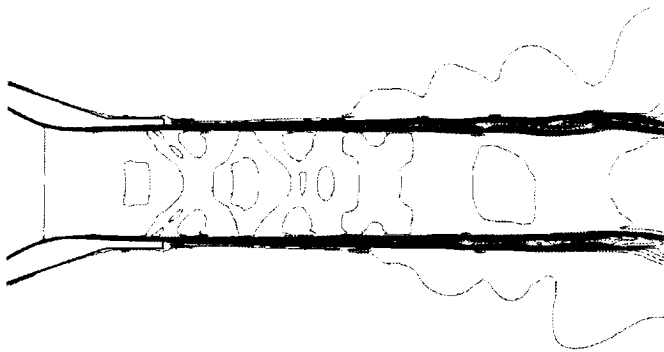(a) instantaneous   (b) time averaged
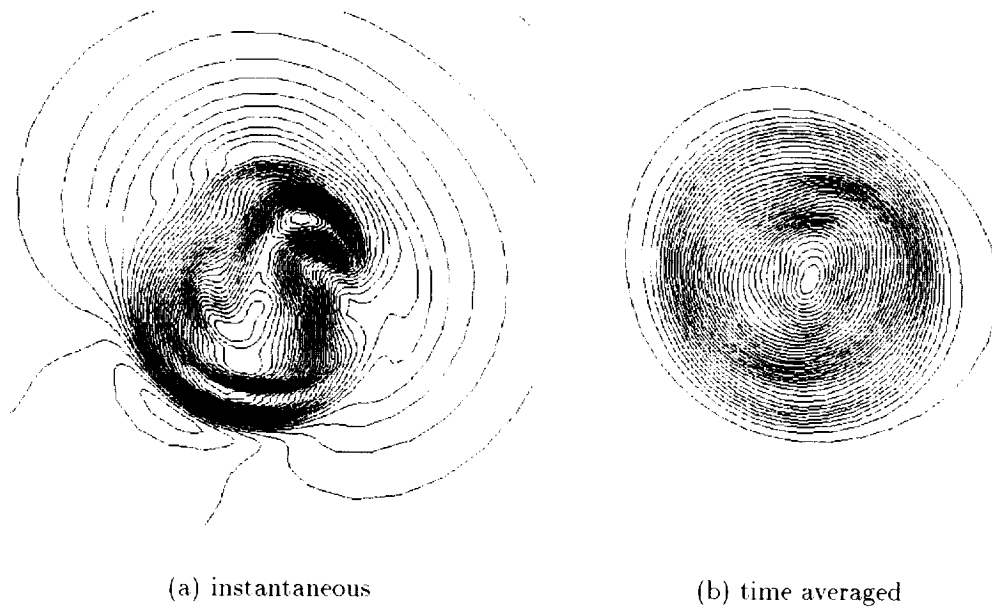
Figure 7.26: Total velocity contours at $x/D_j = 9$ for 3D LES solution
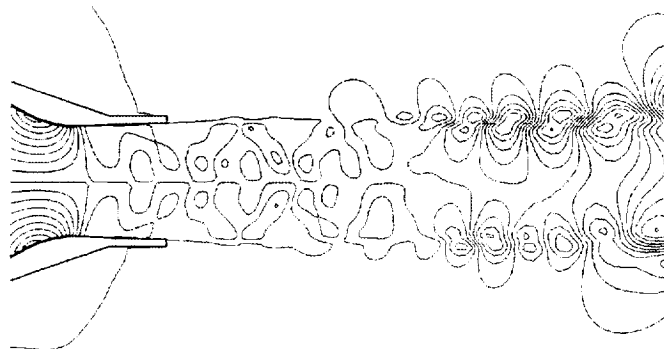
(a) radial velocity

(b) sub-grid turbulent kinetic energy

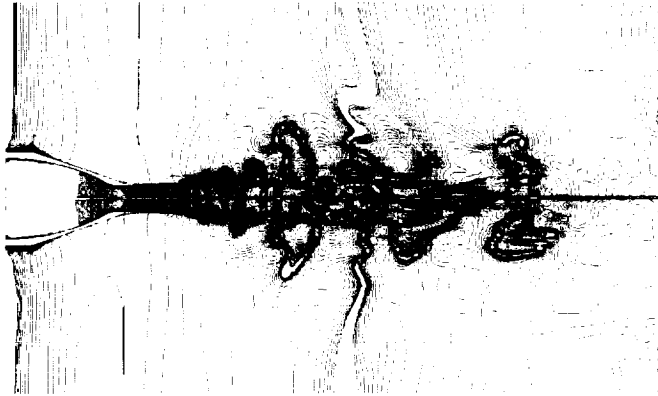Figure 7.27: Nozzle exit detail for 3D LES solution
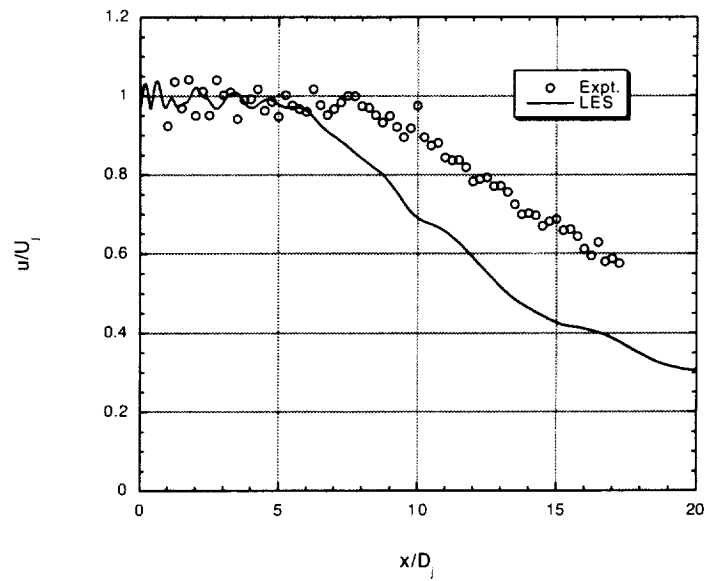
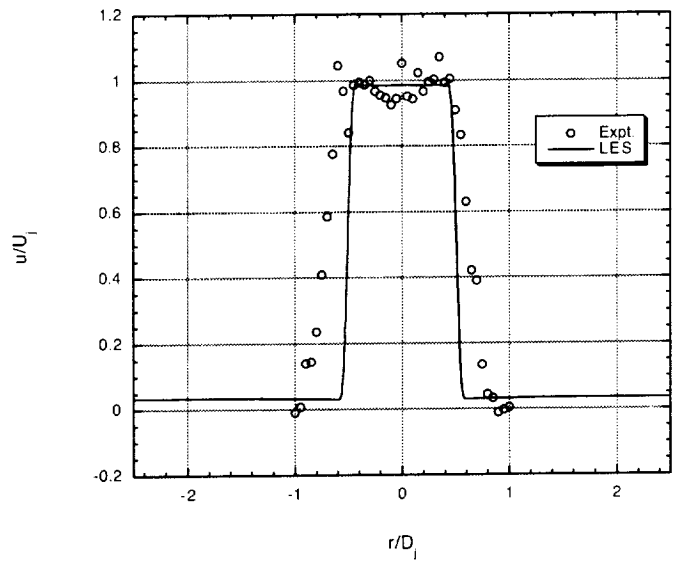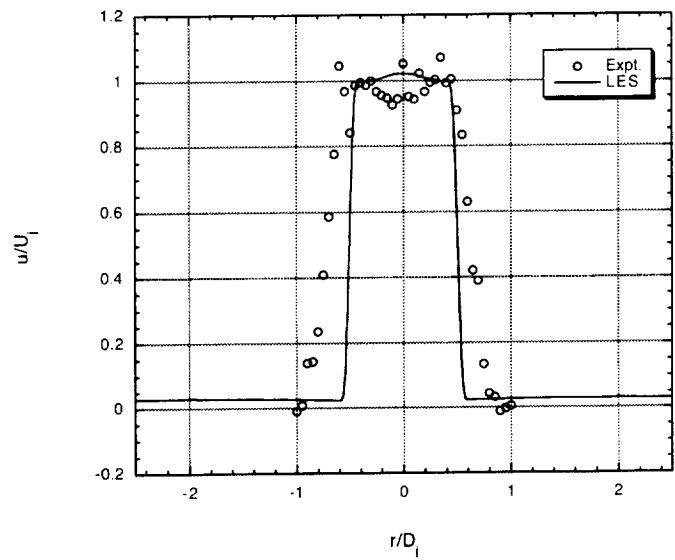Figure 7.28: Dilatation contours for 3D LES solution

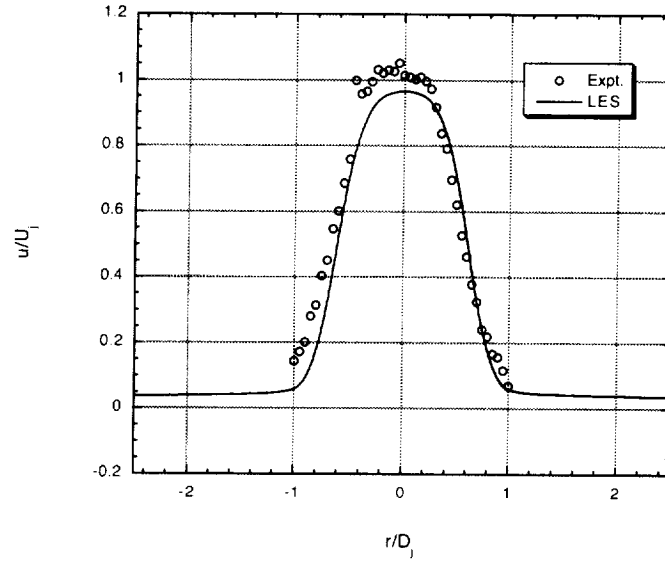Figure 7.29: Time averaged centerline velocity profile for the 3D LES solution

(a) $x/D_j = 2$

(b) $x/D_j = 4$

Figure 7.30: Time averaged radial profiles of axial velocity for the 3D LES solution

continued

Figure 7.30: continued

(c) $x/D_j = 6$

(d) $x/D_j = 8$

continued
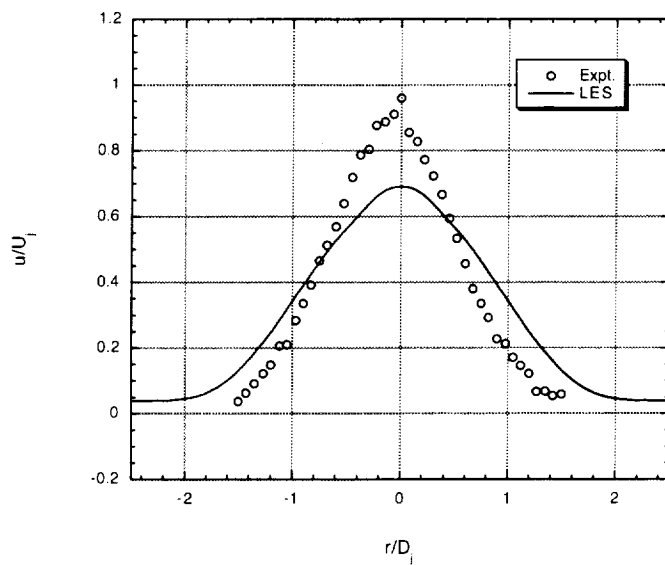
(e) $x/D_j = 10$
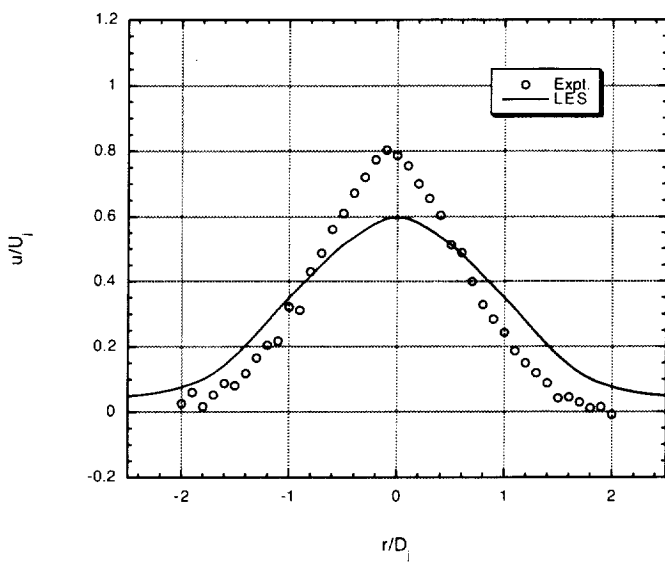
(f) $x/D_j = 12$
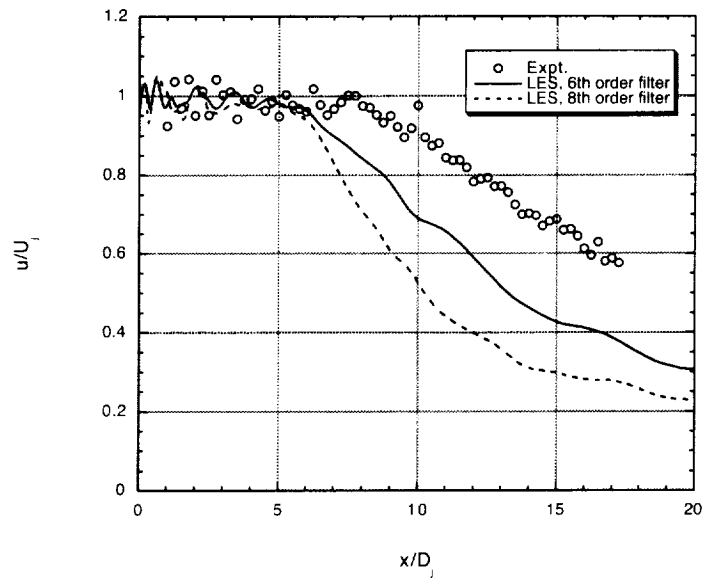
Figure 7.31: Comparison of sixth- and eighth- order filters on 3D LES solution
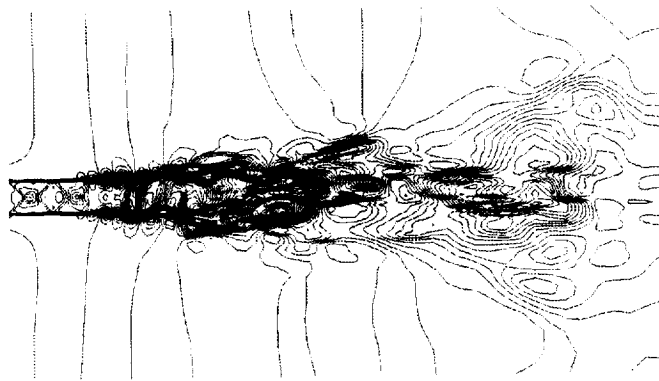
(a) $\frac{tD_j}{U_j} = 0.0000$
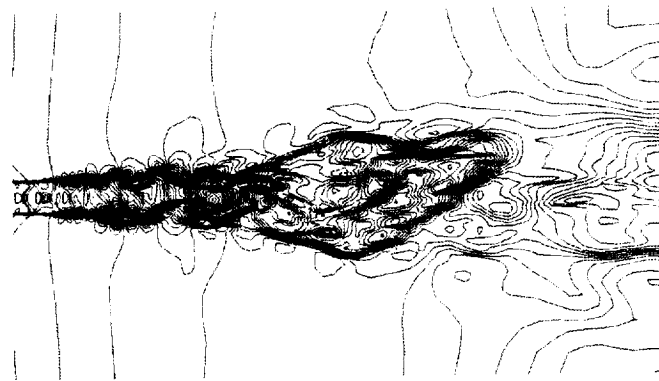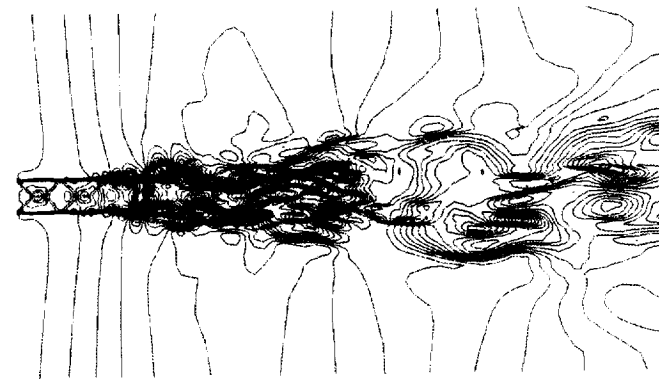
(b) $\frac{tD_j}{U_j} = 16.149$

(c) $\frac{tD_j}{U_j} = 32.297$

Figure 7.32: Instantaneous axial velocity contours for the 3D LES solution
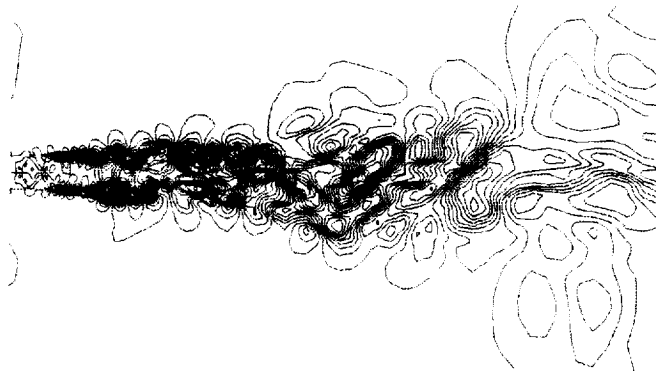
(a) $\frac{tD_j}{U_j} = 0.0000$
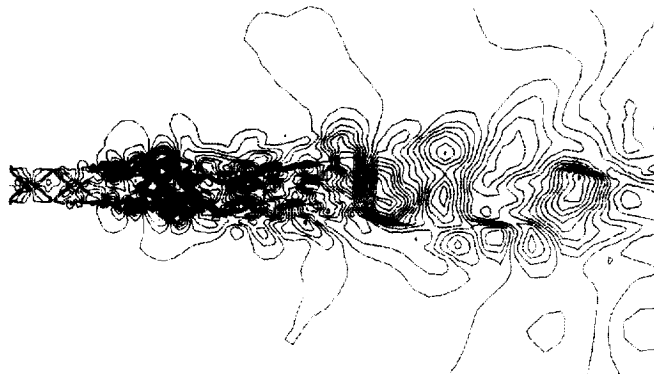
(b) $\frac{tD_j}{U_j} = 16.149$

(c) $\frac{tD_j}{U_j} = 32.297$

Figure 7.33: Instantaneous radial velocity contours for the 3D LES solution
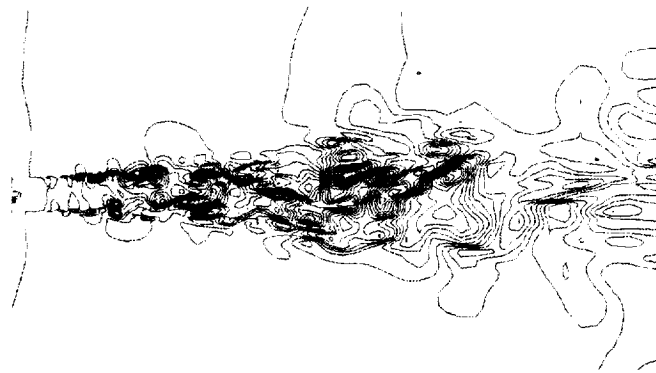
(a) $\frac{tD_j}{U_j} = 0.0000$
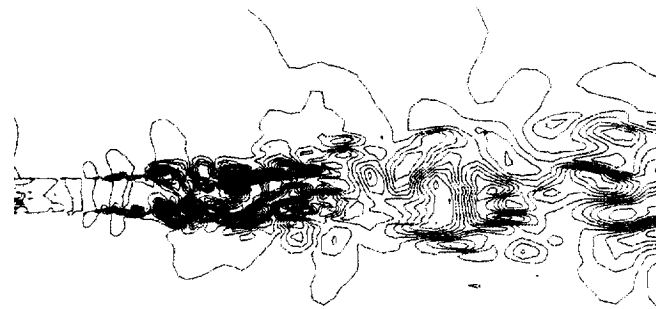
(b) $\frac{tD_j}{U_j} = 16.149$

(c) $\frac{tD_j}{U_j} = 32.297$

Figure 7.34: Instantaneous azimuthal velocity contours for the 3D LES solution

(a) $\frac{tD_j}{U_j} = 0.0000$

(b) $\frac{tD_j}{U_j} = 16.149$
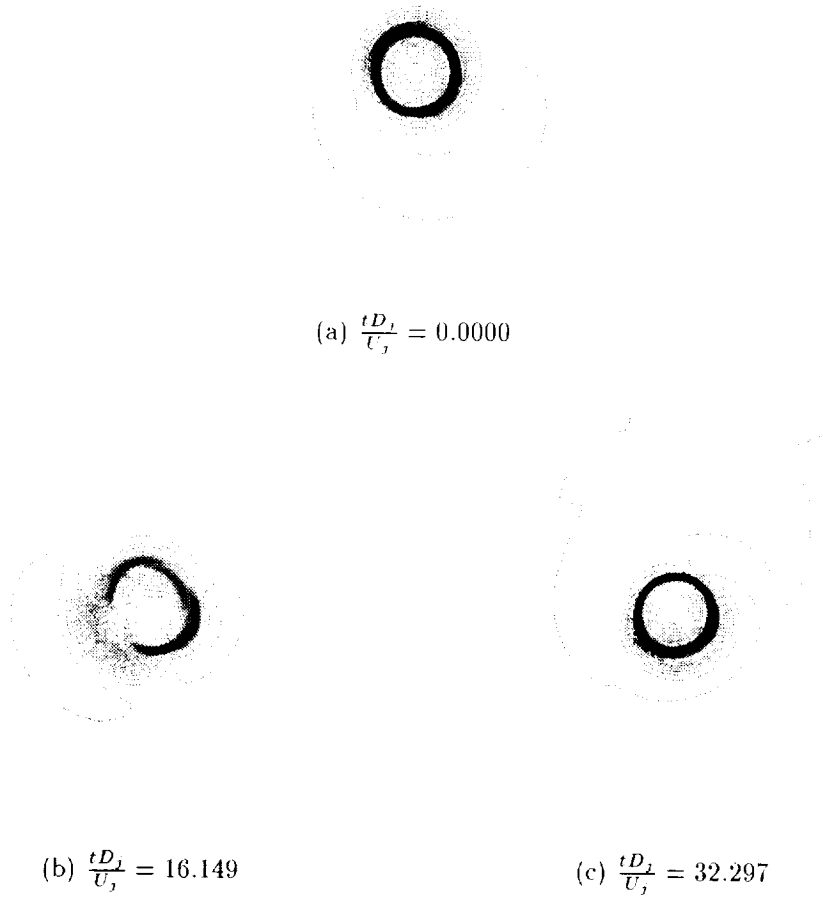
(c) $\frac{tD_j}{U_j} = 32.297$

Figure 7.35: Instantaneous total velocity contours at $x/D_j = 3$ for the 3D LES solution
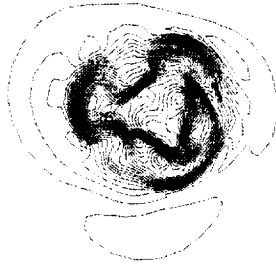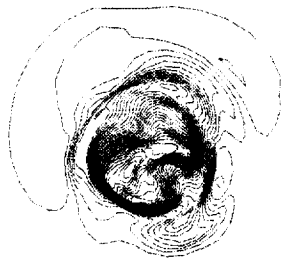
(a) $\frac{tD_j}{U_j} = 0.0000$

(b) $\frac{tD_j}{U_j} = 16.149$

(c) $\frac{tD_j}{U_j} = 32.297$

Figure 7.36: Instantaneous total velocity contours at $x/D_j = 6$ for the 3D LES solution
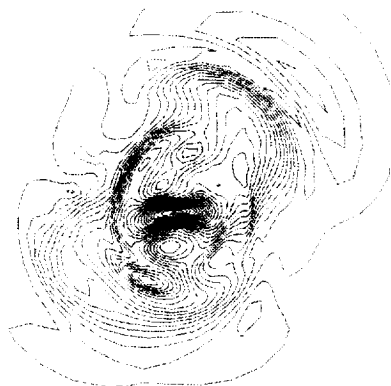
(a) $\frac{tD_j}{U_j} = 0.0000$
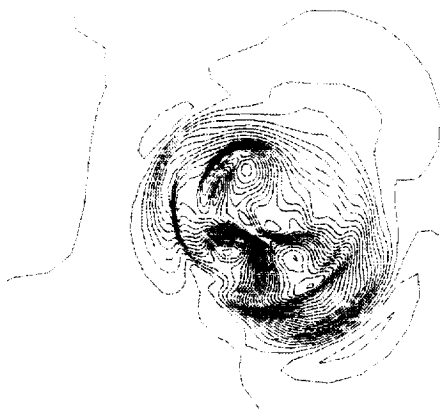
(b) $\frac{tD_j}{U_j} = 16.149$
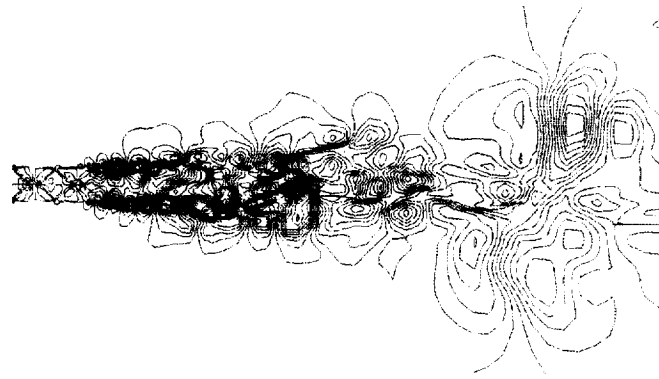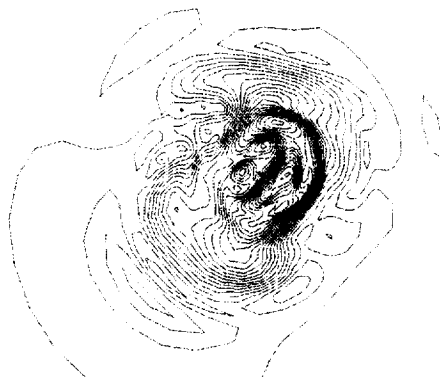
(c) $\frac{tD_j}{U_j} = 32.2970$

Figure 7.37: Instantaneous total velocity contours at $x/D_j = 9$ for the 3D LES solution
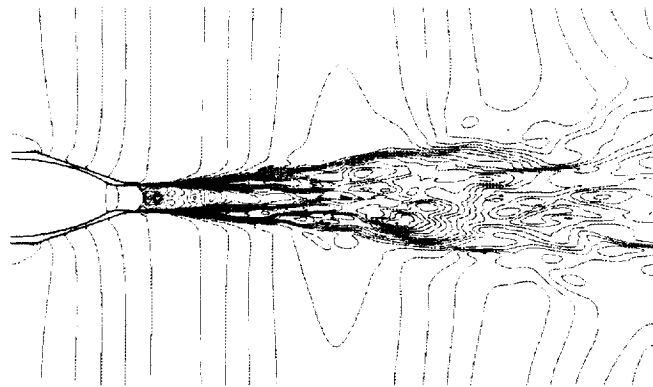
(a) axial turbulent intensity
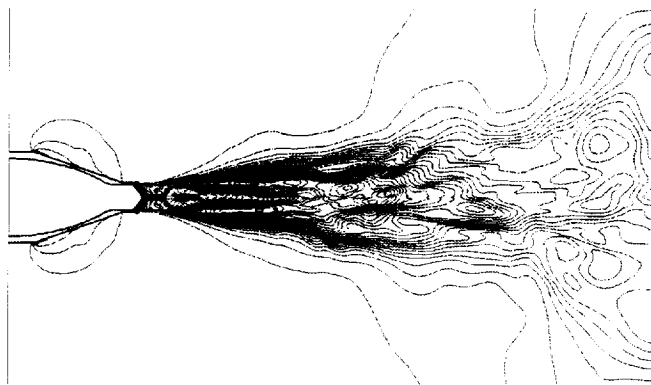
(b) radial turbulent intensity
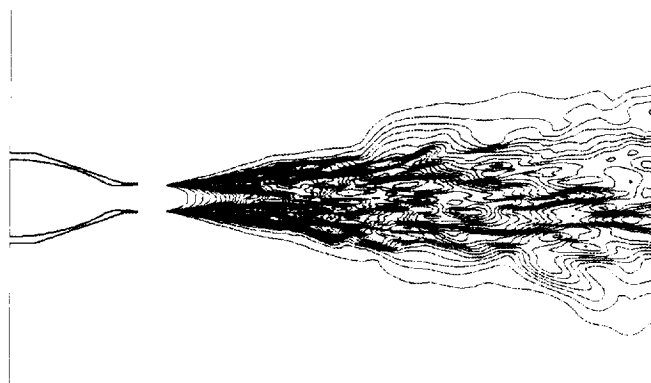
(c) azimuthal turbulent intensity

Figure 7.38: Turbulent intensity contours for the 3D LES solution
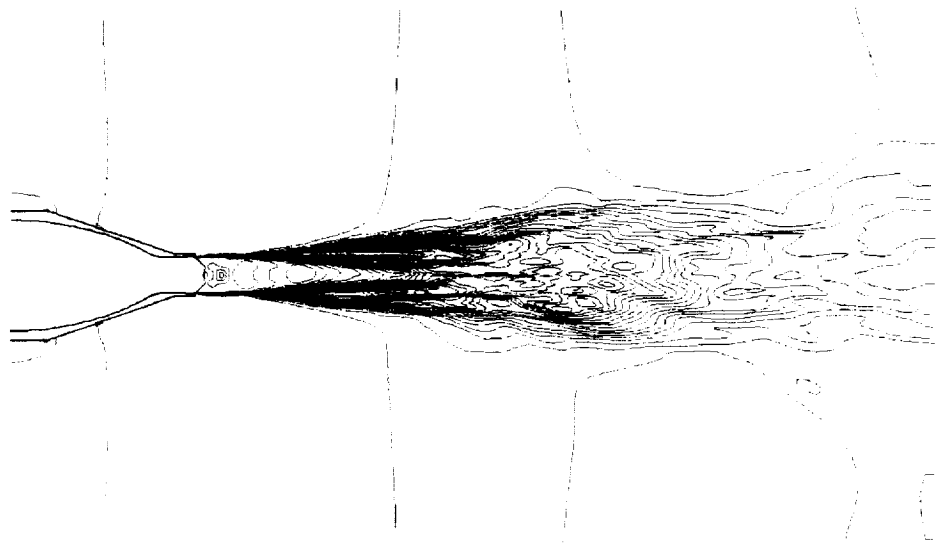
Figure 7.39: Turbulent kinetic energy contours for the 3D LES solution

(a) $\widehat{\widehat{u}}/\widehat{\widehat{v}} < 0.8$
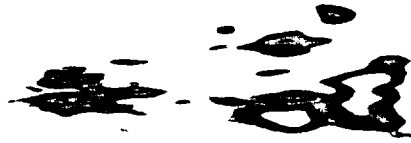
(b) $0.8 < \widehat{\widehat{u}}/\widehat{\widehat{v}} < 1.2$

(c) $\widehat{\widehat{u}}/\widehat{\widehat{v}} > 1.2$

Figure 7.40: Ratio of axial to radial turbulent intensity for the 3D LES solution
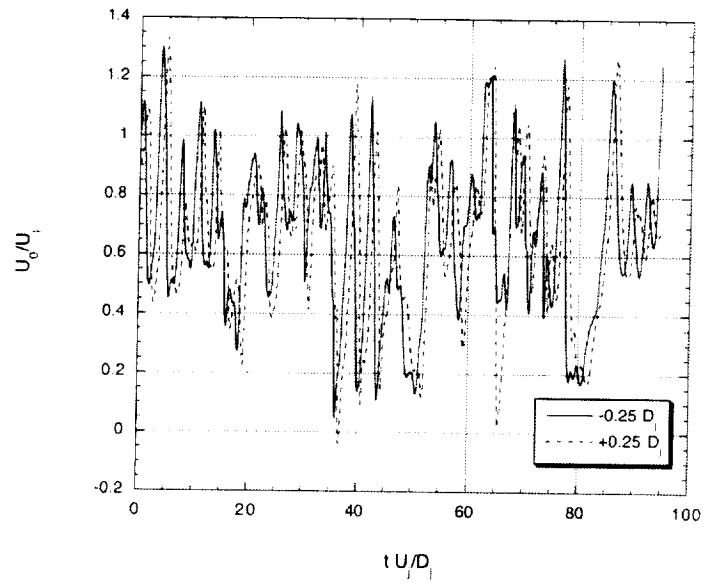
(a) 0 degrees
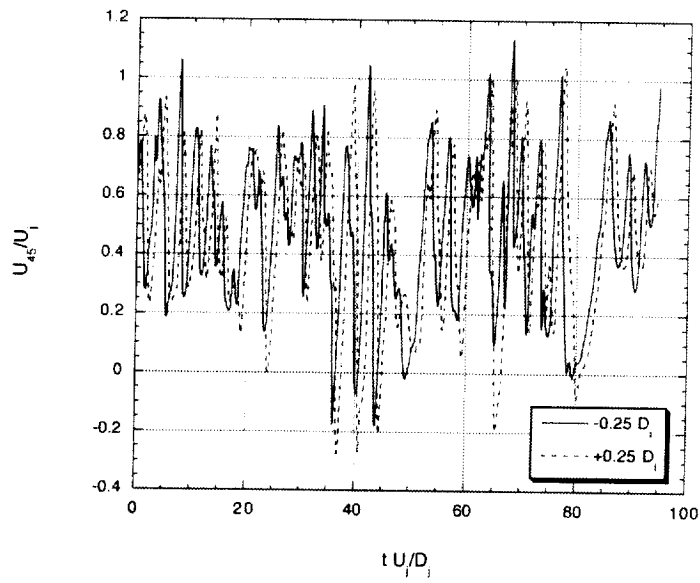
(b) 45 degrees

Figure 7.41: Velocity history for two point correlations

Figure 7.41: continued
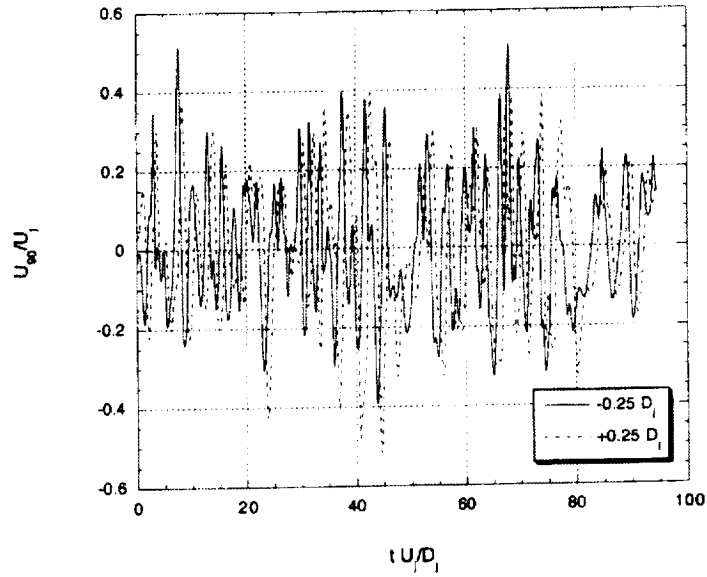
(c) 90 degrees
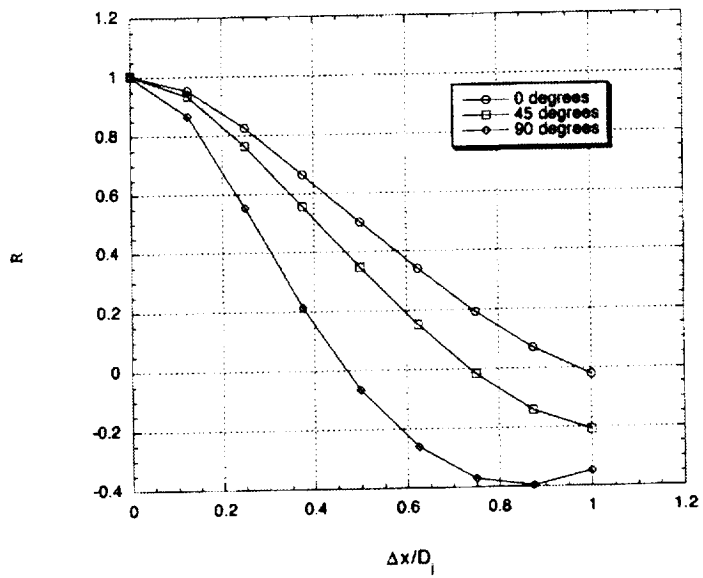
Figure 7.42: Two point space correlation coefficient
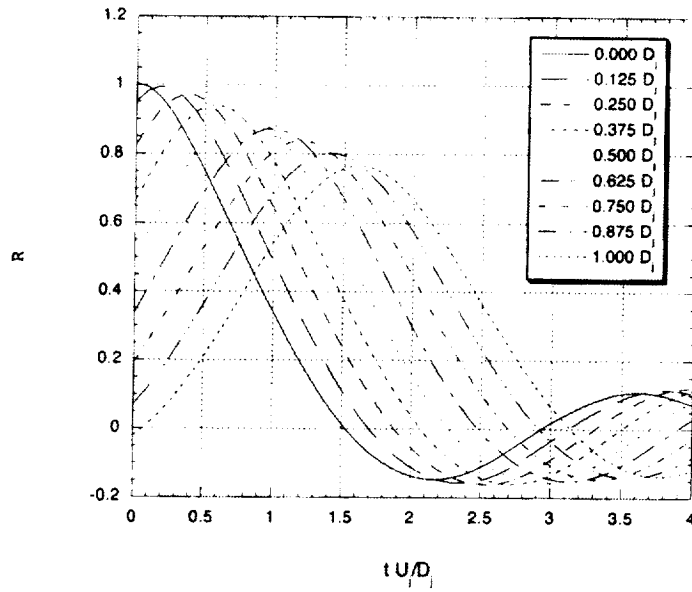
(a) 0 degrees
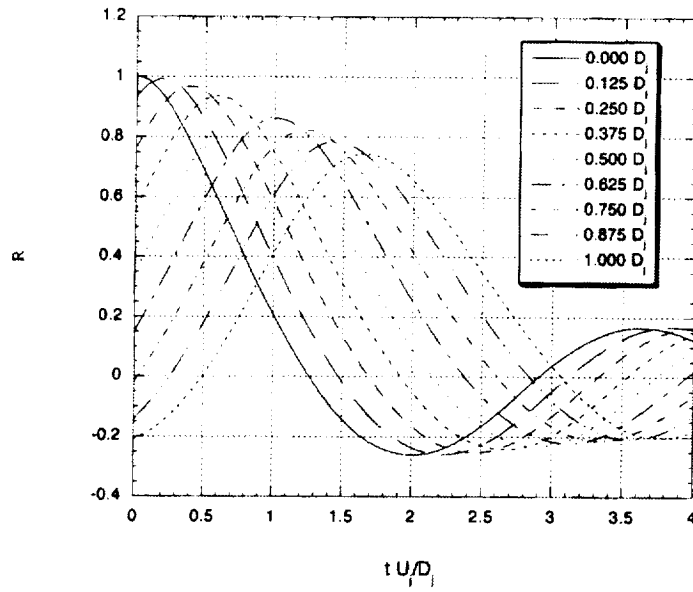
(b) 45 degrees

Figure 7.43: Two point space-time correlation coefficient

Figure 7.43: continued
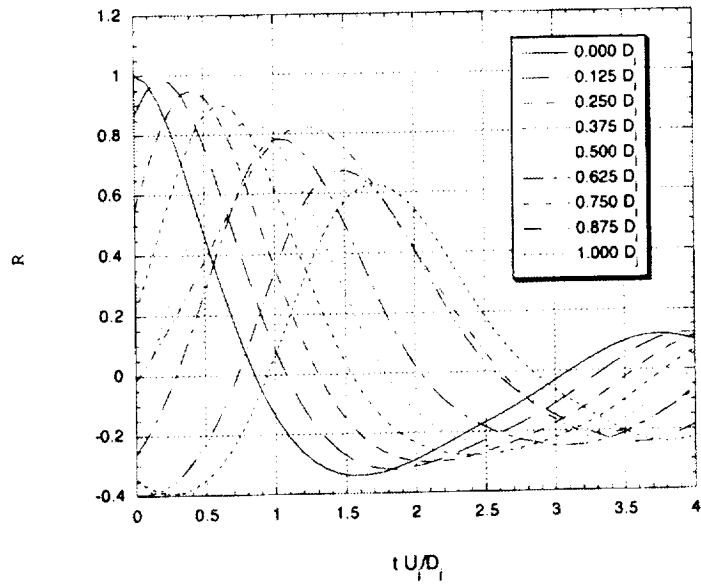
(c) 90 degrees
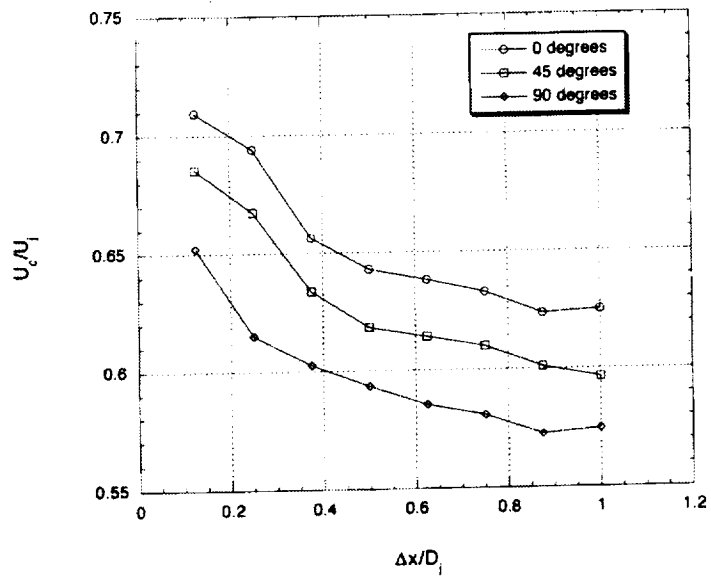
Figure 7.44: Convection velocity

CHAPTER 8

CONCLUSIONS AND RECOMMENDATIONS

A numerical method to simulate high Reynolds number jet flows was formulated and applied to gain a better understanding of the flow physics. Close attention is paid to the sources of error in such calculations and efforts were made to minimize them whenever possible.

Large-eddy simulation is chosen as the most promising approach to model the turbulent structures due to its compromise between accuracy and computational expense. The filtered Navier-Stokes equations are developed including a total energy form of the energy equation. Sub-grid scale models are adapted from compressible forms of Smagorinsky's original model.

The effect of using disparate temporal and spatial accuracy in a numerical scheme was discovered through one-dimensional model problems. The lower order time stepping found in many schemes, such as the Gottlieb-Turkel scheme examined here, causes the scheme to revert to the lowest order accuracy. A new uniformly fourth-order accurate numerical method was developed based on this work. The scheme consists of a low-dispersion Runge-Kutta time stepping scheme with a central difference spatial operator. Solution filtering is used to maintain stability. Results in both one- and two-dimensions showed this new scheme clearly superior to the second-order

in time and fourth-order in space Gottlieb-Turkel scheme. The measure used to judge the schemes was the computational efficiency, the time required to reach a given level of error.

The resulting flow solver was configured to run on a shared memory parallel computer. Poor computer architecture prohibited conclusive results, but the evidence indicates that the code scales well up to 16 processors. Results from validation exercises show that the code accurately reproduces both viscous (laminar flat plate) and inviscid (supersonic wedge and cone flows) flows. The validation exercises also confirmed the increased accuracy of the new numerical scheme.

Numerous axisymmetric simulations were performed to investigate the effect of grid resolution, numerical scheme, exit boundary conditions and sub-grid scale model on the solution. While the axisymmetric assumption was not accurate for the jet flowfield, valuable information was gained for use in the three-dimensional calculations.

The three-dimensional calculations showed that this LES simulation accurately captures the physics of the turbulent jet. The agreement with experimental data relatively is good and is much better than results in the current literature. However, there is still much room for improvement. The improved agreement over previous work can be attributed to the new numerical scheme and the modeling of the nozzle lip. A subsequent run using a higher-order solution filter indicated that the modeling of the unresolved scales needs improvement.

Several techniques were used to gain a better understanding of the underlying physics. A plot of dilatation was used to provide insight into the sound field by indicating the location of acoustic sources in the jet mixing layer. Turbulent intensities

indicate that the turbulent structures at this level of modeling are not isotropic and this information could lend itself to the development of improved sub-grid scale models for LES and turbulence models for RANS simulations. A two point correlation technique was used to quantify the turbulent structures. Two point space correlations were used to obtain a measure of the integral length scale, which proved to be approximately $\frac{1}{2}D_j$. Two point space-time correlations were used to obtain the convection velocity for the turbulent structures. This velocity ranged from 0.57 to 0.71 U_j.

There are several recommendations for further work.

The accuracy of the simulations is highly dependent on grid resolution. Accurate resolution of the shock structure in the potential core was found with the axisymmetric calculation. However, the large grid spacing in the azimuthal direction in the 3D calculations diminished this. Further resolution in this direction may improve the prediction of both the shock structure prediction and the mixing layer. A more systematic study of grid resolution in all three directions is desirable, but may be computationally prohibitive.

A change in the order of the solution filter drastically changed the centerline velocity decay. The change in turbulent mixing with an increase in resolution of scales indicates that the sub-grid scale model is not accurately mimicking the effects of the unresolved scales. Further research into improving the sub-grid scale models is necessary. A promising approach is the dynamic sub-grid model [26] which automatically adjusts the coefficients based on the filter width.

The time required to run a simulation on this relatively simple geometry severely limits the usefulness of LES. This limit may be eased if a more efficient numerical

method was found. As shown, the time stepping scheme is typically the factor that limits the computational efficiency. A high-order accuracy efficient time stepping scheme would allow faster turn-around of solutions and more accurate answers on finer grids.

While there is room for improvement in accuracy, this research has shown that large-eddy simulation can be used, as is, to provide new insight and information about high Reynolds number jet flows. The characterization of the turbulent structures, size, convection speed, and degree of anisotropy, can be used to develop improved tools for predicting the fluid mechanics and acoustics of jets.

APPENDIX A

DERIVATION OF THE FILTERED EQUATIONS

A complete derivation of the Favre filtered Navier-Stokes equations used in Chapter 5 is presented.

A.1   The Filter

A filtering function G, is used to separate large and small scale components. The filtering operation applied to a function f is

$$\bar{f} = \int_{-\infty}^{\infty} G(x - \xi)f(\xi)d\xi \tag{A.1}$$

The function can then be decomposed into its resolved/filtered, $\bar{f}$, and unresolved, f' parts

$$f = \bar{f} + f' \tag{A.2}$$

For most applications, the function is not specified. But, several constraints are placed on the the function to ensure that the filter commutes with the derivative.

$$\overline{\frac{\partial f}{\partial x}} = \frac{\partial \bar{f}}{\partial x} \tag{A.3}$$

The constraints are

1) $G(-\xi) = G(\xi)$

2) $\int_{-\infty}^{\infty} G(\xi)d\xi = 1$

3) $G(\xi) \to 0$ as $|\xi| \to \infty$

4) $G(\xi)$ is small outside $\left(-\frac{\Delta}{2}, \frac{\Delta}{2}\right)$

where Δ is a characteristic width of the filter function. Where it has been necessary to know the form of the filter function, researchers have typically used either a box, Gaussian, or spectral cutoff filter.

Favre (density) weighting is used in the filtering process. This allows for convenient recovery of terms corresponding to the unfiltered equations.

$$\tilde{f} = \frac{\overline{\rho f}}{\bar{\rho}} \tag{A.4}$$

A.2 Continuity Equation

Filtering the continuity equation is a straight forward process. The spatial filter is first applied to the continuity equation (2.1).

$$\overline{\frac{\partial \rho}{\partial t}} + \overline{\frac{\partial \rho u_i}{\partial x_i}} = 0 \tag{A.5}$$

Since the filter commutes with the derivative equation (A.5) is rewritten as

$$\frac{\partial \bar{\rho}}{\partial t} + \frac{\partial \overline{\rho u_i}}{\partial x_i} = 0 \tag{A.6}$$

Then Favre weighting is used to recover an equation of the same form as the unfiltered equation (2.1).

$$\frac{\partial \bar{\rho}}{\partial t} + \frac{\partial \bar{\rho}\tilde{u}_i}{\partial x_i} = 0 \tag{A.7}$$

A.3 Momentum Equation

The filtering of the momentum equation and definition of the sub-grid scale stress tensor is presented below. The filtering operation is applied to the momentum equation (2.2).

$$\overline{\frac{\partial \rho u_i}{\partial t}} + \overline{\frac{\partial \rho u_i u_j}{\partial x_j}} + \overline{\frac{\partial p}{\partial x_i}} = \overline{\frac{\partial \sigma_{ij}}{\partial x_j}} \tag{A.8}$$

Using the the property in (A.3) the equation is rewritten

$$\frac{\partial \overline{\rho u_i}}{\partial t} + \frac{\partial \overline{\rho u_i u_j}}{\partial x_j} + \frac{\partial \bar{p}}{\partial x_i} = \frac{\partial \bar{\sigma}_{ij}}{\partial x_j} \tag{A.9}$$

Favre weighting is then applied

$$\frac{\partial \bar{\rho} \tilde{u}_i}{\partial t} + \frac{\partial \bar{\rho} \widetilde{u_i u_j}}{\partial x_j} + \frac{\partial \bar{p}}{\partial x_i} = \frac{\partial \bar{\sigma}_{ij}}{\partial x_j} \tag{A.10}$$

where the filtered stress tensor is

$$\bar{\sigma}_{ij} = \overline{-\frac{2}{3}\mu \delta_{ij} S_{kk}} + \overline{2\mu S_{ij}} \tag{A.11}$$

The filtered stress tensor and the term $\widetilde{u_i u_j}$ are not in useable forms because they are the filter of a product of two variables. We define a new resolved stress tensor as

$$\hat{\sigma}_{ij} = -\frac{2}{3}\tilde{\mu} \delta_{ij} \widetilde{S}_{kk} + 2\tilde{\mu} \widetilde{S}_{kk} \tag{A.12}$$

where $\tilde{\mu} = \mu(\tilde{T})$ and

$$\widetilde{S}_{ij} = \frac{1}{2}\left(\frac{\partial \tilde{u}_j}{\partial x_i} + \frac{\partial \tilde{u}_i}{\partial x_j}\right) \tag{A.13}$$

We can then write (A.11) as

$$\bar{\sigma}_{ij} = \hat{\sigma}_{ij} + (\bar{\sigma}_{ij} - \hat{\sigma}_{ij}) \tag{A.14}$$

Similarly, we write

$$\rho\widetilde{u_i u_j} = \bar{\rho}\tilde{u}_i\tilde{u}_j + \rho\left(\widetilde{u_i u_j} - \tilde{u}_i\tilde{u}_j\right) \qquad (A.15)$$

We define the sub-grid scale stress tensor as

$$\tau_{ij} = \bar{\rho}\left(\widetilde{u_i u_j} - \tilde{u}_i\tilde{u}_j\right) \qquad (A.16)$$

and rewrite (A.15) as

$$\rho\widetilde{u_i u_j} = \bar{\rho}\tilde{u}_i\tilde{u}_j + \tau_{ij} \qquad (A.17)$$

Finally, we substitute (A.14) and (A.17) into (A.10) and obtain the final form of the filtered momentum equation

$$\frac{\partial\bar{\rho}\tilde{u}_i}{\partial t} + \frac{\partial\bar{\rho}\tilde{u}_i\tilde{u}_j}{\partial x_j} + \frac{\partial\bar{p}}{\partial x_i} = \frac{\partial\hat{\sigma}_{ij}}{\partial x_j} - \frac{\partial\tau_{ij}}{\partial x_j} + \frac{\partial}{\partial x_j}\left(\bar{\sigma}_{ij} - \hat{\sigma}_{ij}\right) \qquad (A.18)$$

A.4   Energy Equation

The filtering the energy equation is the most involved process. Because the total energy form of the energy equation is used, several additional manipulations of the resulting terms are required in order to recover terms for which there are sub-grid scale models. Most work in compressible large-eddy simulations have used either static or total enthalpy forms of the energy equation. First the filtering operation is applied to the energy equation (2.6)

$$\overline{\frac{\partial\rho e_t}{\partial t}} + \overline{\frac{\partial\rho u_i e_t}{\partial x_i}} + \overline{\frac{\partial u_i p}{\partial x_i}} = \overline{\frac{\partial u_j\sigma_{ij}}{\partial x_i}} - \overline{\frac{\partial q_i}{\partial x_i}} \qquad (A.19)$$

Commuting the filter operation with the derivative we obtain

$$\frac{\partial\overline{\rho e_t}}{\partial t} + \frac{\partial\overline{\rho u_i e_t}}{\partial x_i} + \frac{\partial\overline{u_i p}}{\partial x_i} = \frac{\partial\overline{u_j\sigma_{ij}}}{\partial x_i} - \frac{\partial\bar{q}_i}{\partial x_i} \qquad (A.20)$$

where

$$\overline{\rho \epsilon}_t = \overline{\rho \epsilon} + \tfrac{1}{2} \overline{\rho u_k u_k} \tag{A.21}$$

Favre weighting equation (A.20) yields

$$\frac{\partial \bar{\rho} \tilde{\epsilon}_t}{\partial t} + \frac{\partial \overline{\rho u_i} \tilde{\epsilon}_t}{\partial x_i} + \frac{\partial \overline{u_i p}}{\partial x_i} = \frac{\partial \overline{u_j \sigma}_{ij}}{\partial x_i} - \frac{\partial \bar{q}_i}{\partial x_i} \tag{A.22}$$

where

$$\tilde{\epsilon}_t = \tilde{\epsilon} + \tfrac{1}{2} \widetilde{u_k u_k} \tag{A.23}$$

As was done with the momentum equation we rewrite the filter of the product of two variables to obtain useable forms.

$$\rho \widetilde{\epsilon_t u_i} = \bar{\rho} \tilde{\epsilon}_t \tilde{u}_i + \bar{\rho} \left(\widetilde{\epsilon_t u_i} - \tilde{\epsilon}_t \tilde{u}_i \right) \tag{A.24}$$

$$\overline{p u_i} = \bar{p} \tilde{u}_i + \left(\overline{p u_i} - \bar{p} \tilde{u}_i \right) \tag{A.25}$$

$$\overline{u_j \sigma}_{ij} = \tilde{u}_j \hat{\sigma}_{ij} + \left(\overline{u_j \sigma}_{ij} - \tilde{u}_j \hat{\sigma}_{ij} \right) \tag{A.26}$$

$$\bar{q}_i = \hat{q}_i + \left(\bar{q}_i - \hat{q}_i \right) \tag{A.27}$$

where

$$\bar{q}_i = -\overline{k \frac{\partial T}{\partial x_i}} \tag{A.28}$$

$$\hat{q}_i = -\tilde{k} \frac{\partial \tilde{T}}{\partial x_i} \tag{A.29}$$

and $\tilde{k} = k(\tilde{T})$. Substituting equations (A.24) - (A.27) into (A.22) we obtain the following form of the filtered energy equation.

$$\frac{\partial \bar{\rho} \tilde{e}_t}{\partial t} + \frac{\partial \bar{\rho} \tilde{u}_i \tilde{e}_t}{\partial x_i} + \frac{\partial \tilde{u}_i \bar{p}}{\partial x_i} = \frac{\partial \tilde{u}_j \hat{\sigma}_{ij}}{\partial x_i} - \frac{\partial \hat{q}_i}{\partial x_i} - \underbrace{\frac{\partial}{\partial x_i} \left[\bar{\rho} \left(\widetilde{e_t u_i} - \tilde{e}_t \tilde{u}_i \right) \right]}_{i}$$

$$- \underbrace{\frac{\partial}{\partial x_i} \left(\overline{p u_i} - \bar{p} \tilde{u}_i \right)}_{ii} + \underbrace{\frac{\partial}{\partial x_i} \left(\overline{u_j \sigma}_{ij} - \tilde{u}_j \hat{\sigma}_{ij} \right)}_{iii} - \frac{\partial}{\partial x_i} \left(\bar{q}_i - \hat{q}_i \right) \quad \text{(A.30)}$$

The underbraced terms can be further manipulated to obtain terms for which sub-grid scale models have been previously developed.

The argument of the derivative in term (i) is transformed as follows.

$$\bar{\rho} \left(\widetilde{e_t u_i} - \tilde{e}_t \tilde{u}_i \right) = \bar{\rho} \left[\widetilde{u_i \left(e + \tfrac{1}{2} u_k u_k \right)} - \tilde{u}_i \left(\tilde{e} + \tfrac{1}{2} \widetilde{u_k u_k} \right) \right]$$

$$= \bar{\rho} \left[\widetilde{u_i e} + \tfrac{1}{2} \widetilde{u_i u_k u_k} - \tilde{u}_i \tilde{e} + \tfrac{1}{2} \tilde{u}_i \widetilde{u_k u_k} \right] \quad \text{(A.31)}$$

$$= \bar{\rho} \left(\widetilde{u_i e} - \tilde{u}_i \tilde{e} \right) + \tfrac{1}{2} \bar{\rho} \left(\widetilde{u_i u_k u_k} - \tilde{u}_i \widetilde{u_k u_k} \right)$$

The first term in (A.31) can be written as the sub-grid scale heat flux.

$$\bar{\rho} \left(\widetilde{u_i e} - \tilde{u}_i \tilde{e} \right) = \bar{\rho} \left(\widetilde{u_i c_v T} - \tilde{u}_i c_v \tilde{T} \right)$$

$$= \bar{\rho} \frac{R}{\gamma - 1} \left(\widetilde{u_i T} - \tilde{u}_i \tilde{T} \right) \quad \text{(A.32)}$$

$$= \frac{R}{\gamma - 1} Q_i$$

The second term in (A.31) is the sub-grid scale turbulent diffusion and is denoted as

$$\tfrac{1}{2} \bar{\rho} \left(\widetilde{u_i u_k u_k} - \tilde{u}_i \widetilde{u_k u_k} \right) = \bar{\rho} D_i \quad \text{(A.33)}$$

Finally the argument of the derivative of term (i) in (A.30) is simplified to

$$\bar{\rho} \left(\widetilde{e_t u_i} - \tilde{e}_t \tilde{u}_i \right) = \frac{R}{\gamma - 1} Q_i + \bar{\rho} D_i \quad \text{(A.34)}$$

Using the filtered equation of state

$$\bar{p} = \bar{\rho} R \tilde{T} \quad \text{(A.35)}$$

the argument of the derivative in term (ii) in (A.30) can be rewritten as the sub-grid scale heat flux as was done in equation (A.32).

$$\overline{p u}_i - \bar{p}\tilde{u}_i = \overline{\rho R T u_i} - \bar{\rho} \bar{R} \bar{T} \tilde{u}_i$$

$$= \bar{\rho} R \left(\widetilde{u_i T} - \tilde{u}_i \tilde{T} \right) \tag{A.36}$$

$$= R Q_i$$

Term (iii) in (A.30) is transformed as follows.

$$\frac{\partial}{\partial x_i} \left(\overline{u_j \sigma}_{ij} - \tilde{u}_j \hat{\sigma}_{ij} \right) = \frac{\partial \overline{u_j \sigma}_{ij}}{\partial x_i} - \frac{\partial \tilde{u}_j \hat{\sigma}_{ij}}{\partial x_i}$$

$$= \frac{\overline{\partial u_j \sigma_{ij}}}{\partial x_j} - \frac{\partial \tilde{u}_j \hat{\sigma}_{ij}}{\partial x_i}$$

$$= \overline{u_j \frac{\partial \sigma_{ij}}{\partial x_i}} + \overline{\sigma_{ij} \frac{\partial u_j}{\partial x_i}} - \tilde{u}_j \frac{\partial \hat{\sigma}_{ij}}{\partial x_i} - \hat{\sigma}_{ij} \frac{\tilde{u}_j}{\partial x_i} \tag{A.37}$$

$$= \epsilon + \left(\overline{u_j \frac{\partial \sigma_{ij}}{\partial x_i}} - \tilde{u}_j \frac{\partial \hat{\sigma}_{ij}}{\partial x_i} \right)$$

where ϵ is the sub-grid scale turbulent dissipation rate

$$\epsilon = \overline{\sigma_{ij} \frac{\partial u_j}{\partial x_i}} - \hat{\sigma}_{ij} \frac{\tilde{u}_j}{\partial x_i} \tag{A.38}$$

Substituting (A.34) (A.36) and (A.37) into (A.30) and rearranging terms gives us the final form of the filtered energy equation.

$$\frac{\partial \bar{\rho} \tilde{e}_t}{\partial t} + \frac{\partial \bar{\rho} \tilde{u}_i \tilde{e}_t}{\partial x_i} + \frac{\partial \tilde{u}_i \bar{p}}{\partial x_i} = \frac{\partial \tilde{u}_j \hat{\sigma}_{ij}}{\partial x_i} - \frac{\partial \hat{q}_i}{\partial x_i} - \frac{\partial}{\partial x_i} \left(\frac{\gamma R}{\gamma - 1} Q_i \right) + \epsilon - \frac{\partial \bar{\rho} D_i}{\partial x_i}$$

$$+ \frac{\partial}{\partial x_i} \left(\overline{u_j \frac{\partial \sigma_{ij}}{\partial x_i}} - \tilde{u}_j \frac{\partial \hat{\sigma}_{ij}}{\partial x_i} \right) - \frac{\partial}{\partial x_i} \left(\bar{q}_i - \hat{q}_i \right) \tag{A.39}$$

A.5 Determination of Pressure

Pressure is normally obtained from the total energy as follows

$$p = \rho \left(\gamma - 1 \right) \left(e_t - \tfrac{1}{2} u_k u_k \right) \tag{A.40}$$

Applying the spatial filter and Favre weighting we obtain

$$\bar{p} = (\gamma - 1)\left(\overline{\rho\epsilon}_t - \tfrac{1}{2}\overline{\rho u_k u_k}\right)$$

$$= (\gamma - 1)\left(\bar{\rho}\tilde{\epsilon}_t - \tfrac{1}{2}\bar{\rho}\widetilde{u_k u_k}\right) \qquad (A.41)$$

The above equation for pressure contains the filter of a product of variables, $\widetilde{u_k u_k}$. This undetermined quantity is eliminated by using the sub-grid scale kinetic energy

$$\bar{p} = (\gamma - 1)\left(\bar{\rho}\tilde{\epsilon}_t - \tfrac{1}{2}\bar{\rho}\widetilde{u_k u_k}\right)$$

$$= (\gamma - 1)\left[\bar{\rho}\tilde{\epsilon}_t - \tfrac{1}{2}\bar{\rho}\tilde{u}_k\tilde{u}_k - \tfrac{1}{2}\bar{\rho}\left(\widetilde{u_k u_k} - \tilde{u}_k\tilde{u}_k\right)\right] \qquad (A.42)$$

$$= (\gamma - 1)\left(\bar{\rho}\tilde{\epsilon}_t - \tfrac{1}{2}\bar{\rho}\tilde{u}_k\tilde{u}_k - \tfrac{1}{2}\tau_{kk}\right)$$

BIBLIOGRAPHY

[1] A. N. Kolmogorov. Local Structure of Turbulence in Incompressible Viscous Fluid for Very Large Reynolds Number. *Doklady Akademiya Nauk SSSR*, 30:299–303, 1941.

[2] D. C. Wilcox. *Turbulence Modeling for CFD*. DCW Industries, second edition, 1998.

[3] W. P. Jones and B. E. Launder. The Prediction of Laminarization with a Two-Equation Model of Turbulence. *International Journal of Heat and Mass Transfer*, 15:301–314, 1972.

[4] S. Sarkar, G. Erlebacher, M. Y. Hussaini, and H. O. Kreiss. The Analysis and Modeling of Dilatational Terms in Compressible Turbulence. NASA CR 181959, 1989.

[5] O. Zeman. Dilatational Dissipation: The Concept and Application in Modeling Compressible Mixing Layers. *Physics of Fluids A*, 2(2):178–188, 1990.

[6] S. B. Pope. An Explanation of the Turbulent Round-Jet/Plane-Jet Anomaly. *AIAA Journal*, 16(3):279–281, 1978.

[7] T. J. Barber, L. M. Chiapetta, J. R. DeBonis, N. J. Georgiadis, and D. A. Yoder. Assesment of the Parameters Influencing the Prediction of Shear Layer Mixing. *Journal of Propulsion and Power*, 15(1):45–53, 1998.

[8] R. Courant, K. O. Friedrichs, and H. Lewy. On the Partial Difference Equations of Mathematical Physics. *IBM Journal of Research and Development*, 11:215–234, 1967.

[9] D. Gottlieb and E. Turkel. Dissipative Two-Four Methods for Time-Dependent Problems. *Mathematics of Computation*, 30(136):703–723, 1976.

[10] S. K. Lele. Compact Finite Difference Schemes with Spectral-Like Resolution. *Journal of Computational Physics*, 103:16–42, 1992.

[11] C. K. W. Tam and J. C. Webb. Dispersion Relation-Preserving Finite Difference Schemes for Computational Aeroacoustics. *Journal of Computational Physics*, 107:262-281, 1993.

[12] M. R. Visbal and D. V. Gaitonde. High-Order Accurate Methods for Unsteady Vortical Flows on Curvilinear Meshes. AIAA Paper 98-0131, 1998.

[13] R. Hixon. A new class of compact schemes. AIAA Paper 98-0367, 1998.

[14] R. Hixon. Nonlinear Comparison of High-Order and Optimized Finite-Difference Schemes. NASA CR 1998-208670, 1998.

[15] R. Hixon and E. Turkel. High-Accuracy Compact MacCormack-Type Schemes for Computational Aeroacoustics. NASA CR 1998-208672, 1998.

[16] J. B. Freund and P. Moin. Mixing Enhancement in Jet Exhaust Using Fluidic Actuators: Direct Numerical Simulations. FEDSM 98-5235, ASME, 1998. Proceedings of FEDSM'98.

[17] J. B. Freund, S. K. Lele, and P. Moin. Direct Simulation of a Mach 1.92 Jet and its Sound Field. AIAA/CEAS Paper 98-2291, 1998.

[18] J. B. Freund. Direct Numerical Simulation of the Noise from a Mach 0.9 Jet. FEDSM 99-7251, ASME, 1999. Proceedings of FEDSM'99.

[19] J. H. Ferziger and D. C. Leslie. Large Eddy Simulation: A Predictive Approach to Turbulent Flow Computation. AIAA Paper 79-1471, 1979.

[20] R. S. Rogallo and P. Moin. Numerical Simulation of Turbulent Flows. *Annual Review of Fluid Mechanics*, 16:99-137, 1984.

[21] J. H. Ferziger. Recent Advances in Large-Eddy Simulation. In W. Rodi and G. Begeles, editors, *Engineering Turbulence Modeling and Experiments 3*, page 163. Elsevier, 1996.

[22] M. Lesieur and O. Metais. New Trends in Large-Eddy Simulations of Turbulence. *Annual Review of Fluid Mechanics*, 28:45, 1996.

[23] U. Piomelli. Large-Eddy Simulations: Present State and Future Directions. AIAA Paper 98-0534, 1998.

[24] J. Smagorinsky. General Circulation Experiments with the Primitive Equations, Part I: The Basic Experiment. *Monthly Weather Review*, 91:99-152, 1963.

[25] F. M. White. *Viscous Fluid Flow*. McGraw-Hill, 1974.

[26] M. Germano, U. Piomelli, P. Moin, and W. Cabot. A Dynamic Subgrid-Scale Eddy Viscosity Model. *Physics of Fluids A*, 3:1760, 1991.

[27] J. Bardina, J. H. Ferziger, and W. C. Reynolds. Improved Subgrid Models for Large Eddy Simulation. AIAA Paper 80-1357, 1980.

[28] P. Moin, K. Squires, W. Cabot, and S. Lee. A Dynamic Subgrid-Scale Model for Compressible Turbulence and Scalar Transport. *Physics of Fluids A*, 3(11):2746-2757, 1991.

[29] Y. Zang, R. L. Street, and J. R. Koseff. A Dynamic Mixed Subgrid-Scale Model and its Application to Turbulent Recirculating Flows. *Physics of Fluids A*, 5:3186-3196, 1991.

[30] C. C. Nelson. *Simulations of Spatially Evolving Compressible Turbulence Using a Local Dynamic Subgrid Model*. PhD thesis, Georgia Institute of Technology, 1997.

[31] R. R. Mankbadi, S. H. Shih, and R. Hixon. Direct Computation of Sound Radiation by Jet Flow Using Large-Scale Equations. NASA TM 106877, 1995.

[32] L. Gamet and J. L. Estivalezes. Application of Large-Eddy Simulations and Kirchoff Method to Jet Noise Prediction. *AIAA Journal*, 36(12):2170-2178, 1998.

[33] D. Choi, T. J. Barber, L. M. Chiapetta, and M. Nishimura. Large Eddy Simulation of High-Reynolds Number Jet Flows. AIAA Paper 99-0230, 1999.

[34] R. W. MacCormack. The Effect of Viscosity in Hypervelocity Impact Cratering. AIAA Paper 69-354, 1969.

[35] P. D. Lax and B. Wendroff. Systems of Conservation Laws. *Communications on Pure and Applied Mathematics*, 13:217-237, 1960.

[36] A. Bayliss, P. Parikh, L. Maestrello, and E. Turkel. A Fourth-Order Scheme for the Unsteady Compressible Navier-Stokes Equations. NASA CR 177994, 1985.

[37] A. Jameson and T. J. Baker. Multigrid Solution of the Euler Equations for Aircraft Configurations. AIAA Paper 84-0093, 1984.

[38] M. H. Carpenter and C. A. Kennedy. Fourth-Order 2N-Storage Runge-Kutta Schemes. NASA TM 109112, 1994.

[39] F. Q. Hu, M. Y. Hussaini, and J. L. Manthey. Low-Dissipation and Low-Dispersion Runge-Kutta Schemes for Computational Acoustics. *Journal of Computational Physics*, 124:177-191, 1996.

[40] S. Gottlieb and C. W. Chu. Total Variation Diminishing Runge-Kutta Schemes. NASA CR 201591, 1996.

[41] D. Stanescu and W. G. Habashi. 2N-Storage Low Dissipation and Dispersion Runge-Kutta Schemes for Computational Acoustics. *Journal of Computational Physics*, 143(12):674–681, 1998.

[42] R. Vichnevetsky and J. B. Bowles. *Fourier Analysis of Numerical Approximations of Hyperbolic Equations*. Society for Applied and Industrial Mathematics, 1982.

[43] C. K. W. Tam. Computational Aeroacoustics: Issues and Methods. *AIAA Journal*, 33(10), 1995.

[44] T. H. Pulliam. Artificial Dissipation Models for the Euler Equations. *AIAA Journal*, 24(12):1932–1940, 1986.

[45] G. Dulikravich and D. Dorney. Artificial Dissipation Sensors for Computational Gasdynamics. AIAA Paper 89-0643, 1989.

[46] C. Hirsch. *Numerical Computation of Internal and External Flows*, volume 2, pages 344–395. John Wiley & Sons, 1990.

[47] E. Turkel and V. N. Vatsa. Effect of Artificial Viscosity on Three-Dimensional Flow Solutions. *AIAA Journal*, 32(1):39–45, 1994.

[48] C. A. Kennedy and M. H. Carpenter. Comparison of Several Numerical Methods for Simulation of Compressible Shear Layers. NASA TP 3484, 1997.

[49] R. Hixon. Prefactored Compact Filters for Computational Aeroacoustics. AIAA Paper 99-0358, 1999.

[50] G. B. Whitham. *Linear and Nonlinear Waves*. John Wiley & Sons, 1974.

[51] R. D. Snyder and J. N. Scott. Comparison of Numerical Schemes for the Analysis of Aeroacoustics. AIAA Paper 99-0354, 1999.

[52] B. Vreman, B. Geurts, and H. Kuerten. Subgrid-Modelling in LES of Compressible Flows. In P. R. Voke et al., editor, *Direct and Large-Eddy Simulation I*, pages 133–144. Kluwer Academic Publishers, 1994.

[53] E. R. Van Driest. On Turbulent Flow Near a Wall. *Journal of the Aeronautical Sciences*, 23:1007–1011, 1956.

[54] G. Erlebacher, M. Y. Hussaini, C. G. Speziale, and T. A. Zang. Toward the Large-Eddy Simulation of Compressible Turbulent Flows. NASA CR 187460, 1990.

[55] D. A. Anderson, J. C. Tannehill, and R. H. Pletcher. *Computational Fluid Mechanics and Heat Transfer*. Taylor & Francis, 1984.

[56] M. Vinokur. Conservation Equations of Gas-Dynamics in Curvilinear Coordinate Systems. *Journal of Computational Physics*, 14:105–125, 1974.

[57] R. Hixon, S. H. Shih, T. Dong, and R. R. Mankbadi. Evaluation of Generalized Curvilinear Coordinate Transformations Applied to High-Accuracy Finite-Difference Schemes. AIAA Paper 98-0370, 1998.

[58] R. W. MacCormack. *Numerical Solution of the Interaction of a Shock Wave with a Laminar Boundary Layer*, volume 8 of *Lecture Notes in Physics*, pages 151–163. Springer-Verlag, 1971. Proceedings of the Second International Conference on Numerical Methods in Fluid Dynamics.

[59] M. B. Giles. Nonreflecting Boundary Conditions for Euler Equation Calculations. *AIAA Journal*, 28(12):2050–2058, 1990.

[60] R. Hixon, S. H. Shih, and R. R. Mankbadi. Evaluation of Boundary Conditions for Computational Aeroacoustics. NASA TM 106645, 1995.

[61] T. Colonius, S. K. Lele, and P. Moin. Boundary Conditions for Direct Computation of Aerodynamic Sound Generation. *AIAA Journal*, 31(9):1574–1582, 1993.

[62] J. B. Freund. Proposed Inflow/Outflow Boundary Condition for Direct Computation of Aerodynamic Sound. *AIAA Journal*, 35(4):740–742, 1997.

[63] M. J. Quinn. *Designing Efficient Algorithms for Parallel Computers*. McGraw-Hill, 1987.

[64] D. P. Bertsekas and J. N. Tsitsiklis. *Parallel and Distributed Computation*. Prentice Hall, 1989.

[65] J. H. Ferziger and M. Perić. *Computational Methods for Fluid Dynamics*. Springer-Verlag, 1996.

[66] H. Schlicting. *Boundary Layer Theory*. McGraw-Hil, seventh edition, 1979.

[67] Ames Research Staff. Equations, Tables and Charts for Compressible Flow. NACA Report 1135, 1953.

[68] J. Panda and R. G. Seasholtz. Density measurement in underexpanded supersonic jets using rayleigh scattering. AIAA Paper 98-0281, 1998.

[69] J. Panda and R. G. Seasholtz. Velocity and temperature measurement in supersonic free jets using spectrally resolved rayleigh scattering. AIAA Paper 99-0296, 1999.

[70] J. Panda and R. G. Seasholtz. Density fluctuation measurement in supersonic fully expanded jets using rayleigh scattering. AIAA Paper 99-1870, 1999.

[71] J. Panda and R. G. Seasholtz. Investigation of density fluctuations in supersonic free jets and corrleation with generated noise. AIAA Paper 2000-2099, 2000.

[72] H. Tennekes and J. L. Lumley. *A First Course in Turbulence*. MIT Press, 1972.

[73] W. T. Chu. Turbulence Measurements Relevant to Jet Noise. UTIAS Report 119, University of Toronto Institute for Aerospace Studies, 1966.

[74] J. N. Scott. A Comparison of Numerical and Experimental Results for Unsteady Flow Associated with Jet Noise. AIAA Paper 94-0459, 1994.

[75] Gridgen Version 13. User manual, Pointwise, Inc., 1998.

[76] K. A. Hoffmann. *Computational Fluid Dynamics for Engineers*. Engineering Education System, 1989.

[77] G. N. Abramovich. *The Theory of Turbulent Jets*. MIT Press, 1963.

[78] P. O. Witze. Centerline velocity decay of compressible free jets. *AIAA Journal*, 12(4):417–4186, 1974.

[79] E. Kreyszig. *Advanced Engineering Mathematics*. John Wiley & Sons, seventh edition, 1993.
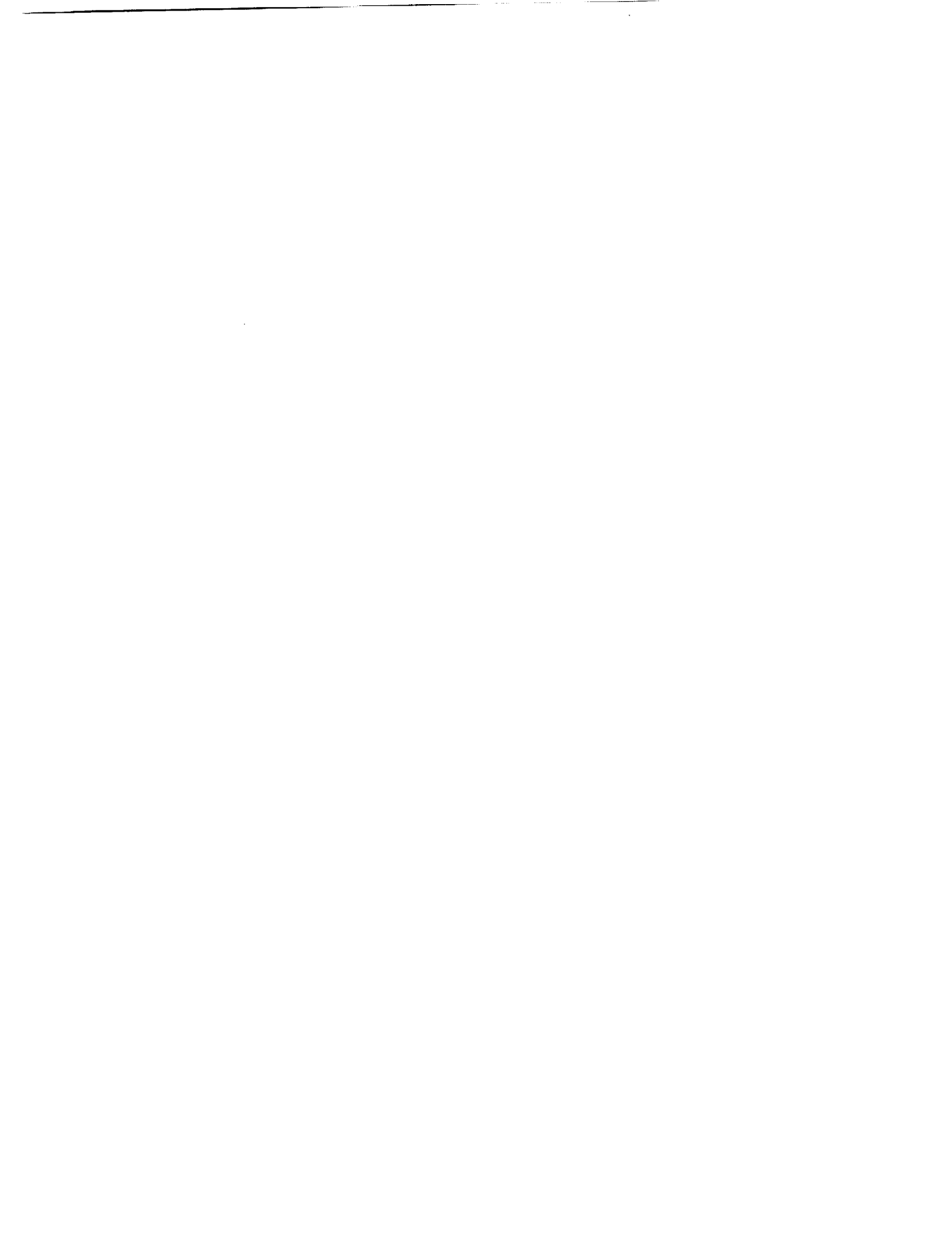
REPORT DOCUMENTATION PAGE

Public reporting burden for this collection of information is estimated to average 1 hour per response, including the time for reviewing instructions, searching existing data sources, gathering and maintaining the data needed, and completing and reviewing the collection of information. Send comments regarding this burden estimate or any other aspect of this collection of information, including suggestions for reducing this burden, to Washington Headquarters Services, Directorate for Information Operations and Reports, 1215 Jefferson Davis Highway, Suite 1204, Arlington, VA 22202-4302, and to the Office of Management and Budget, Paperwork Reduction Project (0704-0188), Washington, DC 20503.

1. AGENCY USE ONLY (Leave blank)	2. REPORT DATE	3. REPORT TYPE AND DATES COVERED
	May 2001	Technical Memorandum

4. TITLE AND SUBTITLE

The Numerical Analysis of a Turbulent Compressible Jet

5. FUNDING NUMBERS

WU–708–90–43–00

6. AUTHOR(S)

James R. DeBonis

7. PERFORMING ORGANIZATION NAME(S) AND ADDRESS(ES)

National Aeronautics and Space Administration
John H. Glenn Research Center at Lewis Field
Cleveland, Ohio 44135–3191

8. PERFORMING ORGANIZATION REPORT NUMBER

E–12669

9. SPONSORING/MONITORING AGENCY NAME(S) AND ADDRESS(ES)

National Aeronautics and Space Administration
Washington, DC 20546–0001

10. SPONSORING/MONITORING AGENCY REPORT NUMBER

NASA TM—2001-210716

11. SUPPLEMENTARY NOTES

This report was submitted as a dissertation in partial fulfillment of the requirements for the degree Doctor of Philosophy to the Graduate School of the Ohio State University, Cleveland, Ohio, 2000. Responsible person, James R. Debonis, organization code 5860, 216–433–6581.

12a. DISTRIBUTION/AVAILABILITY STATEMENT

Unclassified - Unlimited
Subject Categories: 02, 07 and 34   Distribution: Nonstandard

Available electronically at http://gltrs.grc.nasa.gov/GLTRS

This publication is available from the NASA Center for AeroSpace Information, 301–621–0390.

12b. DISTRIBUTION CODE

13. ABSTRACT (Maximum 200 words)

A numerical method to simulate high Reynolds number jet flows was formulated and applied to gain a better understanding of the flow physics. Large-eddy simulation was chosen as the most promising approach to model the turbulent structures due to its compromise between accuracy and computational expense. The filtered Navier-Stokes equations were developed including a total energy form of the energy equation. Subgrid scale models for the momentum and energy equations were adapted from compressible forms of Smagorinsky's original model. The effect of using disparate temporal and spatial accuracy in a numerical scheme was discovered through one-dimensional model problems and a new uniformly fourth-order accurate numerical method was developed. Results from two- and three-dimensional validation exercises show that the code accurately reproduces both viscous and inviscid flows. Numerous axisymmetric jet simulations were performed to investigate the effect of grid resolution, numerical scheme, exit boundary conditions and subgrid scale modeling on the solution and the results were used to guide the three-dimensional calculations. Three-dimensional calculations of a Mach 1.4 jet showed that this LES simulation accurately captures the physics of the turbulent flow. The agreement with experimental data was relatively good and is much better than results in the current literature. Turbulent intensities indicate that the turbulent structures at this level of modeling are not isotropic and this information could lend itself to the development of improved subgrid scale models for LES and turbulence models for RANS simulations. A two point correlation technique was used to quantify the turbulent structures. Two point space correlations were used to obtain a measure of the integral length scale, which proved to be approximately $1/2\ D_j$. Two point space-time correlations were used to obtain the convection velocity for the turbulent structures. This velocity ranged from 0.57 to 0.71 U_j.

14. SUBJECT TERMS

Large eddy simulation; Jet flow; Turbulent jets

15. NUMBER OF PAGES

198

16. PRICE CODE

17. SECURITY CLASSIFICATION OF REPORT	18. SECURITY CLASSIFICATION OF THIS PAGE	19. SECURITY CLASSIFICATION OF ABSTRACT	20. LIMITATION OF ABSTRACT
Unclassified	Unclassified	Unclassified	

NSN 7540-01-280-5500